New Uses of Micro and Nanomaterials

*Edited by Marcelo Rubén Pagnola,
Jairo Useche Vivero and Andres Guillermo Marrugo*

NEW USES OF MICRO AND NANOMATERIALS

Edited by **Marcelo Rubén Pagnola, Jairo Useche Vivero** and **Andres Guillermo Marrugo**

New Uses of Micro and Nanomaterials
http://dx.doi.org/10.5772/intechopen.73361
Edited by Marcelo Rubén Pagnola, Jairo Useche Vivero and Andres Guillermo Marrugo

Contributors

Rodica-Mariana Ion, Ramona Marina Grigorescu, Lorena Iancu, Paul Ghioca, Nicoleta Radu, Abdullah Ahmed Ali Ahmed, Marcin Gorski, Małgorzata Krystek, Kw Guo, Pablo Levy, Cynthia Quinteros, Alexander Hardtdegen, Susanne Hoffmann-Eifert, Mariano Barella, Federico Golmar, Félix Palumbo, Javier Curiale, Marcelo Pagnola, Jairo Useche Vivero, Andres G Marrugo, Ashraf Ghanem, Diana Ibrahim, Chandrabhan Verma, Zhenhua Dan, Fengxiang Qin, Izumi Muto, Nobuyoshi Hara, Hui Chang, Corneliu Doroftei, Liviu Leontie, Hiromi Miura

Notice

Statements and opinions expressed in the chapters are these of the individual contributors and not necessarily those of the editors or publisher. No responsibility is accepted for the accuracy of information contained in the published chapters. The publisher assumes no responsibility for any damage or injury to persons or property arising out of the use of any materials, instructions, methods or ideas contained in the book.

We are IntechOpen,
the world's leading publisher of Open Access books
Built by scientists, for scientists

3,800+
Open access books available

116,000+
International authors and editors

120M+
Downloads

151
Countries delivered to

Our authors are among the

Top 1%
most cited scientists

12.2%
Contributors from top 500 universities

Interested in publishing with us?
Contact book.department@intechopen.com

Numbers displayed above are based on latest data collected.
For more information visit www.intechopen.com

Meet the editors

Dr.Ing. Marcelo R. Pagnola, born in Buenos Aires on November 22, 1969, completed his training as a mechanical engineer at the Universidad Nacional de Lomas de Zamora, Buenos Aires, Argentina, in 1996, with excellent results. He obtained the degree of Doctor of Engineering at the University of Buenos Aires in 2009 with a summa cum laude, after working in the private sector in different areas and managerial positions. He is currently a member of CONICET and Director of the Magnetic Materials Pilot Plant, INTECIN. He is also a member of different scientific committees, a reviewer of international publications, and a director of different research projects financed by government agencies at national and international levels. Dr. Pagnola has directed engineering and doctorate theses, has taught university courses in physics and has managed PhD courses in materials and nanomaterials. He is author of more than 50 publications for congresses, as well as international journals and books on materials engineering. He has received different mentions from the Rector of the University of Buenos Aires for his academic contributions to engineering. He is currently working as a professor in the Department of Physics at the Engineering Faculty of the University of Buenos Aires, Argentina.

Dr. Jairo Useche is Professor of Mechanical Engineering at the Universidad Tecnológica de Bolivar at Cartagena de Indias, Colombia, South America. He received his PhD in Mechanical Engineering from the State University of Campinas, Brazil, his BS in Mechanical Engineering at the Universidad Tecnológica de Bolivar, Colombia, and his MSc in Mechanical Engineering at the Universidad de Los Andes, Colombia. Dr. Useche is a consulting engineer and worked as a mechanical engineer in a number of companies for several years. He has been involved in several major projects dealing with numerical modeling, structural mechanics, composite materials, deformable shaft vibrations, and the reliability assessment of buried pipes. He teaches various engineering courses at both undergraduate and graduate levels. He has developed and taught several solid mechanics engineering courses, including mechanics of materials, advanced numerical modeling, structural vibrations, and finite element analysis in solid and structural mechanics. His research and consulting expertise includes structural mechanics, structural reliability of buried pipes, pipes and structural panels under blast loads, composite mechanics of naval structures, and control of fractures in plates.

Dr. Andrés G. Marrugo is currently an associate professor in the Department of Mechanical and Mechatronics Engineering at the Universidad Tecnológica de Bolívar, Colombia, where he did his BE in Mechatronics Engineering (summa cum laude). He received his PhD in Optical Engineering (cum laude) and MSc in Photonics from the Universitat Politècnica de Catalunya, Spain. He was the recipient of the Honors Diploma for Young Researchers from the Spanish Optical Society (SEDOPTICA). His research interests include optical metrology, biomedical image analysis, computer vision, and image processing.

Contents

Preface

The invention of the scanning tunneling microscope in 1981, the development of atomic force microscopy in 1984, and the discovery of fullerenes in 1985 are three major events that defined the birth of nanotechnology. These three events triggered a series of new explorations and applications of micro- and nanostructured materials, which have modified and different physical and chemical properties compared to the same elements at larger scales. It is for this reason that the precise control of individual components in nanostructures is crucial to realizing different functionalities in applications in electronics, energy-conversion devices, biotechnologies, and other specific applications. The morphology of the nanostructures depends not only on the compatibility between their component phases but also on the mixing method and its dispersion if chemical approaches are used. On the other hand, the use of physical methods, self-assembly, and bottom-up approaches also allows bulk nanostructures to be synthesized. The micro- and macroscopic properties of the system (optical or magnetic properties, conductivity, etc.) can vary without changing the chemical composition of the original material simply by controlling different parameters at the nanoscale of the materials.

In this book, the reader will discover the manufacture of nanostructures with current methodologies and their applications and uses in different techniques applied to engineering.

These aspects make the application and development of new composites attractive in different technologic fields, improving performance parameters in equipment with respect to energy savings. In addition, new and improved technological applications are being discovered in hitherto unthinkable fields of science.

This book is divided into the following parts:

Part 1: Engineering: Techniques and Processes.

Part 2: Engineering: Models and Applications.

This collection of articles presents a set of excellent studies using state-of-the-art methodologies by professional researchers from different countries in the most diverse areas of knowledge and makes the book an excellent tool for those interested in looking for the latest progressions in the topic of nanotechnology.

The editor and coeditors thank Ivana Glavic, the Author Service Manager Intech Open, for her help in the production of this book.

Prof. Dr.Ing. Pagnola Marcelo
University of Buenos Aires
National Council of Scientific and Technical Research
Institute of Technology and Engineering Sciences "Ing. Hilario Fernández Long" (INTECIN)
Buenos Aires, Argentina

Jairo F. Useche and Andrés G. Marrugo
Universidad Tecnológica de Bolívar, Colombia

Engineering, Techniques and Processes

The Atomic Layer Deposition Technique for the Fabrication of Memristive Devices: Impact of the Precursor on Pre-deposited Stack Materials

Cynthia P. Quinteros, Alex Hardtdegen,
Mariano Barella, Federico Golmar, Félix Palumbo,
Javier Curiale, Susanne Hoffmann-Eifert and
Pablo Levy

Additional information is available at the end of the chapter

Abstract

Atomic layer deposition (ALD) is a standard technique employed to grow thin-film oxides for a variety of applications. We describe the technique and demonstrate its use for obtaining memristive devices. The metal/insulator/metal stack is fabricated by means of ALD-grown HfO_2, deposited on top of a highly doped Si substrate with an SiO_2 film and a Ti electrode. Enhanced device capabilities (forming free, self-limiting current, non-crossing hysteretic current-voltage features) are presented and discussed. Careful analysis of the stack structure by means of X-ray reflectometry, atomic force microscopy, and secondary ion mass spectroscopy revealed a modification of the device stack from the intended sequence, $HfO_2/Ti/SiO_2/Si$. Analytical studies unravel an oxidation of the Ti layer which is addressed for the use of the ozone precursor in the HfO_2 ALD process. A new deposition process and the model deduced from impedance measurements support our hypothesis: the role played by ozone on the previously deposited Ti layer is found to determine the overall features of the device. Besides, these ALD-tailored multifunctional devices exhibit rectification capability and long enough retention time to deserve their use as memory cells in a crossbar architecture and multibit approach, envisaging other potential applications.

Keywords: atomic layer deposition, nonvolatile memory, forming free memristive device, complementary resistive switching cell, redox-based resistive random access memory, ReRAM

1. Introduction

1.1. The ALD technique

The chemical vapor deposition (CVD) technique is a chemical reaction of a volatile compound with other gases for the deposition of a solid on a substrate. This reaction takes place inside a reactor in which the reactants are inserted as gases. Temperature and pressure are the two main parameters to be controlled. Temperature affects the rate in a predictable manner (Arrhenius behavior). The pressure range, even when it has a lower impact, determines whether the deposition mechanism will be surface-reaction limited or transport limited. During a transport-limited process, the deposition speed is very high, and the growth rate is very sensitive to the temperature. On the contrary, a surface-reaction regime can reach rates as low as an atomic layer per cycle by means of an oversupply of reactants available in the vicinity of the surface. This regime is more conditioned by the boundary layer than by the main flow of reactants, being less dependent on the temperature.

The atomic layer deposition (ALD) technique, though bearing many resemblances to CVD, excludes the gas phase reaction of the precursors. ALD is characterized by chemisorption steps while the physisorbed molecules are purged away during the necessary purge steps [1–3]. ALD relies on the activation of the surface on top of which the resultant layer is placed. This activation insures the growth to be self-limited to the minimum thickness determined by the reaction (usually an atomic layer). The substrate surface exhibits a certain density of surface sites, for example, OH groups, which serve as "anchors" for the metal precursor molecules. ALD requires four steps: I—chemisorption of the metal precursor to surface (OH) groups; II—release of the by-products during the purge; III—the reaction of the oxygen source with the remaining reactive groups at the metal ion; and IV—the purge of the by-products. After steps I–IV, the surface is again covered with (OH) groups, now on the deposited surface layer. The chemisorption of the precursor molecules to the surface, which can happen via different chemical reactions (1), stops suddenly when all surface sites are occupied. As a consequence, the ALD process exhibits extremely low deposition rates and an accurate control of the film thickness. The strict timely separation of the two precursor materials, which is achieved with the purge steps, gives the difference between ALD and CVD.

The key role played by the buffer material in the ALD technique can be identified from the described procedure. Surface preparation consists of the chamber introduction of some precursor that reacts with the former and improves the adhesion of the deposited compound. After that, deposition is performed by cycles in order to grow, layer by layer, the required material in a controlled manner. In the case of binary oxides, each cycle requires an oxygen source and a metal precursor. The oxidant and precursor chemically react, giving rise to a conformal growth layer above the buffered surface. The reaction during each cycle is summarized in Eq. (1):

$$AB \ (precursor) + CD \ (precursor) \rightarrow AC \ (solid \ formed \ at \ the \ surface) + BD \ (gas) \qquad (1)$$
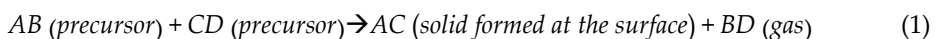
Before repeating each cycle, purge gases are inserted into the chamber to avoid further reactions with possible remaining products. Once a complete run has occurred (activation, oxidant

and precursor, and purge gases), the process is repeated as many times as required to obtain the desired film thickness. It is worth to point out that the two gas-phase reactants are not in contact in the gas phase since the surface reactions are performed sequentially. The reaction (Eq. (1)) occurs when the second reactant reaches the surface. This sequence avoids possible reactions in the gas phase that could collapse at the surface forming undesired grains. Typical deposition rates are in the order of 0.1 nm per cycle [2].

ALD is a very versatile technique for many reasons. Among them, we emphasize here those that allow large-scale production: suitability to be applied in a wide temperature range, low cost, and easy scalability. Many reviews have addressed the fundamentals of ALD and its applications [1, 4]. Instead, the aim of the present study is to demonstrate how a spurious phase, produced by some inherent details of the technique, could be used to achieve devices with improved characteristics. This chapter highlights exactly such an issue in a concrete example: the deposition of a thin film of HfO_2 by ALD on top of a Ti-buffered Si/SiO$_2$ substrate. We will show how an unconsidered change, produced by the nature of the oxidant itself, has occurred at the Ti buffer during the ALD cycle, determining the growth of an extra oxide layer of TiO_x and thus providing interesting and useful features to the final device. We will take advantage of several microscopic and macroscopic techniques in order to fully characterize the resulting oxide layer, in order to fully elucidate the effect produced by the surface reaction.

In brief, we report here the structural evidence for the presence of TiO_x below the HfO_2 layer and discuss the key role of the O_3 precursor in its formation during the ALD process. Although it is quite difficult to disentangle the oxidant and/or precursor effect, some signs seem to point to the former as the main responsible one of the produced changes. We also include macroscopic electrical evidence to support that the TiO_x layer determines the occurrence of a very interesting metal-insulator-metal nonvolatile memory device. Besides, an additional deposition process was carried out in order to clarify whether we could be in presence of another unconsidered effect. Finally, we will introduce a phenomenological model to describe the electrical response and microscopic transport properties that support the microscopic picture achieved.

1.2. Details of the ALD technique and the device's fabrication

For ALD-based HfO_2 growth, the oxygen source is typically either H_2O [4] or O_3 [4] while the metal source could be for example Tetrakis(dimethylamino)hafnium (TDMAH) or TEMAH [5]. In our specific case, O_3 and TDMAH were the oxygen and metal source, respectively, although we will also include some comparison with samples grown using H_2O instead of O_3. The substrate employed was commercial Si (highly doped)/thermally oxidized SiO_2 (120 nm) of 1 cm^2 size. The Ti layer (20 nm) was sputtered on top. After Ti sputtering, the ALD process—using either ozone as oxygen source and TDMAH as the metal precursor—was carried out to obtain a uniform 20 nm-thick HfO_2 layer. After this deposition process an array of 5 lines by 16 columns was determined by means of optical photolithography, delimiting 80 squared-shaped structures of 200 μm lateral size covered with sputtered Pd (40 nm)/Co (35 nm) acting as the top electrode (TE). To complete these two terminal devices, the access to the bottom contact was achieved by a scratch.

1.3. The ReRAM scenario

As downscaling of storage devices is approaching its physical limits, new strategies based on emergent materials and non-previously explored effects are moving into the focus of intense research as FLASH memory replacement. In particular, the metal-insulator-metal (MIM) structures acting as memory cells are developing as prominent candidates for such replacement. The resistive switching (RS) is the mechanism underlying the memory behavior. Its appealing features (speed, downscaling, retention, endurance) have evolved into a nowadays mature technology, coined as resistive random access memory (ReRAM).

The ability to produce a reversible change of conductance in these technologically simple structures (the RS effect) relies on the extremely large electric field applied to the strategically engineered thin insulating layer (i.e., between the metallic electrodes) but also on the choice of the electrodes' material. Basically, the effect consists of a switching process between a high resistance state (HRS) and a low resistance state (LRS) through a soft dielectric breakdown of the insulating layer(s). The change from HRS to LRS is called the SET process and the opposite one (from LRS to HRS) is referred to as RESET. Thus, memristive cells are resistive switching units, and their unique properties are strongly dependent on the materials used and on the fabrication details. They could need an initial electroforming process or not, and the polarity could be a relevant parameter (bipolar switches) or not (unipolar switches). Comprehensive discussions on the resistive switching phenomena are found in Ref. [6].

The simplicity of the geometrical structure and the absence of transistors make the concept extremely interesting for low-power, high-density, and nonvolatile memory applications. However, a challenge to achieve a technological implementation, using the RS concept, is to be allowed to select a designated cell within a passive crossbar array without interference from neighboring cells (i.e., the sneak currents problem) [7].

A way to overcome the sneak currents problem includes the use of rectifying elements to isolate each nonvolatile memory cell. The integration of a rectifying element, to achieve bipolar operation, would solve the sneak path problem "in situ." But so far no sufficiently scalable material has been found yet [7]. Therefore, simple structures based on nanometer thick oxides are a major topic of work in scientific and industrial research. A detailed knowledge of expected behaviors allows material engineering. In that sense, rectifying metal/oxide junctions, based on TiO_x, ZnO, and on TaO_{2-x}, has been recently described [8, 9], where upon appropriate oxygen vacancy accumulation the interface is switched to a non-rectifying resistive device. In particular, structures based on HfO_2 have shown excellent rectifying capabilities [10, 11]. Besides, hafnium oxide is a preferred high-k material, and therefore it is one of the most promising ReRAM materials since it has been already added to the complementary metal-oxide semiconductor (CMOS). From the industrial point of view, this fact is an enormous advantage and explains why so much effort is being done related with HfO_2.

In this scenario, and responding to the actual trend on multifunctional components, there is a renewed interest on the mechanisms governing its dielectric behavior. These facts, combined with the observation of perpendicular magnetic anisotropy (which involves another promising low-power memory mechanism [12]) in Co films deposited on high-k materials [13] and FeFETs based on doped HfO_2 [14], put devices based on HfO_2 again in the focus of the attention.

2. Understanding the origin of remarkable electrical properties in simple RS stacks based on ALD-deposited HfO$_2$

2.1. Electrical characterization

The MIM stack was electrically characterized in a two-terminal configuration (see inset **Figure 1a**). We used a Keithley 4200 unit hooked through coaxial wires to a room-temperature probe station. Applying voltage while recording the current flowing through the stack allowed us to identify the general properties of the devices. In particular, sweeping voltage in a pulsed way is suitable for avoiding heating effects.

Figure 1a shows a typical current-voltage (I-V) dependence of a fabricated stack, obtained by sweeping voltage pulses, as demonstrated in the inset in **Figure 1a**. Four branches can be defined: (a) from 0 to +15 V, (b) from +15 to 0 V, (c) from 0 to −15 V, and (d) from −15 to 0 V. After deposition (pristine state), all devices are found in HRS (branch A in **Figure 1a**). When the positive voltage applied to the top electrode is increased, the device abruptly switches to LRS in a SET operation happening at around +5 V. No additional previous "forming" is required. Upon decreasing the stimulus (branch B), the I-V curve exhibits huge hysteresis (the semi-logarithmic scale in **Figure 1b** highlights the change rate).

Further cycling with positive voltages reproduces the LRS, as shown in the second and fourth sweeps in **Figure 1b**. Thus, the programmed state is nonvolatile with respect to the time scale of the measurement.

When the polarity is reversed, the negative voltage cycle starts in the HRS (branch C in **Figure 1a**), even when the positive cycle finished in a LRS, that is, a rectifying response is found. This behavior is referred to as a non-crossing hysteresis in the literature [15]. From that HRS on, the description of the negative voltage cycle is completely analogous to the positive

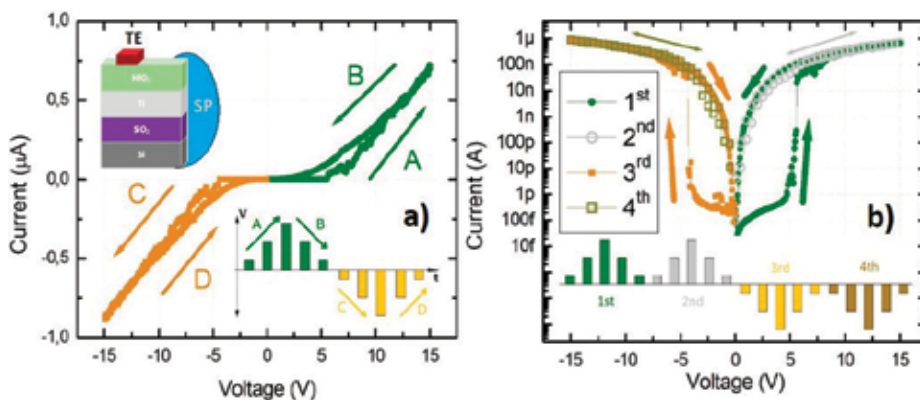**Figure 1.** (a) Current as a function of voltage (I-V) measured with a pulsed sweep (see lower right inset). The upper left inset sketches the stack (TE stands for top electrode while SP is the way to access to the bottom contact of the structure). (b) I-V curve displayed in semi-logarithmic scale. As can be seen from the inset, the protocol consists in two repetitions of each polarity sweep in order to test the nonvolatile behavior.

one, and the other SET operation is recorded each time the voltage reaches ~ 5 V. After a negative polarity sweeping loop, the positive HRS is recovered at the positive stimulus.

It is worth to point out that even when no trace of a RESET operation was observed, just upon zero voltage crossing the rectifying capability of these devices rebuilds a high-resistance level.

Memristive cells are classified into bipolar and unipolar behavior. Bipolar cells are those which demonstrate the SET and RESET operations in opposite voltage polarities, for example, SET at positive polarity and RESET at negative voltage. In turn, in unipolar cells the SET and RESET can occur at the same polarity (while other parameters need to be controlled, i.e., current compliance). Whether both polarities are required to operate the memristive cells or not is determined by the mechanism governing the switching. Despite the difference, typical memristive cells (being either bipolar or unipolar) depict crossing I-V curves, a behavior qualitatively different from the one obtained in our $Pd/Co/HfO_2/Ti/SiO_2/Si$ samples. So far samples showing non-crossing I-V curves were referred to as complementary RS [7]. This behavior can be modeled as the response of two coupled bipolar memristive switches in series, in a back-to-back configuration. Within this scheme, one of the two coupled memristive switches (or RS units) shows the SET operation at a positive voltage, while the other one exhibits the SET at a negative voltage. When the stimulus polarity change is produced, instead of maintaining the low-level resistance obtained during the positive excursion, it reveals the high-level resistance corresponding to the second RS unit. The coupling between the two RS units would be responsible for RESET screening. The explanation for apparent RESET absence arises on the fact that alternating the voltage polarity leads us to measure the reversed RS unit. However, if we record the resistance level between consecutive pulses (applying a small pulse of the same polarity even when the sweeping curve goes through zero), we progressively observe the changes from HRS to LRS at certain polarity and from LRS to HRS at the opposite voltage polarity. Interestingly, the back-to-back configuration determines two different pair of states: positive high- and low-resistance states (pHRS and pLRS, respectively) and equivalently for negative polarity (nHRS and nLRS).

By following the resistance level, measured in between every two consecutive pulses during the pulsed voltage sweep (green pulses in **Figure 2b** and **d**), the specific voltage values at which the SET and RESET occur (identified as the changes from HRS to LRS, and from LRS to HRS, respectively) can be identified. If the resistance level is recorded with a positive pulse (green pulses in **Figure 2b**), the pHRS and pLRS will be tested, while if the small pulse consists of a negative voltage value (green pulses in **Figure 2d**), the nHRS and nLRS will be under study. In that way, the two units can be split. By experimentally exploring the voltage required to observe each operation by a unique pulse (positive SET and RESET and negative SET and RESET), reduced protocols were achieved. **Figure 2b** and **d** sketch the protocols used to distinguish the two RS units. Instead of going through the whole sweep as in **Figure 1**, a unique voltage pulse is chosen to reach the LRS. In each case, positive and negative, the highest signal is used to SET the unit while the pulse with the inverted polarity is used to RESET it, and in between two pulses act as the reading voltages to quantify the resistance level. **Figure 2a** (**Figure 2c**) shows the resistance at pHRS and pLRS (nHRS and nLRS) as a function of the elapsed time. **Figure 2a** (**Figure 2c**) corresponds to applied values of +10 V (−10 V)
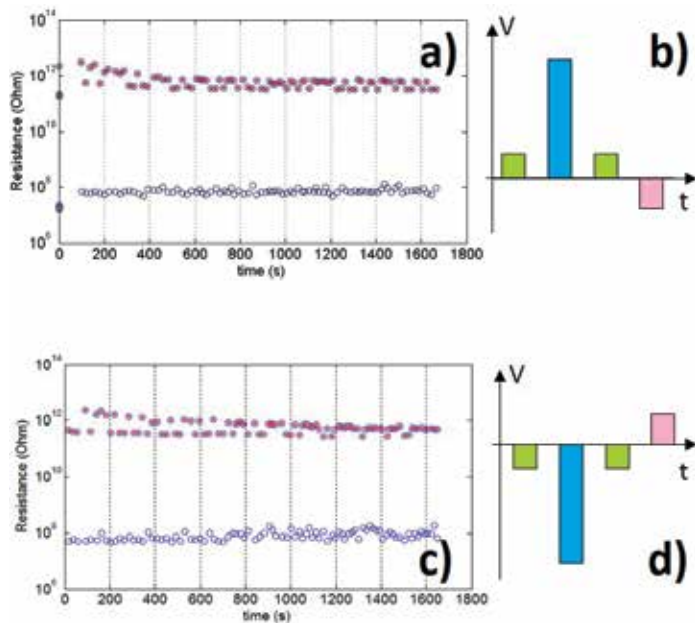
Figure 2. Resistance measured at 3 V after the SET and RESET operations for each RS unit. (a) Corresponds to pHRS and pLRS, with Vset = +10 V, Vread = +3 V, Vreset = −3.5 V (protocol sketched in (b)), while (c) represents nHRS and nLRS, with Vset = −10 V, Vread = −3 V, Vreset = +3.5 V (protocol sketched in d).

for SET operation and − 3.5 V (+3.5 V) for RESET while the resistance is recorded in between at +3 V (−3 V). All applied pulses last for 5 ms. Resistance levels measured at +3 V and − 3 V can be recognized as the two possible states displayed by the hysteretic curves shown in **Figure 1**. Although some dispersion can be appreciated within each defined state (pHRS, pLRS, nHRS, and nLRS), the rate between each pair of HRS and LRS remains of four orders of magnitude for at least 2000 repetitions.

To gain further insight into the electrical response of the device, we performed capacitance measurements. Capacitance is a differential quantity that has to be recorded applying an AC voltage; frequency and amplitude (levels) are the parameters of such an AC signal. To quantify the capacitive contribution an electrical model is required. Two different models considering a capacitor and a resistor were employed: serially and parallely connected. In both cases, the capacitive term was equivalent pointing out the predominance of the capacitive over the resistive term. An LCR meter Agilent E4980 parameter analyzer was used to perform the measurements in a two-terminal configuration connected through coaxial wires to a probe station with a heating system.

Figure 3b was obtained applying a 100 kHz–100 mV AC signal while sweeping a superimposed DC voltage. Most relevant conclusions are obtained under different polarization conditions or bias (DC voltage). Remarkably, no change of the capacitance is observed even though the applied DC sweep goes through the values expected to switch the electrical resistance of the device (**Figure 3a**) includes an I-V curve for comparison). Such independence as a function

of DC bias is usually attributed to a parallel-plate capacitor, that is, a MIM stack. Instead, two RS units are supposed to take part in a complex scenario of different states. The measurement of a constant value implies that whatever the involved switching mechanism is, at least the capacitive component will remain unaffected. Moreover, recording C-V at different frequencies and/or temperatures (**Figures 3c** and **4a**, respectively) also exhibits a value independent on the bias.

It is worth pointing out that capacitance appears unaffected by DC stimulus but is strongly dependent on the two additional parameters analyzed: AC frequency and temperature, **Figures 3c** and **4a**, respectively. Since we are using a resistor-capacitor (RC) model and the comparison between the capacitance determined from a parallel array coincides exactly with the one measured considering a series array, the capacitive term seems to indicate an intrinsic feature of the stack. Within this scenario, in a simple RC circuit, capacitances should correspond to the imaginary part of the complex impedance, at the so-called reactance term. The capacitive reactance depends on capacitance and frequency. However, once the capacitance term was identified, the simplified variable should not depend on the frequency. Usually, the dependence of this parameter of frequency is attributed to a wrong determination of the capacitive term and is more notorious in the high-frequency regime [11]. In this case, the full range of available frequencies (from 2 Hz to 1 MHz) was explored, obtaining a monotonous dependence. **Figure 3c** demonstrates the frequency-dependent capacitance by plotting C recorded at four selected fixed frequencies as a function of voltage (each of them, in turn, independent from bias).

Regarding the measurements as a function of temperature, such dependence (**Figure 4a**) reminds us of a semiconductor material since the amount of available carriers increases [16]. However, as we mentioned, the constant capacitance is the signature of a MIM-like stack. How to reconcile an MIM indication, of an invariable capacitance as function of bias, with a semiconductor-like dependence with the frequency? Where does the semiconductor nature
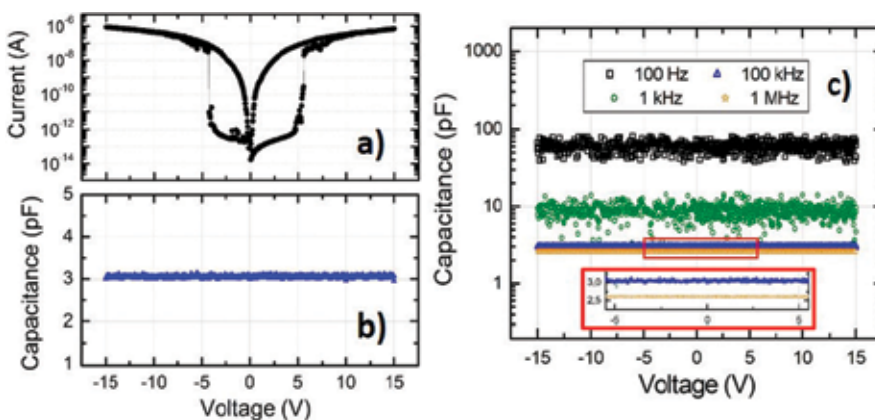

Figure 3. Capacitance as function of bias voltage (C-V) recorded at 100 kHz and room temperature (b). The upper panel (a) offers a reference with the switching observed during an I-V excursion. (c) C-V measured at room T under different AC frequencies.

arise from? Some works report a semiconducting behavior of HfO_2 at HRS [17] but since no change is observed beyond the SET value this cannot be a satisfactory explanation. To have a deep insight on this issue, the LRS was analyzed as a function of the temperature (**Figure 4b**). The current flowing across the stack, measured in a two-terminal connection at +15 V, increases with temperature which evidences a nonmetallic behavior (it could be an insulator or a semiconductor). Moreover, this would be in agreement with the capacitance dependence on the temperature. Nevertheless, it remains unclear as to how to justify the flat C-V observed for the whole bias range.

Beyond the mentioned dependencies, the absolute value of capacitance deserves to be discussed. If we proceed by considering a parallel-plate capacitor (Eq. (2)), as suggested from the C-V flat trend, the dielectric constant of HfO_2 could be found considering the area and thickness as known parameters. Eq. (2) is the capacitance attributed to a parallel-plate capacitor with metal electrodes of area A, a dielectric material characterized by ε_r (dielectric constant referred to the vacuum permittivity ε_0), and thickness t:

$$C = \frac{\varepsilon_0 \varepsilon_r A}{t} \qquad (2)$$

However, such estimation offers in all the cases (different frequencies and temperatures) extremely low values of ε_r compared with the one expected ($\varepsilon_r = 0.005$ calculated from experimental data against $\varepsilon_r = 20$ which was expected [18]). Even though a certain dispersion could be a reasonable (i.e., related with the particular deposition method), the estimated difference exceeds in orders of magnitude of the spread so far reported. Devices with different areas, HfO_2 thicknesses, and TE materials were also measured supporting the dielectric constant obtained in samples with 20 nm-thick HfO_2 and square (200 μm^2) side top electrodes. **Figure 5** includes data from all those devices, showing capacitance scales as expected with area but not with thickness. In fact, three different HfO_2 thicknesses were measured presenting the same absolute value. This independency with the HfO_2 thickness suggests either that the
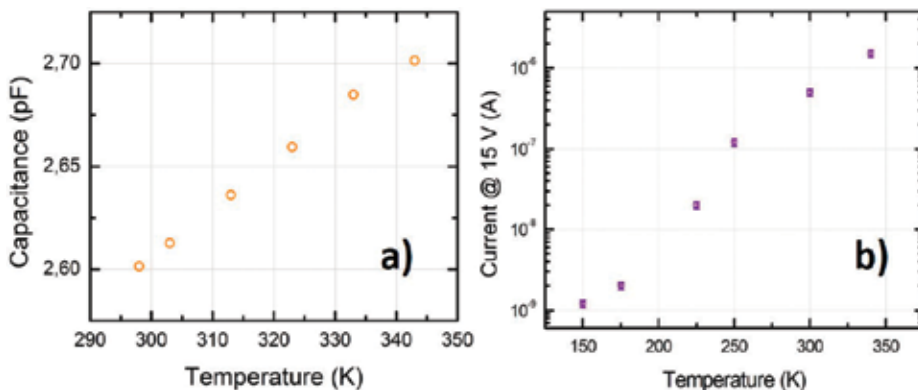

Figure 4. (a) Capacitance as function of temperature. Each point represents the average value obtained within the ±15 V bias range. (b) Resistance measured at +15 V (pLRS) as function of temperature. The decrease is usually attributed to a nonmetallic behavior.

model is incorrect (capacitance does not originate from the TE/HfO$_2$/Ti like in a parallel-plate capacitor fashion) or that HfO$_2$ is not the dielectric of the capacitor that governs the general trend. Importantly, also, Au electrodes were tested without remarkable differences. Although a semiconductor behavior is deduced from the temperature dependence, a capacitive term related with some depletion layer formation is ruled out since the C-V trend should follow the width modulation with bias.

Another interesting issue is extracted from the extrapolated intercept in **Figure 5**. A zero intercept is expected when a pure capacitor is measured. Instead, a nonzero value is related with an extra contribution usually from unconsidered terms, such as interfacial effects. However, if an interfacial effect is suspected, that should not be at the TE interface since the two explored materials seem to converge to the same intercept. The possibility of a nonzero intercept also highlights the need of measuring many areas in order to get the real slope. The upper-left inset demonstrates the difference between point-to-point slope determination and the real one provided by the area dependence.

So far, the capacitance dependence does not follow the expected trend with HfO$_2$ thickness. In addition, the absolute value of the measured capacitance appears not to be related with the dielectric constant usually attributed to such materials. Something else determines the capacitive behavior, although a depletion layer formation was discarded based on the absence of dependence with bias voltage. Moreover, two different memristive cells were necessary to explain the non-crossing feature and the impossibility of appreciating RESET operations. There is no clue yet about where those RS units, acting as junctions, are located. However, once more if we consider two different elements a plausible picture is obtained. **Figure 5c** sketches two M-I-S (metal-insulator-semiconductor) devices connected in series. As it is well-known the sum of capacitors in series is governed by the smaller term, because the sum
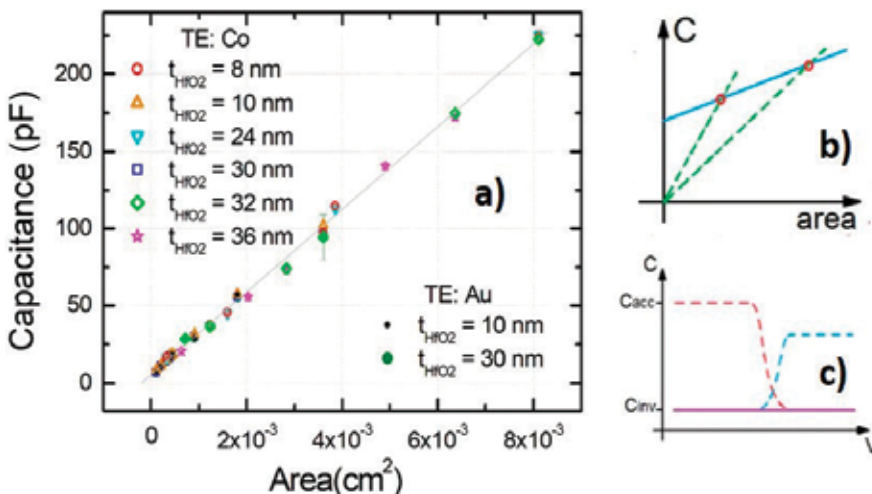

Figure 5. (a) Capacitance as function of area, including many different samples measured at 100 kHz. Capacitance scales as expected with area while no variation is observed for different HfO$_2$ thicknesses. Considering different TE's material does not reflect changes. (b) Sketch of a proposed explanation for the behavior observed in **Figures 3**, **4** and **5a**).

corresponds to the inversion value for each MIS. Since the inversion value of capacitance is not directly related to the dielectric material but to the semiconductor properties, that offers a possible explanation for the independence with HfO_2 thickness. Also, given the fact that the semiconductor rules the absolute capacitance value, the temperature dependence can be satisfactory understood.

Interestingly, the accuracy of such an explanation arises on the fact of considering two MIS stacks with opposite-doped semiconductors but exactly the same flat-band condition, which means the voltage required to exactly compensate the band bending. That voltage is the one at which the change between accumulation and depletion occurs. Now, two new questions appear:

1. Why should the inversion capacitance for both MIS stacks be coincident? and

2. Why they switch from accumulation to inversion and vice versa at the very same voltage?

In the following we will try to identify the origin of these two elements within the stack composition to answer these questions.

2.2. Structural characterization

In order to determine each layer's thickness, roughness, and density within the obtained stack, X-ray reflectivity (XRR) was recorded. Since the top electrodes are patterned, that is, Pd/Co does not constitute a uniform layer, the samples studied by XRR do not have the metal cover. This technique distinguishes materials by their electronic density. A typical measurement consists of the grazing incidence of X-rays, starting with total reflection and followed by a pronounced decrease identified as the critical angle, when the X-rays start penetrating the material. Following oscillations are related to the interference pattern produced by the interference of X-rays reflected by the different interfaces present within the sample under study. The critical angle and the period are directly related to the density of the material on top and the total thickness, respectively. Further estimations require a model and, by fitting it, a deeper comprehension of the stack can be achieved. **Figure 6a** includes XRR experimental data and a fitting. The experimental data are shown normalized by the Fresnel coefficient ($R_F = 16\pi^2/Q^4$) and the x-axis uses the propagation vector (Q) instead of 2θ. The good agreement between experiment and fitting provides a reasonable confidence about the conclusions extracted from it. It is worth pointing out that some parameters were previously determined in order to reduce the parameter space and get a physical representative set of values, that is, the HfO_2 roughness was fixed as the value obtained from atomic force microscopy (not shown). Results are summarized in **Table 1**.

As discussed, the contrast in this X-rays technique is related with the electronic density of the materials. This feature makes it impossible to distinguish between Ti and TiO_2 layers. However, an important conclusion has to be highlighted; the Ti-related layer is 50% thicker than what it was supposed to be. Since the accurate control of Ti sputter deposition can be assured, this could consist of an indirect proof of oxidation.
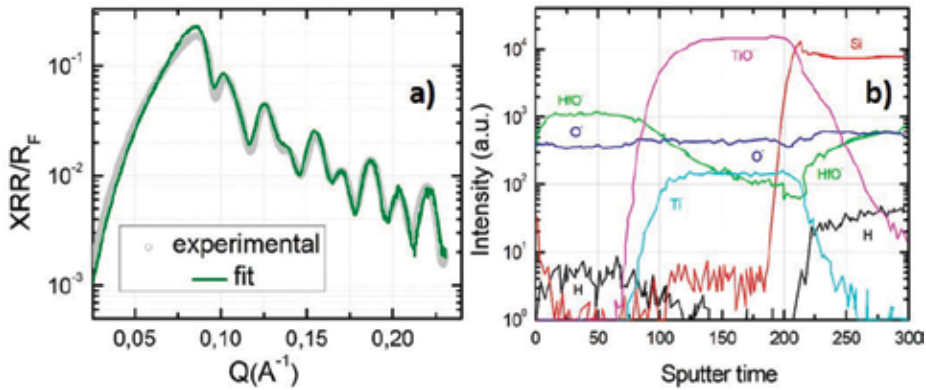
Figure 6. (a) X-ray reflectometry normalized with Fresnel coefficient ($R F = 16 \pi 2/Q 4$) as a function of the incident propagation vector. A good agreement between experimental and fitting is achieved. (b) Secondary ion mass spectroscopy (SIMS) as a function of elapsed sputtering time. During the etching of the sample the signals of the expected species are recorded. The intensity, in logarithmic scale, relates with the relative presence of each compound while deeper layers are reached as sputter time passes through.

	Parameter	From fitting	Expected
HfO_2	Thickness [nm]	26.5	20
	Roughness [nm]	Not fitted	1 (AFM determined)
	Density [g/cc]	10.1	10.12
Ti/TiO_x	Thickness [nm]	27.8	20
	Roughness [nm]	0.6/1.,9	—
	Density [g/cc]	4.3/3.8	4.50/4.25
SiO_2	Thickness [nm]	45.9	120
	Roughness [nm]	0.3	—
	Density [g/cc]	2.5	2.65

Table 1. Summary of parameters obtained from XRR fitting compared with expected values.

Note that for the underlying SiO_2 layer the obtained density is quite precise. However, we did not expect the proper thickness for that layer because the angular resolution limits the maximum accessible value (usually below 150 nm).

To define whether a pure Ti or a TiO_2 layer is present, secondary ion mass spectroscopy (SIMS) was performed at room temperature (**Figure 6b**). This is a destructive technique in which an Ar beam impacts the sample detaching its constituent atoms, which are collected by a detector. In this way, as the Ar beam etches the surface progressively, a profile composition is obtained (depending on the etching rate, the time variable can be regarded as the depth function). Starting with an exposed HfO_2 layer, as the sputter time increases, traces attributed to deeper layers can be observed. When the HfO^- signal decreases, Ti and TiO^- traces

increase pointing out the interface location. **Figure 6b** allows one to recognize oxygen presence through the full titanium layer. Complete oxidation of the titanium layer implies an absence of the Ti bottom electrode and, in that case, the bottom electrode would be formed by the highly doped silicon substrate. According to such an observation, and as it was suggested by electrical measurements, a thicker dielectric material has to be considered.

2.3. Additional deposition process

Thus, both electrical and chemical evidence indicate a clear layer modification by which the stack is significantly modified compared to the designed stack. Nonetheless, RS was positively affected in the way that some desirable properties were improved. From the technological point of view, extremely low leakage currents, free-forming behavior, complementary bipolar junctions, and low power consumption are at the core of qualities that the next memory generation has to achieve. All these properties were attained by samples presented herein (for more details see Ref. [19]). Thus, it is of paramount importance to disentangle the oxygen source and metal precursor effects of the ALD HfO_2 process on the titanium oxidation.

So far, ALD HfO_2 deposition has not been reported for such underlying layers' modification. To validate our hypothesis about O_3 influence, an additional fabrication proposal was dealt with. The aim of such exploration is to use H_2O instead of O_3 as an oxygen source, maintaining the hafnium precursor as before. As shown in **Table 2**, different combinations of layer thicknesses were explored. Thicker and thinner Ti layers (than the one used in the initial batch) will allow us to understand the impact of oxygen diffusion on the Ti metal-layer oxidation. Also, different HfO_2 thicknesses will help to clarify whether the ALD cycles, the temperature persistence, or the longer diffusion times give rise to the discovered oxidation of the full Ti layer.

2.4. Microscopic picture beyond the macroscopic behavior

Structural and electrical characterizations do not show any significant variation with respect to usual HfO_2-based RS devices reported elsewhere [20, 21]. All of them show a forming requirement and are needed to be externally limited to avoid current runaway. After the forming operation, states of high power consumption (mW) were observed. Besides, no

SiO$_2$ thickness	Ti thickness	HfO$_2$ thickness	Access to BE
120 nm	20 nm	10 nm	Scratch
120 nm	20 nm	20 nm	SiO$_2$ removal from back contact
120 nm	10 nm	20 nm	Scratch
120 nm	20 nm	20 nm	SiO$_2$ removal from back contact
120 nm	—	20 nm	Scratch
120 nm	—	—	Scratch

Table 2. Details of complementary batch designed to disentangle oxidant and/or precursor effects.

double rectification was appreciated within the new batch. All those remarkably features, highlighted as desired in the former case (with ozone as oxidant), seem to be related with the TiO_x layer formed in the experiments. **Figure 7** constitutes one example of the referred characteristics: forming operation, no-self limitation, and crossing behavior. Moreover, Yoon et al. [22] who follow a similar deposition process (O_3-based ALD-deposited HfO_2 over a Ti layer) demonstrate current-voltage dependence strikingly similar to that reported here. Although they attribute such behavior to the interface quality, structural analysis is missing, leading to thinking about an effect of Ti oxidation (in the following referred to as TiO_x), analogous to what was demonstrated in this study. **Figure 8** summarizes the subsequent steps that would explain the proposed stack composition of the ozone-based samples.

In this framework a picture of the involved mechanism in such unusual switching is required. Since the resultant stack was shown to be composed by a multilayer insulator (20 nm of HfO_2, 30 nm of TiO_x and 120 nm of SiO_2), it is hard to justify any reversible switching operation.

We will now focus on the role of the SiO_2 dielectric layer, which was thermally grown from the very initial Si wafer.

Thermal oxidation is closely related with semiconductor doping. Si doping, related with wafer resistivity (4–40 mΩ cm, provided by the manufacturer), is about 4.10^{18}–4.10^{19} cm^{-3} and allows one to understand that although a semiconductor behavior is expected, such high doping screens its nature. Within this scenario Si behaves like a metal and explains capacitance independence with respect to bias stimulus. Nonetheless, this issue hinders capacitance-temperature dependence explanation. Besides, a highly doped semiconductor affects the growth rate [23] and the impurity content of the resultant oxide [20]. This explains the current flow across a 200 nm dielectric as trap assisted [16] and justifies such a low current level, even at LRS.

Within a multilayered dielectric, the voltage drop on each layer (Eq. (3)) is subjected to each layer's permittivity, ε_l [24]. Although such an estimation seems very complex in this situation,
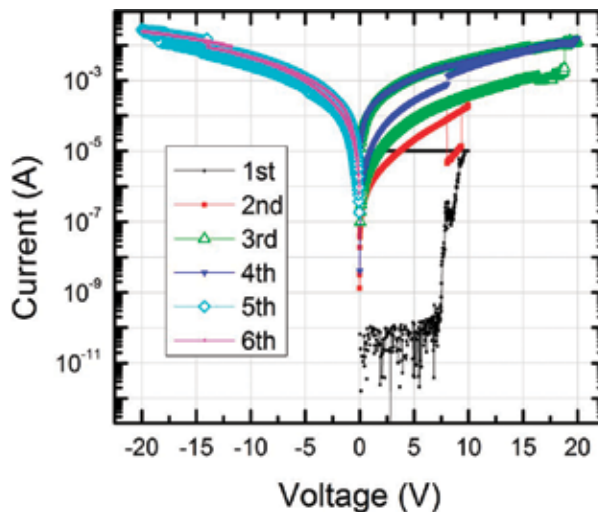

Figure 7. Prototypical behavior of one sample SiO_2 (120 nm)/Ti (10 nm)/HfO_2 (20 nm)/Pt of the new fabrication process. After the first voltage excursion, the device is found in an irreversible low resistance state.
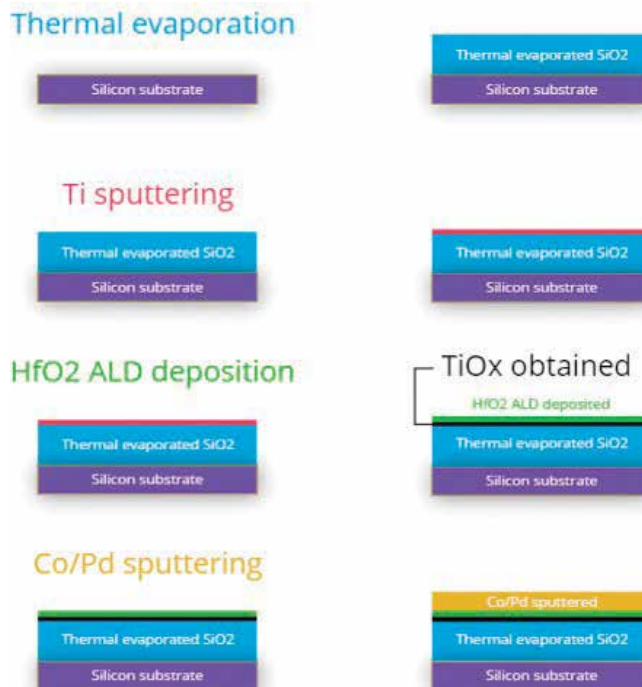
Figure 8. Sketch of process flow and the changes produced during ALD process using ozone as oxidant.

at least it is possible to argue that HfO_2 has a higher permittivity than it was ever reported to SiO_2 [20] and lower than what could be attributed to TiO_2 and its related sub-oxides (generally denoted as TiO_x [25, 26]). **Table 3** presents an estimation of voltage drops on each dielectric sub-layer. This means that most of the voltage drop is restricted to the SiO_2 layer avoiding HfO_2 and/or TiO_x to be formed and/or switched.

$$V_i = \eta_i . V_T, \quad \text{where} \quad \eta_i = \frac{t_i}{\varepsilon_i} . 1/\Sigma_i \frac{t_i}{\varepsilon_i} \tag{3}$$

The situation could be summarized as follows: a multilayered dielectric sandwiched between two metal-like electrodes (Pd/Co and highly doped Si) shows RS. Such behavior cannot be explained by usual HfO_2 or TiO_2 switching because of the voltage drop competition, associated with their individual dielectric constants. On the other hand, Eq. (3) relies on the fact that no charges are present at the interfaces and, consequently, no voltage drop is expected in those regions. It is not clear whether this assumption is correct or not but even if so, the voltage drop on the HfO_2 and/or TiO_x should be indeed lower than considered (making harder the switch of each layer).

We can also use the impedance spectroscopy (IS) technique to deepen the understanding of the mechanisms involved in the resistive switching. In this particular case, to measure the impedance, in the range 100 Hz–10 MHz, we set the oscillator amplitude of the impedance analyzer to 5 mV and applied a DC bias of 3 V. In this context, the obtained results for the complex impedance are presented in a complex plane plot usually called the Nyquist diagram [27],

Material	ε_i	Thickness (nm)	V_i (V)
HfO$_2$	20	10	0.24
TiO$_x$	80 (40)	30	0.18 (0.36)
SiO$_2$	3.9	120	14.58 (14.40)
Total		*160*	*15*

Table 3. Voltage drop on each dielectric sublayer. Quantities between parentheses indicates voltage drop variation depending on the permittivity attributed to TiO$_x$.

where minus the imaginary part of the impedance is plotted as function of the real one. In **Figure 9a** and **b** the Nyquist diagrams corresponding to pHRS and pLRS are shown. In these plots, each point corresponds to the imaginary and real components of the impedance at different frequencies. It is interesting to remark that the capacitive behavior of the measured devices is evidenced by the negative values of the measured imaginary part of the impedance. If a model is proposed for the equivalent circuit of the device, the value of each equivalent component can be found.

In **Figure 9a** and **b**, the inset show the equivalent circuit used to model the impedance of each state. In the pHRS (**Figure 9a**), two blocks connected in series were necessary to properly fit the measurements while only one was required in the pLRS case (**Figure 9b**). Both the low- and high-resistance states have a common block composed of a resistor in parallel to a constant-phase element (CPE) [27]. In addition, the high-resistance state has also another block constituted by a resistor in parallel with a capacitor. The obtained values for all these elements are summarized in **Table 4**. A CPE is an artificial way of representing a wide dispersion of characteristic times. It can be thought as a capacitor but instead a unique resonant condition, a dispersion of them (usually related with different species underneath), is taken into account. Its mathematical expression is given by $Z_{CPE} = A\,(j\omega)^{-\alpha}$ where A and α are related specifically with the system, while ω is the angular frequency.
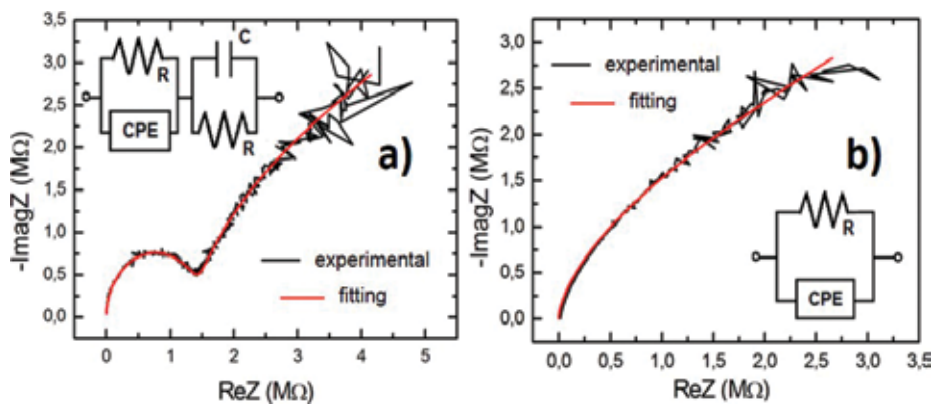

Figure 9. Nyquist plot constructed from impedance measurements under +3 V bias and 5 mV AC signal in (a) pHRS, and (b) pLRS.

		pHRS	pLRS
R-CPE	R	$1.1.10^7$ Ω	$9.6.10^6$ Ω
	m (CPE)	0.71	0.74
	p (CPE)	$3.7.10^{-10}$	$2.8.10^{-10}$
R-C	R	$1.3.10^6$ Ω	—
	C	$4.7.10^{13}$ F	—

Table 4. Parameters of the models used to fit the Cole-Cole diagrams of **Figure 9a** and **b**.

In this case, we will not focus on the model for each state (pHRS and pLRS) but in the comparison of them. It is worth to point out that an equivalent behavior was obtained also in the comparison of the nHRS and nLRS. For that reason, in the following, we will refer generically to HRS and LRS even though only the positive case is being presented. Our aim is to get a more detailed comprehension of the switching behind the macroscopic behavior. Compared with **Figure 9a**, experimental data of **Figure 9b** could be mimicked with only one of the two arrays mentioned before. It seems that the LRS maintains the wide dispersion of species that gives rise to the CPE element while the parallel capacitor-resistor block disappeared. This finding, together with the fact that the parallel resistor-CPE remains constant, reveals that a diode has been overcome. A block consisting of a parallel capacitor-resistor is the usual model to represent a diode below the forward-biased threshold. Thus, the removal of that block to model the LRS implies a diode-like behavior during the HRS and consequently a barrier to overcome in order to get the conductive condition.

Finally, we suggest a plausible mechanism for switching operation: TiO_2 interfaces with HfO_2 and SiO_2 could play the role of a barrier, originating two junctions. Band bending would assist the current to flow through one of them, while the other has to be overcome after charge trapping had taken place. That would offer possible states in the forbidden gap to the electrons. A condition for which this happens could be related with each sharp switching operation (observed in I-V dependence). This could be the reason why half of a loop in the DC I-V curve was also identified in Ref. [22]. In that case, TiO_x had only one interface with an oxide suitable to be switched. Thus, a trapping-based mechanism would be attributed to such behavior which cannot be reflected by capacitance measurements. In such a way, no capacitance change could be expected. Moreover, the TiO_x semiconductor nature would explain the capacitance-temperature dependence that we observed. It is worth to point out that resistive switching mechanisms without ion movement requirement have attracted attention since it would be less downgrading to the memory cell neighborhood, in terms of chip integration [28].

3. Conclusions

We described the ALD technique in detail, pointing out many interesting, efficient and unique capabilities. Besides, we highlighted the problem found when there is an interaction of a

material to be deposited or the precursors used in its growing process, with the pre-deposited layers on the substrate. We exemplified the case describing a particular case, where the non-volatile memory device of the ReRAM type was grown.

The ALD technique was used to obtain HfO_2-based devices with some remarkable features. The use of different precursors, and the fact that a non-negligible interaction between these precursors and pre-existent stacks could produce unconsidered phases, has been discussed in detail. A careful analysis of the device's structure (initially suggested by difficulties in the understanding of measured electrical features) triggered the comprehension of the actual structure of the device. An additional oxide layer was formed because the precursor reacted with the buffer material, giving rise to a completely different stack. Remarkably, this fact rendered advantageous properties which could be useful in the field of multifunctional memory applications.

While an MIM stack was expected (consisting of $Pd/Co/HfO_2/Ti$), a post-deposition structural characterization proved oxidation of the metallic layer underlying the ALD-deposited oxide. Using water instead of ozone as an oxidant allowed to attribute titanium oxidation to the very high reactivity of the oxidant primary employed. Once the complete stack composition was determined, a feasible scenario about the switching mechanism was proposed. This gathers the evidence obtained, through electrical and structural measurements, in a unique picture that captures all features highlighted within memory behavior.

Acknowledgements

Conflict of interest

The authors do not declare any conflict of interest.

Notes/thanks/other declarations

This chapter is part of the thesis "Óxidos delgados para micro y nanoelectrónica: degradación, ruptura y aplicaciones tecnológicas" in Spanish by C.P. Quinteros at Buenos Aires University, presented in March 2016 (http://digital.bl.fcen.uba.ar/gsdl-282/cgi-bin/library.cgi?a=d&c=tesis&d=Tesis_5923_Quinteros).

Author details

Cynthia P. Quinteros[1,2]*, Alex Hardtdegen[3], Mariano Barella[4], Federico Golmar[4,5],
Félix Palumbo[6], Javier Curiale[7,8], Susanne Hoffmann-Eifert[3] and Pablo Levy[1]

*Address all correspondence to: cpquinterosdominguez@gmail.com

1 CNEA, CONICET, Centro Atómico Constituyentes, San Martín (Buenos Aires), Argentina

2 Actually at Nanostructures of Functional Oxides, ZIAM, University of Groningen (RUG), Groningen, The Netherlands

3 Forschungszentrum Jülich, Jülich, Germany

4 CMNB – INTI, CONICET, San Martín (Buenos Aires), Argentina

5 ECyT – UNSAM, San Martín (Buenos Aires), Argentina

6 UTN - FRBA, CONICET, Buenos Aires city, Argentina

7 CNEA, CONICET, S. C, Bariloche (Río Negro), Argentina

8 Instituto Balseiro, UNCuyo - CNEA, S. C, Bariloche (Río Negro), Argentina

References

[1] George SM. Atomic Layer Deposition: An Overview. Chemical Reviews. 2010;**110**(1): 111-131

[2] Franssila S. Introduction to Microfabrication. Chichester, England: Wiley; 2004. p. 331

[3] Ohring M. Materials Science of Thin Films. Chapter 6, 2nd ed. Amsterdam, The Netherlands: Elsevier; 1991

[4] Choi JH, Mao Y, Chang JP. Development of hafnium based high-k materials—A review. Materials Science & Engineering R: Reports. 2011 Jul 22;**72**(6):97-136

[5] Li Y-L, Chang-Liao K-S, Li C-C, Chen L-T, Su T-H, Chang Y-W, et al. Electrical and physical characteristics of high-k gated MOSFETs with in-situ H_2O and O_2 plasma formed interfacial layer. Microelectronic Engineering. 2015 Nov 1;**147**:67-71

[6] Ielmini D, Waser R. Resistive Switching: From Fundamentals of Nanoionic Redox processes to Memristive Device Applications. New Jersey, US: Wiley, Hoboken; 2015 p. 787

[7] Linn E, Rosezin R, Kügeler C, Waser R. Complementary resistive switches for passive nanocrossbar memories. Nature Materials. 2010 May;**9**(5):403-406

[8] Herpers A. Electrical characterization of manganite and titanate structures [PhD]. [Forschungszentrum Juelich]; 2014

[9] Chasin A. High-performance a-IGZO thin film diode as selector for cross-point memory application. IEEE Electron Device Letters. 2014;**35**(6):642-644

[10] Zazpe R, Stoliar P, Golmar F, Llopis R, Casanova F, Hueso LE. Resistive switching in rectifying interfaces of metal-semiconductor-metal structures. Applied Physics Letters. 2013 Aug 15;**103**(7):073114

[11] Nicollian EH, Brews JR. MOS (Metal Oxide Semiconductor) Physics and Technology. New Jersey (US): Wiley; 1982. p. 222

[12] Sbiaa R, Meng H, Piramanayagam SN. Materials with perpendicular magnetic anisotropy for magnetic random access memory. Physica Status Solidi RRL – Rapid Research Letters. 2011 Dec 1;**5**(12):413-419

[13] Vermeulen BF, Wu J, Swerts J, Couet S, Linten D, Radu IP, et al. Perpendicular magnetic anisotropy of Co\Pt bilayers on ALD HfO_2. Journal of Applied Physics. 2016 Oct 28;**120**(16):163903

[14] Park MH, Lee YH, Kim HJ, Kim YJ, Moon T, Kim KD, et al. Ferroelectricity and anti-ferroelectricity of doped thin HfO_2-based films. Advanced Materials. 2015 Mar 1; **27**(11):1811-1831

[15] Qingjiang L, Khiat A, Salaoru I, Papavassiliou C, Hui X, Prodromakis T. Memory impedance in TiO_2 based metal-insulator-metal devices. Scientific Reports. 2014 Mar 31;**4**

[16] Sze SM. Physics of Semiconductor Devices. Chapter 7, 2nd ed. New York, US: Wiley; 1981

[17] Mahapatra R, Maji S, Horsfall AB, Wright NG. Temperature impact on switching characteristics of resistive memory devices with HfOx/TiOx/HfOx stack dielectric. Microelectronic Engineering. 2015 Apr 20;**138**:118-121

[18] Martínez-Domingo C, Saura X, Conde A, Jiménez D, Miranda E, Rafí JM, et al. Initial leakage current related to extrinsic breakdown in HfO_2/Al_2O_3 nanolaminate ALD dielectrics. Microelectronic Engineering. 2011 Jul;**88**(7):1380-1383

[19] Quinteros C, Zazpe R, Marlasca FG, Golmar F, Casanova F, Stoliar P, et al. HfO_2 based memory devices with rectifying capabilities. Journal of Applied Physics. 2014 Jan 8; **115**(2):024501

[20] Islamov DR, Gritsenko VA, Cheng CH, Chin A. Percolation conductivity in hafnium sub-oxides. Applied Physics Letters. 2014 Dec 29;**105**(26):262903

[21] Hardtdegen A, Zhang H, Hoffmann-Eifert S. Tuning the performance of Pt/HfO_2/Ti/Pt ReRAM devices obtained from plasma-enhanced atomic layer deposition for HfO_2 thin films. Meet Abstr. 2016 Jan 9;MA2016-02(28):1885-1885

[22] Yoon JH, Kim KM, Song SJ, Seok JY, Yoon KJ, Kwon DE, et al. Pt/Ta_2O_5/HfO_{2-x}/Ti resistive switching memory competing with multilevel NAND flash. Advanced Materials. 2015 Jul 1;**27**(25):3811-3816

[23] Ho CP, Plummer JD. Si/SiO_2 interface oxidation kinetics: A physical model for the influence of high substrate doping levels. II. Comparison with experiment and discussion. Journal of the Electrochemical Society. 1979 Jan;**126**(9, 9):1523-1530

[24] Quinteros CP, Palumbo F, Campabadal F, Miranda E. Stress conditions to study the reliability characteristics of high-k nanolaminates. ECS Transactions. 2012 Aug 30;**49**(1):161-168

[25] Szot K, Rogala M, Speier W, Klusek Z, Besmehn A, Waser R. TiO_2—A prototypical memristive material. Nanotechnology. 2011 Jun 24;**22**(25):254001

[26] Robertson J. High dielectric constant oxides. European Physical Journal Applied Physics. 2004;**28**(3):265-291

[27] Barsoukov E, Macdonald JR. Impedance Spectroscopy: Theory, Experiment, and Applications. 2nd ed. Wiley

[28] Mehonic A, Cueff S, Wojdak M, Hudziak S, Labbé C, Rizk R, et al. Electrically tailored resistance switching in silicon oxide. Nanotechnology. 2012 Nov 16;**23**(45):455201

Mechanisms of Significant Precipitation Hardening in a Medium Carbon Bainitic Steel by Complex Nanocarbides Composed of Nb, Ti and V

Makoto Okonogi, Takuya Hara and Hiromi Miura

Additional information is available at the end of the chapter

Abstract

Precipitation-hardening behavior of various medium carbon bainitic steels with added elements of Nb, Ti and V was systematically investigated. Complex nanocarbides composed of Nb, Ti and V precipitated after aging in the steel with multiple additions of all the elements, whereas those with added individual elements were simple MC types. The amount of precipitation hardening (ΔHv) after aging at 873 K of the former steel was approximately 90 ΔHv, while those of the latter were less than 40 ΔHv at best. Therefore, significant precipitation hardening took place by multiple element addition. The different amount of precipitation hardening depending on added elements was reasonably understood by considering misfit parameters between carbides and ferrite matrix.

Keywords: medium carbon steel, precipitation hardening, carbide, misfit parameter

1. Introduction

For machinery parts, such as bolts and gears, medium carbon steels are regularly employed. These steel parts are generally formed to prescribed shapes and designs through thermomechanical processes of hot and/or cold forging, and machining followed by heat treatments for further strengthening. Recently, demands for high strength steels, with their reduction of cost in addition to superior balance of mechanical properties, are increasing.

The dispersion of hard particles should be one of the most effective methods for strengthening. For this purpose, microalloyed steels with dispersed fine carbides are developed and actually employed for machinery parts because of their good balance of formability and strengthening

by heat treatment after the forming. It is reported that the dispersion of fine carbides such as VC, NbC, TiC and Mo$_2$C is effective for strengthening of low carbon ferritic and martensitic steels [1–3].

From the above background, some researches on precipitation-hardened medium carbon steels have been also undertaken. Murase et al. have investigated the precipitation-hardening behavior of medium carbon ferritic steels with single or multiple element additions of V and Cu [4] and have found that precipitation hardening of medium carbon steels is obviously improved by the multiple element addition of V and Cu rather than single additions of each element. Grange et al. precisely examined the effect of alloying elements (such as Mn, P, Si, Ni, Cr, Mo and V) on precipitation-hardening behavior in low and medium carbon steels with tempered martensite [5] and reported that the estimated hardening Hv$_{Estimated}$ could be evaluated by simple summation of the individual hardening effects as follows:

$$Hv_{Estimated} = Hv + \Delta Hv_{Mn} + \Delta Hv_P + \Delta Hv_{Si} + \Delta Hv_{Ni} + \Delta Hv_{Cr} + \Delta Hv_{Mo} + \Delta Hv_V, \quad (1)$$

where Hv and ΔHv_{Mn}, ΔHv_P, ΔHv_{Si}, ΔHv_{Ni}, ΔHv_{Cr}, ΔHv_{Mo} and ΔHv_V are the initial hardness of Fe–C alloy before element addition and the increments in hardness due to the individual element additions. On the other hand, Kosaka et al. investigated the precipitation-hardening behavior in 0.1 C–2.0 Mn steels (in mass %) with tempered martensite and revealed that the increase in precipitation hardening due to complex-composition carbide, that is, (Mo, V)C, is larger than those by carbides with simple compositions, that is, Mo$_2$C and VC [6]. They have also shown that the effect of carbides with simple compositions on hardening becomes larger in the order of Mo$_2$C, VC, TiC and NbC. The amount of precipitation hardening would be, therefore, considerably and complicatedly changed depending on the composition of carbide.

Medium carbon steels with bainite are well known for their good balance of mechanical properties of strength and ductility [7]. They are expected to be one of the most useful steels for machinery parts in the future. However, as far as the authors know, few studies on precipitation-hardening behavior and the strengthening mechanisms due to Nb, Ti and V additions in medium carbon steels with bainite have been carried out. Here, Nb, Ti and V are the most commonly employed elements for strengthening of low carbon steels as already shown above. In the present study, the effects of compositions of carbides on the precipitation-hardening behavior of medium carbon bainitic steel and the strengthening mechanisms are precisely investigated.

2. Experimental procedure

Various kinds of medium carbon steels with different compositions, shown in **Table 1**, were vacuum induction melted and cast into 15 kg ingots. Steel A is the base sample. In steels B, C and D, elements of Nb, Ti and V, respectively, were further added to the base sample. In steel E, Nb, Ti and V were all added. Mn as well as Mo was added to all the samples to attain bainite microstructure. The casted samples were then hot forged at 1523 K into bars with a diameter of 55 mm. The bars were solution treated at 1523 K for 30 min followed by air cooling down to

	C	Si	Mn	Mo	Ni	Nb	Ti	V	N	Fe
Steel A	0.26	0.69	1.59	0.50	0.35	—	—	—	0.003	Bal.
Steel B	0.26	0.71	1.59	0.49	0.35	0.019	—	—	0.003	Bal.
Steel C	0.26	0.70	1.58	0.49	0.35	—	0.039	—	0.003	Bal.
Steel D	0.25	0.71	1.58	0.49	0.35	—	—	0.30	0.003	Bal.
Steel E	0.25	0.71	1.58	0.49	0.35	0.020	0.038	0.31	0.003	Bal.

Table 1. Chemical compositions in mass% of tested medium carbon bainitic steels.

room temperature. Thereafter, some of the bars were aged for 120 min at various temperatures between 673 and 973 K.

Microstructural observations were carried out using optical microscopy and transmission-electron microscopy (TEM) on the cross-sections normal to the longitudinal direction of bars and at the positions of the half radius of the bars. Samples for the optical microscopic observation were prepared by mechanical polishing and etching using the nital solution of 3% nitric acid and 97% ethanol. TEM specimens were also prepared by mechanical polishing followed by electrolytic polishing using a solution of 5% perchloric acid and 95% acetic acid. The size, distribution and composition of precipitated carbides were examined by TEM equipped with energy-dispersive X-ray spectroscopy (EDS). The hardness was measured using a micro-Vickers hardness tester. The amount of precipitation hardening (ΔHv) was estimated using the following equation:

$$\Delta H_V = (\text{Hardness after aging}) - (\text{Hardness before aging}) \tag{2}$$

3. Microstructure and hardness

Figure 1 shows the optical micrographs of the microstructure developed in steels D and E after solid-solution treatment at 1523 K for 30 min followed by air cooling, that is, before aging. It can be seen in **Figure 1** that a typical acicular bainite microstructure was almost uniformly evolved in both samples. A completely similar microstructure was observed to develop in all the other samples, while they are not displayed here.

The samples were then aged at various temperatures for 120 min and the change in the hardness was measured. **Figure 2** shows the summarized results of the amount of precipitation hardening (ΔH_V) as a function of aging temperature. In steels A, B and C, the maximum values of ΔH_V were approximately 30. This result indicates, therefore, precipitation hardening due to the additions of 0.019% Nb or 0.039% Ti (see **Table 1**) is quite small. On the other hand, the ΔH_V values in steels D and E after aging at 873 K exceeded 40. Moreover, in steel E, the maximum ΔH_V value was approximately 90. It should be noted, therefore, that the amount of precipitation hardening in steel E, $\Delta H_V = 90$, due to multiple element addition, is significantly larger than those in steels B, C and D with the single element additions. When the values of ΔH_V at 873 K are compared, it in steel E is larger than the summation of the ΔH_V values of
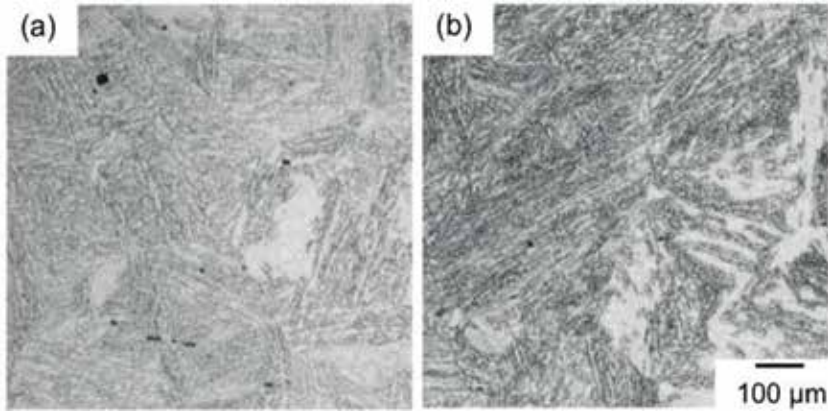
Figure 1. Typical microstructure of (a) steel D and (b) steel E after solution treatment at 1523 K for 30 min followed by air cooling.
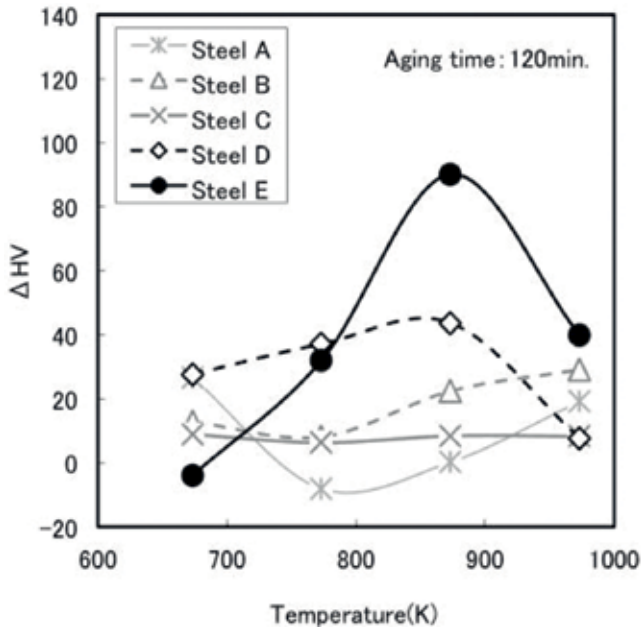
Figure 2. Change in the amount of precipitation hardening (ΔHv) depending on aging temperature and added elements.

steels B, C and D, i.e., $\Delta H_V = 73$. This result indicates that the amount of age-hardening is not a simple summation of individual hardening as described in Eq. (1).

The developed precipitates were examined by TEM. **Figure 3** shows the typical TEM photographs of steels D and E after aging at 873 K for 120 min. In steel D, fine disk-shaped precipitates of 8 nm in diameter in average were distributed (**Figure 3(a)**). On the other hand, in
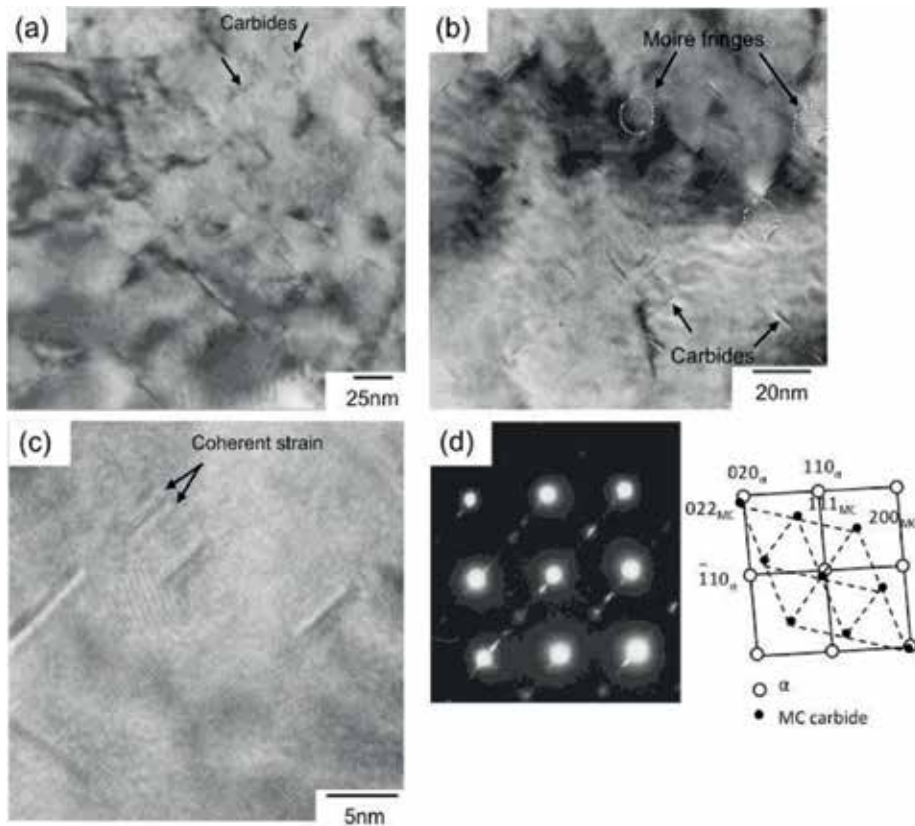
Figure 3. TEM micrographs of steels D and E after aging at 873 K: (a) Bright-field image of steel D, (b) Bright-field image of steel E, (c) magnified image of (b), and (d) diffraction pattern taken from the ferrite and MC carbide in (b).

steel E, slightly finer disk precipitates of approximately 5 nm in diameter were observed (**Figure 3(b)**). The size of precipitates in steel E looks more homogeneous than that in steel D. The moiré fringes due to the lattice misfit between the precipitates and matrix were also observed. High-resolution TEM observation of the precipitates in steel E revealed the presence of misfit strain at the edges of them indicating coherency of precipitate/matrix interface (**Figure 3(c)**). **Figure 3(d)** shows selected-area-diffraction pattern taken along direction parallel to the [001] axis of the matrix of steel E. Based on the analyses by the diffraction pattern and EDS, the fine precipitates were identified to be MC-type carbide having the Baker and Nutting crystallographic-orientation relationship, that is, $(100)_{MC}//(100)_\alpha$, $[010]_{MC}//[011]_\alpha$, and $[001]_{MC}//[011]_\alpha$ [8]. The EDS analysis indicated the compositions of carbides in steels D and E as VC and (Nb, Ti, V)C, respectively. Mo_2C carbides were not detected in all the samples.

It is reported that the critical size of MC-type carbides to keep coherency with matrix is approximately 5 nm and the loss of coherency derives a decrease in shear stress for dislocation to bypass the precipitates [3]. Even while the precipitates in steels A, B and C were not observed using TEM, the lower hardness of these steels than those of D and E (see **Figure 2**) should be affected by coherency loss of coarse MC-type carbides as observed in steel D.

4. Bypass mechanism and hardness

Precipitation-hardening behavior in medium carbon bainitic steels with added elements of Nb, Ti and V were precisely investigated. It was found that the amount of precipitation hardening became larger by the multiple element additions of Nb, Ti and V than the single addition of each element. Hardness changes due to change in dislocation bypass mechanism of particles. Even while hardness changes also depending on volume of the dispersed particles, the total amounts of particles contained in the present steels are assumed not largely different. The mechanisms of the change in the amount of precipitation hardening due to multiple element addition are precisely discussed below.

4.1. Dominant dislocation-bypass mechanism

There are two well-known mechanisms of dislocation to pass through particle at ambient temperature, that is, the Orowan [9] and the cutting mechanisms [10], which control threshold stress for dislocation motion in the particle-bearing materials. Their activation and role during plastic deformation change sensitively depending on precipitate size. Takaki has estimated the critical particle diameter for the cutting mechanism to be 7–10 nm at maximum for the MC-type carbides such as NbC, TiC and VC, whereas the Orowan mechanism can activate at ranges of 7–10 nm and over [11]. The precipitation size observed in the present study is approximately 5–8 nm in average (**Figure 3**).

When a gliding dislocation is pinned by a dispersed particle, the increase in the tensile stress ($\Delta\sigma$) can be expressed by the following equation [12, 13]:

$$\Delta\sigma = \beta Gb/\lambda \cdot \sin\theta, \tag{3}$$

where G is the shear modulus of matrix, b is the Burgers vector, λ is the mean particle spacing, θ is the bowing angle between the dislocation and the straight line that connects two particles, and β is a constant composed of Taylor's factor and the coefficient of shear stress, for which the value is approximately 3.2 [14]. The values of λ in steels D and E were measured by TEM observation to be 20 nm and 10 nm, respectively. The values of G and b are 80 GPa and 0.25 nm [14], respectively. Assuming that the tensile stress is empirically evaluated by one third of the hardness [13], the increase in the tensile stress ($\Delta\sigma$) of steels D and E can be estimated as 120 and 270 MPa, respectively, from their increase in hardness (ΔHv) 40 and 90 by aging. Finally, the θ values in steels D and E can be calculated using Eq. (3) to be approximately 2.1 and 2.4°, respectively. These values are much smaller than those of particle/dislocation interaction by the Orowan mechanism, which shows a characteristic θ value of approximately 90° [12]. The Orowan mechanism should be, therefore, not activated as the dominant dislocation bypass mechanism in the present samples.

When the carbides were examined precisely by TEM, a typical contrast owing to coherent strain as well as Moiré fringe was observed (**Figure 3**). This indicates the presence of misfit strain due to interface coherency between carbides and matrix. Miura et al. have experimentally shown that dislocation passes through incoherent particles by the Orowan mechanism and coherent particles by cutting mechanism, and the latter deformation stress is higher than

the former one [15]. From the above arguments, the activated dislocation-bypass mechanism is concluded as a cutting mechanism irrespective of the present samples. The dominant dislocation bypass mechanism is closely related with the deformation stress [15]. However, it is revealed from the above argument that the bypass mechanism itself should not cause the change in hardness in the present samples. Nevertheless, according to the criteria proposed by Takaki [11], activation of the Orowan mechanism might be partially activated for such inhomogeneously and largely coarsen precipitates observed in **Figure 3(a)**.

4.2. Origin of higher hardness due to complex carbides

Gerold and Haberkorn have theoretically shown, considering the lattice misfit parameter at precipitate/matrix interface, that the increase in shear stress ($\Delta\tau_0$) due to dislocation detachment from precipitate is expressed by

$$\Delta\tau_0 = kG|\varepsilon|^{1.5}\left(\frac{fr}{b}\right)^{0.5},\tag{4}$$

where k is a constant, f is the volume fraction of precipitates, r is the radius of the precipitate [10], ε is the lattice misfit parameter between the precipitate and matrix and ε is approximately 2/3 of the lattice misfit δ [16, 17]:

$$\varepsilon = \frac{2}{3}\,\delta,\tag{5}$$

and δ is expressed by

$$\delta = \frac{d_p - d_m}{d_m},\tag{6}$$

where d_p and d_m are the lattice constants of precipitate and matrix, respectively [10]. Eq. (4) indicates that the shear stress ($\Delta\tau_0$) increases with increasing misfit parameter, size and volume fraction of precipitates.

The complex carbides of (Nb, V)C and (Ti, V)C are known to be continuous solid solution over the entire composition range [18]. The lattice constant d_p of the complex carbide such as (Nb, V)C, (Ti, V)C and (Nb, Ti, V)C is proportional to the composition and estimated by the following equation [19]:

$$d_p = \Sigma n_i d_i,\tag{7}$$

where i denotes the alloying element (i.e., Nb, Ti and V) to compose carbide, and n_i and d_i are the expediently estimated fraction of each carbide and the lattice constant, respectively. In the present study, d_p and d_m correspond to the lattice constants of $\{001\}_{MC}$ of carbide and of $\{011\}_\alpha$ of ferrite [8].

Change in the lattice misfit parameter between the matrix and carbide could be evaluated using Eqs. (5)–(7). The calculated misfit parameter (ε) of (Nb, V)C and (Ti, V)C is displayed
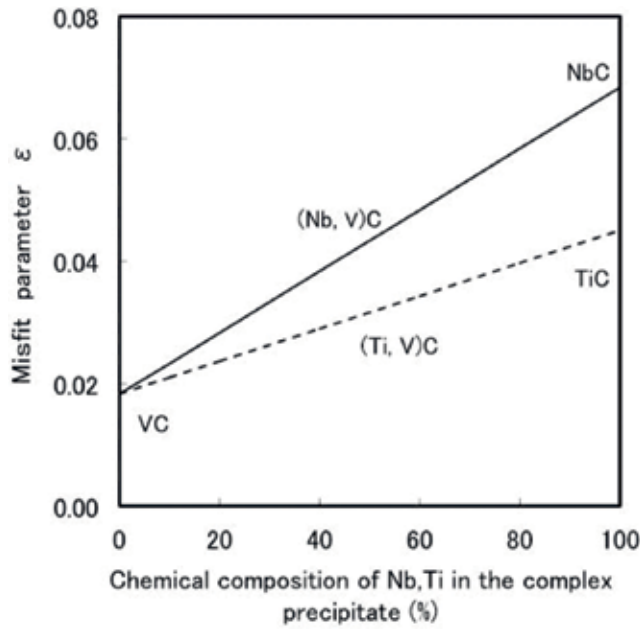
Figure 4. Calculated change in the lattice misfit parameter ε between matrix and complex precipitates of (Nb, V)C and (Ti, V)C depending on chemical composition.

in **Figure 4**. It is clear that the misfit parameter (ε) of the complex carbides (Nb, V)C and (Ti, V)C is larger than that of VC though smaller than those of NbC and TiC. Misfit parameter of (Nb, Ti, V)C complex carbide must be also linearly changed sensitively depending on the chemical composition.

In the same way, the lattice constant of (Nb, Ti, V)C complex carbide as well as the other carbides was determined. For this purpose, for an example of steel E, the chemical composition of the complex carbide at 873 K (i.e., aging temperature) was calculated to be $(Nb_{0.03}, Ti_{0.12}, V_{0.85})C$ in atomic fraction by means of the "Thermo-Calc" software using the chemical composition in **Table 1**. **Figure 5** summarizes the calculated lattice misfit parameters (ε) of the carbides precipitated in the tested samples. It is evident that the misfit parameters (ε) of (Nb, Ti, V)C is greater than that of VC and smaller than those of NbC and TiC.

Miyamoto et al. have suggested that precipitation hardening (ΔHv) due to carbides can be converted into increase in shear stress (Δτ₀) by using the Taylor's factor of 2.08 in nontextured bcc metals by the following equation [20]:

$$\Delta\tau_0 = 3 \cdot \Delta Hv/2.08, \tag{8}$$

Equation (8) indicates that the value of $\Delta\tau_0$ is proportional to precipitation hardening (ΔHv). Actually, Ronay has investigated precipitation-hardening behavior in low carbon steels and shown a linear relationship between shear stress (Δτ₀) and hardness (ΔHv) due to TiN precipitation [21]. She also reported that the increase in the hardness and, therefore, shear stress due
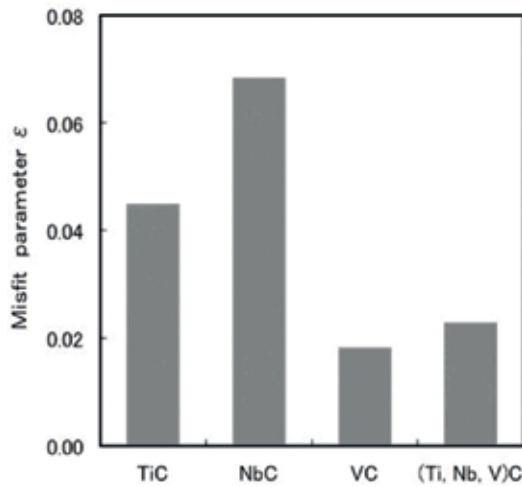
Figure 5. Comparison of the calculated lattice misfit parameter ε between matrix and precipitates of NbC, TiC, VC and (Nb, Ti, V)C.

to TiN precipitation could be reasonably understood by the quantitative estimation based on the cutting mechanism.

The amount of precipitation hardening (ΔHv) of the tested samples can be estimated from Eqs. (4) and (7):

$$\Delta Hv = 0.69 \cdot kG|\varepsilon|^{1.5}\left(\frac{fr}{b}\right)^{0.5}, \tag{9}$$

The constant k in Eqs. (4) and (9) is reported to be approximately 1–3 [22, 23]. The precipitation hardening (ΔHv) by addition of 0.5 mass% Mo was quite small (**Figure 2**). Furthermore, Mo carbides were not detected by TEM observation in all the samples. From these reasons, the effect of Mo carbides on precipitation hardening can be excluded from the estimations. Therefore, carbides that mainly contribute to precipitation hardening in steels B, C, D and E are NbC, TiC, VC and (Nb, Ti, V)C, respectively.

Figure 6 shows the relationship between the measured ΔHv values and the parameter $G|\varepsilon|^{1.5}$ $(fr/b)^{0.5}$ of the present steels. Calculated results using Eq. (9) and constant k of 1 and 3 are also shown by dotted lines. For the calculation of $G|\varepsilon|^{1.5}$ (f r/b)$^{0.5}$, the diameter of carbides (2r) was assumed to be 5 nm for simplicity, and the volume fraction of the precipitates (f) was estimated by the "Thermo-Calc" calculation using the chemical compositions in **Table 1**. It is evident in **Figure 6** that the results derived from experimental data of steels D and E appear between the lines with constant k of 1 and 3. The above results indicate that the values of ΔHv calculated from Eq. (9) almost coincide with the present experimental data. That is, quantitative estimation of the amount of precipitation hardening (ΔHv) in the medium carbon bainitic steels with Nb, Ti and V additions can be reasonably understood by the carbide/matrix lattice misfit parameter and cutting
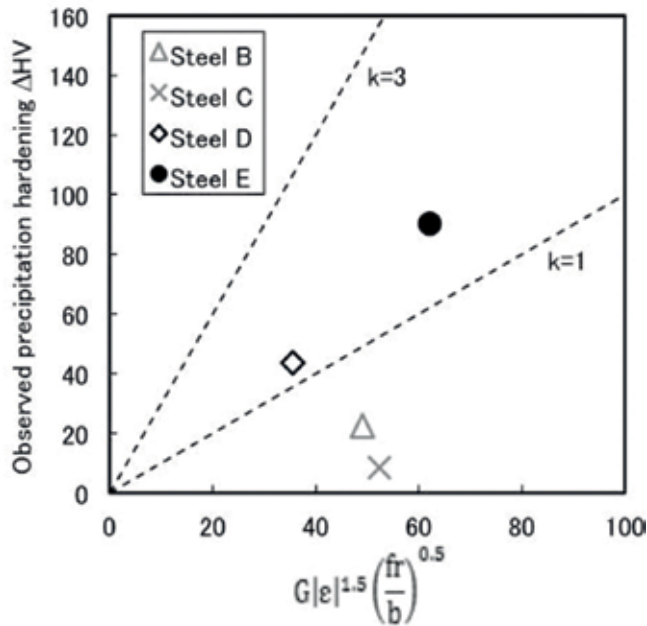
Figure 6. Relationship between the measured precipitation hardening (ΔHv) and estimated parameter $G|\varepsilon|^{1.5} (fr/b)^{0.5}$ using experimental data of the present steels, which are exhibited by symbols. For comparison, the relationship derived from Eq. (9) is also shown by dotted lines with k constants of 1 and 3.

mechanism for dislocation to pass through carbides. On the other hand, in steels B and C, the measured ΔHv values were far from the calculated data. This could be because of the misfit dislocations that were produced around the carbides to reduce the misfit strain between carbides and matrix, since the misfit parameter (ε) of NbC and TiC is very large. Hence, precipitation hardening in steels B and C would not be understood simply by the cutting mechanism only presumably because of the loss of coherency between the coarsen carbides and matrix. Reduction of ΔHv, therefore, took place because of a loss of coherency at the carbide/matrix interface [15]. Loss of coherency at the interface is well known to appear by coarsening [24, 25] and large lattice misfit strain [26]. Hence, complicated dislocation-bypass mechanisms could be activated depending on the size of precipitates in steels B and C.

5. Conclusions

The precipitation hardening due to complex carbides in medium carbon bainitic steels was investigated. The yielded results are as follows:

1. Small amount of additional elements can cause drastic change in the structures and chemical compositions of nanocarbides dispersed in steels, which induce conversion in dislocation bypass mechanisms to improve mechanical properties.

2. The amount of precipitation hardening in medium carbon bainitic steel with multiple element additions of Nb, Ti and V was larger than those in steels with single additions of these elements.

3. The dominant dislocation-bypass mechanism at room temperature of VC and (Nb, Ti, V)C carbides with a diameter approximately of 5–8 nm is the cutting mechanism, whereas that of NbC and TiC carbides appears different.

4. The difference in the amount of precipitation hardening could be reasonably understood by the lattice misfit parameter between carbide and matrix.

5. Cutting mechanism would not be dominant when the precipitate/matrix misfit parameter and size of carbides become large enough due to loss of coherency.

Acknowledgements

Author details

Makoto Okonogi[1], Takuya Hara[2] and Hiromi Miura[3]*

*Address all correspondence to: miura@me.tut.ac.jp

1 Kimitsu R&D Lab., Nippon Steel and Sumitomo Metal Corporation, Kimitsu, Chiba, Japan

2 Pipe and Tube Research Lab., Steel Research Laboratories, Nippon Steel and Sumitomo Metal Corporation, Amagasaki, Hyogo, Japan

3 Department of Mechanical Engineering, Toyohashi University of Technology, Toyohashi, Aichi, Japan

References

[1] Funakawa Y, Shiozaki T, Tomita K, Yamamoto T, Maeda E. Development of high strength hot-rolled sheet steel consisting of ferrite and nanometer-sized carbides. ISIJ International. 2004;**44**:1945-1951. DOI: https://doi.org/10.2355/isijinternational.44.1945

[2] Miyata K, Sawaragi Y. Effect of Mo and W on the phase stability of precipitates in low Cr heat resistant steels. ISIJ International. 2001;**41**:281-289. DOI: https://doi.org/10.2355/isijinternational.41.281

[3]   Miyata K, Omuma T, Kushida T, Komizo Y. Coarsening kinetics of multicomponent MC-type carbides in high-strength low-alloy steels. Metallurgical Materials Transactions A. 2003;**34**:1565-1573. DOI: https://doi.org/10.1007/s11661-003-0303-x

[4]   Murase Y, Iwase N, Takemoto Y, Senuma T. Precipitation hardening behavior of V and/or Cu bearing middle carbon steels. Tetsu-to-Hagane. 2013;**99**:669-675. DOI: https://doi.org/10.2355/tetsutohagane.99.669

[5]   Grange RA, Hribal CR, Porter LF. Hardness of tempered martensite in carbon and low-alloy steels. Metallurgical. Transactions A. 1977;**8**:1775-1785. DOI: https://doi.org/10.1007/BF02646882

[6]   Kosaka M, Yoshida S, Tarui T. Precipitation hardening behavior of alloy carbide (Precipitation hardening and hydrogen trapping behavior in high strength steels-1). CAMP-ISIJ. 2004;**17**:1370. DOI: https://y100.isij.or.jp/acceptance/Ronbunzi/record_detail.php?-recid=18181

[7]   Takada H. Alloy designing of high strength bainite steels for hot forging. Tetsu-to-Hagane. 2002;**88**:534-538. DOI: https://doi.org/10.2355/tetsutohagane1955.88.9_534

[8]   Baker G, Nutting J. London, Iron and Steel Institute, Special Report. 1959;**64**:1-22. DOI: https://trove.nla.gov.au/version/44983341

[9]   Orowan E. Symposium on Internal Stresses in Metals and Alloys, Session III Discussion, Effects Associated with Internal Stresses. Institute of Metals, London; 1948. pp. 451-453. OCLC No.:1814639

[10]   Gerold V, Haberkorn H. On the critical resolved shear stress of solid solutions containing coherent precipitates. Physica Status Solidi. 1966;**16**:675-684. DOI: https://doi.org/10.1002/pssb.19660160234

[11]   Takaki S. Strengthening of steel by secondary particles. In: Fundamentals and Applications of Precipitation in Steels. Tokyo: Iron and Steel Institute of Japan; 2001. pp. 69-80. ISBN: 10:4930980267

[12]   Nakashima K, Futamura Y, Tsuchiyama T, Takaki S. Interaction between dislocation and copper particles in Fe-Cu alloys. ISIJ International. 2002;**42**:1541-1545. DOI: https://doi.org/10.2355/isijinternational.42.1541

[13]   Takahashi J, Kawasaki K, Kawakami K, Sugiyama M. Three-dimensional atom probe analysis of nitriding steel containing Cr and Cu. Nippon Steel Technical Report. 2005;**91**:23-27. UDC 669.15'26'3-155.3:543.5

[14]   Nakashima K, Futamura Y, Tsuchiyama T, Takaki S. Precipitation strengthening at elevated temperature in Fe-Cu alloys. Tetsu-to-Hagane. 2003;**89**:524-529. DOI: https://doi.org/10.2355/tetsutohagane1955.89.5_524

[15]   Miura H, Tsukawaki H, Sakai T, Jonas JJ. Effect of particle/matrix interfacial character on the high-temperature deformation and recrystallization behavior of Cu with dispersed Fe particles. Acta Materialia. 2008;**56**:4944-4952. DOI: https://doi.org/10.1016/j.actamat.2008.06.012

[16] Yeomans SR, Mccormick PG. An investigation of precipitation and strengthening in age-hardening copper-manganese alloys. Materials Science Engineering. 1978;**34**:101-109. DOI: https://doi.org/10.1016/0025-5416(78)90040-X

[17] Takahashi J, Kawakami K, Kobayashi Y. Consideration of particle-strengthening mechanism of copper-precipitation-strengthened steels by atom probe tomography analysis. Materials Science. Engineering A. 2012;**535**:144-152. DOI: https://doi.org/10.1016/j.msea.2011.12.056

[18] Hamar-Thibault S, Adnane L, Kesri R. Miscibility of binary VC–MC carbides in quaternary Fe–V–M–C alloys. Journal of Alloys and Compounds. 2001;**317-318**:311-314. DOI: https://doi.org/10.1016/S0925-8388(00)01362-1

[19] Denton AR, Ashcroft NW. Vegard's law. Physical Review A. 1991;**43**:3161-3164. DOI: https://doi.org/10.1103/PhysRevA.43.3161

[20] Miyamoto G, Hori R, Poorganji B, Furuhara T. Interphase precipitation of VC and resultant hardening in V-added medium carbon steels. ISIJ International. 2011;**51**:1733-1739. DOI: https://doi.org/10.2355/isijinternational.51.1733

[21] Ronay M. Nitridable steels for cold forming processes. Metallurgical Transactions A. 1981;**12**:1951-1955. DOI: https://doi.org/10.1007/BF02643808

[22] Ibrahim IA, Ardell AJ. Hardening mechanisms in underaged ordered and disordered Cu_3Au-Co alloy single crystals. Acta Metallurgica. 1977;**25**:1231-1240. DOI: https://doi.org/10.1016/0001-6160(77)90212-7

[23] Ardell AJ. Precipitation hardening. Metallurgical Transactions A. 1985;**16**:2131-2165. DOI: https://doi.org/10.1007/BF02670416

[24] Gerold V, Pham HM. Precipitation hardening by misfitting particles and its comparison with experiments. Scripta Metallurgica. 1979;**13**:895-898. DOI: https://doi.org/10.1016/0036-9748(79)90182-0

[25] Pande CS, Imam MA. Nucleation and growth kinetics in high strength low carbon ferrous alloys. Materials Science. Engineering A. 2007;**457**:69-76. DOI: https://doi.org/10.1016/j.msea.2006.12.043

[26] Furuhara T. Structure and energy of interphase boundaries in steel. Tetsu-to-Hagane. 2003;**89**:497-509. DOI: https://doi.org/10.2355/tetsutohagane1955.89.5_497

Elaboration of Nanoporous Copper via Chemical Composition Design of Amorphous Precursor Alloys

Zhenhua Dan, Fengxiang Qin, Izumi Muto,
Nobuyoshi Hara and Hui Chang

Additional information is available at the end of the chapter

Abstract

Au-group (Ag, Au) and Pt-group (Ni, Pd, Pt) metals have lower surface diffusion coefficients than Cu and are defined as LSD. The chemical composition has been designed based on the differences in diffusion coefficients, and the micro-alloying of 1 at % LSD metals with the $Ti_{60}Cu_{40}$ amorphous precursor alloy results in the formation of bi-continuous nanoporous copper (NPC) with finer nanoporous structure. LSD-stabilized NPCs have the smallest characteristic pore sizes of 7 nm and 6 nm after dealloying amorphous $Ti_{60}Cu_{39}Pd_1$ and $Ti_{60}Cu_{39}Pt_1$ precursor alloys, while NPC had a pore size of 39 nm after dealloying the amorphous $Ti_{60}Cu_{40}$ alloy. The refining factor increases approximately from 3.7 for $Ti_{60}Cu_{39}Ag_1$ to 1780 for $Ti_{60}Cu_{39}Pt_1$ precursors due to the dramatic decrease in the surface diffusivity during both preferential dissolution and rearrangement of Cu adatoms. The elaboration efficiencies of $Ti_{60}Cu_{40}$ alloy with addition of 1 at.% Pt-group elements are higher than those of Au-group elements. The homogeneous distribution of LSD elements in both the precursors and final stabilized NPCs played a key role in restriction of the long-distance diffusion of Cu adatoms. LSD-stabilized NPCs are able to have an ultrafine nanoporosity with a pore size almost one order smaller than that from LSD-free alloys.

Keywords: amorphous precursor alloys, nanoporous copper, surface diffusion, micro-alloying, elaboration of nanoporous copper

1. Introduction

Nanoporous metals (NPMs), a representative type of nanostructured materials, possess intriguing properties to generate promising potentials for various important applications, including catalysis, sensors, actuators, fuel cells, micro-fluidic flow controllers, and

so forth [1–4]. NPMs with a variety of superior physical-chemical properties arisen from their unique pore structure, large specific surface area, and high electrical conductivity have attracted great interests to explore their electrocatalytic properties and greatly extend their potential applications in catalysts, electrochemical sensing, and energy systems [1]. Dealloying primarily originated from the phenomenon of selective corrosion has attracted more attention recently because it has been regarded to be an effective method to fabricate NPMs with a three-dimensional bi-continuous interpenetrating ligament-channel structure at the nanometer scale [5–8]. Nanoporous copper (NPC) is cost-effective and readily fabricated via dealloying process due to the high electrochemical stability. NPCs with different morphologies have been obtained from numerous binary alloy systems including Zn-Cu [7, 9], Mg-Cu [10], Al-Cu [7, 11–16], Ni-Cu [7], Mn-Cu [17, 18], Zr-Cu [19], and Ti-Cu [20].

The characteristic pore sizes of NPCs obtained from the systems mentioned above are relatively larger than those of nanoporous gold (NPG) or nanoporous platinum (NP Pt) and change from few tenth nanometers to few hundredth nanometers, particularly for Zr-Cu system with a pore size of 500 nm [19]. The pore sizes have a significant effect on the mechanical properties of NPMs. The smallest size of nanopores is of order of 3.5 nm for the Cu-Pt system [21]. The yield strength of nanometer-sized NPG ligaments has been improved from ~880 MPa to 4.6 GPa as the NPGs' pore size was refined from 50 nm to 10 nm [22]. As has been reported, the rough NPCs have a relative lower yield strength (i.e., 128 ± 37 MPa with a ligament size of 135 ± 31 nm [17], 86 ± 10 MPa as the ligaments with a size of 300–500 nm of NPCs fabricated by one-step dealloying of the melt-spun Al-50 at.% Cu alloy [11]). It is thus of importance to fabricate NPMs with finer nanostructure with smaller pore size and ligament scales. On the other hand, the elaboration of NPCs is helpful for the enhancements of the catalytic performance and sensitivity for various gaseous phases or metallic ions. Effective ways to reduce the characteristic nanopore sizes have been reported to be dealloying at low temperature [23]; chemical composition design of the precursor alloys, for example, Ag-Au-Pt [24], Al-Pt-Au [25], Ti-Cu-Au [26, 27], Ti-Cu-Ag [28], Ti-Cu-Ni [29], and Ti-Cu-Pd/Pt [30]; and modification of the solution chemistry by using organic acids [31] and by introducing the macromolecules of polyvinylpyrrolidone [32, 33]. The chemical composition design is considered to be an effective way to change the surface diffusion and rearrangements of the adatoms of the noble elements in the precursor alloys since these noble elements take effect from inside to outside. However, the uniform nanoporosity of NPCs is of importance for enhancing the mechanical properties and catalytic performances. Final nanoporous structure is affected by many factors, such as the chemical compositions and initial microstructure of the precursor alloys, the solution chemistries of dealloying solutions, and the experimental conditions (i.e., temperatures, etc.) [12, 34, 35]. The crystalline precursor alloys are extensively dealloyed to prepare NPMs (i.e., coarsen crystalline Al-Cu alloys [11], nanocrystalline Ag-Au, Ag-Au-Pt alloys [22, 24]). While the intermetallic phases or secondary phases exist in the matrix, the final nanoporous structures inherit the characteristics of their initial microstructure of precursor alloys. The characteristics of the casting structures, the intermetallics, and the phase segregations

typical of the crystalline alloys, such as Al-Cu [11–16], Zn-Cu [9], Mg-Cu [10], Mn-Cu [17], Zr-Cu [19], and Ti-Cu [12, 13] alloys are inherited by the final porous structures. The kind and the chemical composition of the initial intermetallic phases and microstructure usually cause the formation of multi-modal nanoporous structures [9–17, 19]. On the contrary, the amorphous alloys exhibit many advantages, especially in their uniform distribution of the alloy constituents without the segregation in the chemical composition and heterogeneity in the microstructure [36]. It is believed that the absence of grain boundary, the large-scaled phase segregations, and intermetallics of amorphous precursors contributes to high uniformity in NPMs. Amorphous alloys with disordered atomic-scale structure, an absence of the weak sites (i.e., grain/phase boundaries typical of crystalline materials) [37], are good to be precursor alloys for the fabrication of the uniform NPMs in some extent. The formation of highly uniform and ultrafine nanoporous structures has been realized for several amorphous alloy systems, including Mg-Cu-Y [31], Ti-Cu-Au [26, 27], Ti-Cu-Ag [28], and Ti-Cu-Ni [29] ternary alloys.

2. Materials and methods

On the basis of binary $Ti_{60}Cu_{40}$ alloy, ternary alloys with nominal compositions of $Ti_{60}Cu_{39}M_1$ (M: Ni, Pd, Pt, Ag, Au) were designed and prepared by arc melting of high purity (purity > 99.99 mass%) of raw metals. The LSD elements were divided into two groups: G-I Au-group (Ag, Au) and G-II Pt-group (Ni, Pd, Pt). The surface diffusion coefficients have been reported to be 1.1×10^{-24} m s^{-2} for Pd and 3.6×10^{-26} m s^{-2} for Pt and 2.2×10^{-23} m s^{-2} for Au [38]. The surface diffusion coefficient of Ag in a vacuum is two orders lower than that of Cu as reported [12, 39, 40]. That of Cu is 1.1×10^{-18} m s^{-2}, more than two orders higher than LSD elements. The surface diffusivity of Ni adatoms in the electrolyte was one tenth of that of Cu adatoms [41]. The ribbon samples were fabricated by melt spinning with a dimension of 20 μm in thickness and 2 mm in width. The starting $Ti_{60}Cu_{39}M_1$ amorphous precursor alloys were treated under the free immersion condition for 43.2 ks in 0.03 M HF solution at 298 K. The detailed information of the experimental procedures has been supplied in the previous publications [27–30]. An X-ray diffractometer (XRD, Rigaku 4200) was employed to identify the change in the lattice constants, crystalline states of dealloyed alloys and microstructure of precursor alloys and dealloyed alloys. The porous morphologies of the nanoporous NPC and LSD-stabilized samples were observed by a scanning electron microscope (JEOL, JIB-4610F). The chemical composition of the as-dealloyed samples was analyzed by an energy dispersive X-ray spectroscope (JEOL, JIB-4610F). Transmission electron microscopes (JEOL, HC2100, and ARM200) were used to observe the internal porous structure, the nanoporosity of dealloyed alloys, and crystalline characteristics of the LSD-stabilized Cu ligaments in high-resolution TEM modes. The nanoporosity was mainly analyzed on the basis of the average size of the nanopores and ligaments. The characteristic pore size of as-dealloyed alloys was confirmed by the single chord method for over 125 sites on SEM and TEM images.

3. Elaboration of nanoporous copper via the chemical composition design

3.1. Characteristics of LSD-added Ti-Cu precursor alloys and nanoporous counterparts

The XRD patterns of the as-spun $Ti_{60}Cu_{40}$, $Ti_{60}Cu_{39}Ni_1$, $Ti_{60}Cu_{39}Pd_1$, and $Ti_{60}Cu_{39}Pt_1$ ribbons present one strong and broad diffraction peak at 41° and a weak diffraction peak at 70–75°, indicating an amorphous structure, as shown in **Figure 1**. Other LSD-substituted $Ti_{60}Cu_{40}$ precursor alloys were still amorphous states, indicating that the micro-alloying of 1 at.% LSD elements had not generated the heterogeneous microstructure or phase segregation. The high-resolution TEM images (HRTEM) and corresponding selective area diffraction patterns (SADP) of as-spun $Ti_{60}Cu_{40}$ and $Ti_{60}Cu_{39}M_1$ show that as-spun LSD-substituted $Ti_{60}Cu_{39}M_1$ alloys had an amorphous structure without the crystalline clusters and phase segregations [27]. As is well known, because G-I LSD elements, Ag and Au, have a similar crystal structure to Cu, the addition of minor amounts of G-I elements has thus no significant influence on the structure of as-spun alloys [26, 27]. In G-II elements, Ni, Pd, and Pt, three strong diffraction peaks were observed in the XRD patterns of the dealloyed $Ti_{60}Cu_{39}Pd_1$ and $Ti_{60}Cu_{39}Pt_1$ ribbons after dealloying for 43.2 ks in the 0.03 M HF solution. The diffraction peaks were identified to be *fcc* Cu and had slightly shifted to low diffraction angles due to the expansion of the LSD-substituted

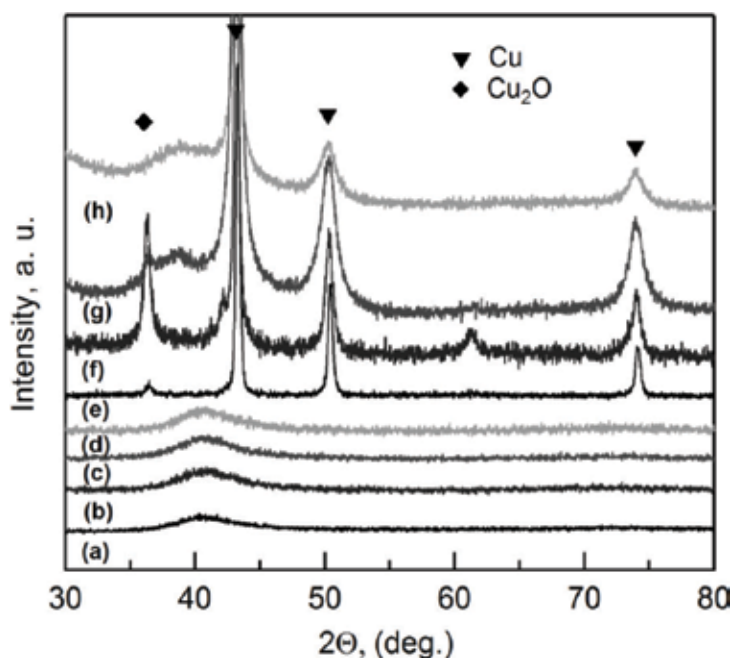**Figure 1.** XRD patterns of as-spun (a, b, c, d) and dealloyed (e, f, g, h) $Ti_{60}Cu_{40}$ (a, e), $Ti_{60}Cu_{39}Ni_1$ (b, f), $Ti_{60}Cu_{39}Pd_1$ (c, g), and $Ti_{60}Cu_{39}Pt_1$ (d, h) ribbons after immersion in 0.03 M HF solution for 43.2 ks. Reproduced with permission from Dan et al. [30] Copyright Materials Transactions.

unit cells. The small peak around 36° was considered to be from the Cu_2O phase. The absence of strong diffraction peaks from crystalline Pd and Pt phases indicates that CuPd or CuPt solid solution formed after dealloying. These XRD patterns were similar to those of Ag-, Au-, and Ni-stabilized NPCs [26–29]. **Figure 2** shows the change in the lattice constant, α, and the grain sizes, L, with 1 at% addition of Au-group (G-I) and Pt-group (G-II). The standard lattice constants are reported to be 0.3524 nm for Ni, 0.3608 nm for Cu, 0.3891 nm for Pd, 0.3924 nm for Pt, 0.4078 nm for Au, and 0.4085 nm for Ag, respectively. The lattice constants of NPCs were estimated to be 0.3615–0.3627 nm on the basis of the XRD data of Cu (111) peaks. The lattice constants became larger when the added elements had larger lattice constants except in the case of Ag. As indicated in **Figure 2**, the Cu lattice expanded more when Pd and Pt were micro-alloyed into the $Ti_{60}Cu_{40}$ alloy. The added Ni, Pd, or Pt atoms were thus considered to substitute the Cu atoms in the Cu lattice to a higher extent than in the Ag- or Au-added cases, resulting in the expansion of the Cu lattice constants from 0.3615 nm to 0.3627 nm in **Figure 2**. In previous works it was found that the Au or Ag phase was formed after dealloying the $Ti_{60}Cu_{39}Au_1$ and $Ti_{60}Cu_{39}Au_1$ precursor alloys [26–29]. The absence of diffraction peaks from the Pd or Pt phase in the XRD patterns of dealloyed $Ti_{60}Cu_{39}Pd_1$ and $Ti_{60}Cu_{39}Pt_1$ ribbons and the large expansion of the lattice constants of the NPCs indicated that more Pt-group atoms invaded the Cu lattice than Au-group atoms (i.e., Ag addition and Au addition) for NPCs from precursor alloys micro-alloyed with LSD elements [26–29]. On the other hand, the grain sizes were reduced to 15 nm and 13 nm when the Pd and Pt were added into $Ti_{60}Cu_{40}$ ribbons.

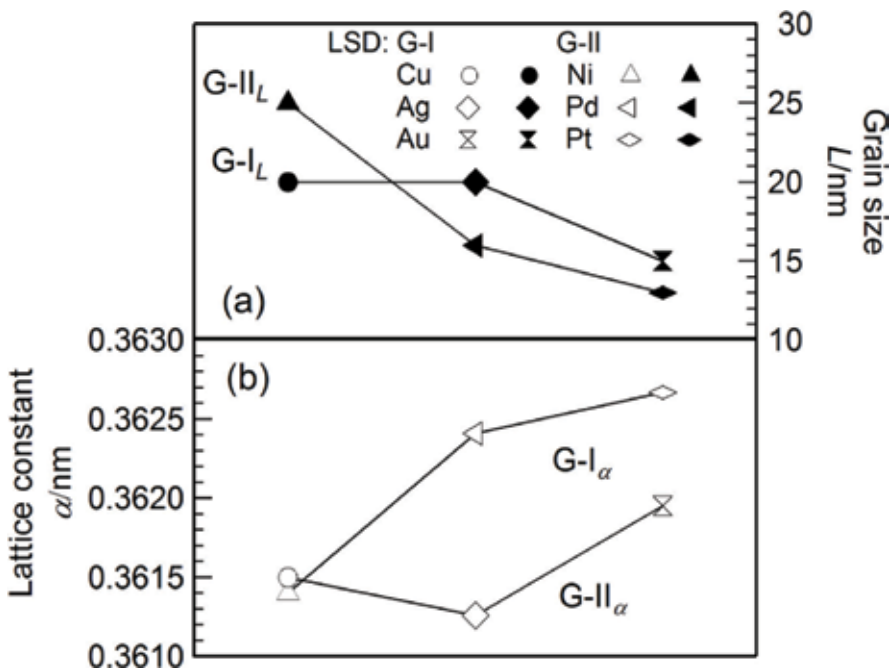**Figure 2.** Dependence of the grain sizes (a) and the lattice constants (b) of dealloyed $Ti_{60}Cu_{39}M_1$ (M: LSD—G-I Cu, Ag, and Au and G-II Ni, Pd, and Pt) ribbons on the addition of the elements. The lines are used for view guide of data points in G-I and G-II. Reproduced with permission from Dan et al. [30] Copyright Materials Transactions.

The decrease in the grain sizes was considered to be due to the retardation of the self-diffusion of Cu adatoms by LSD elements [27, 29, 30]. The diffusion distance of Cu adatoms under free diffusion patterns is prevailed in a long-distance diffusion mode [2, 5, 10, 19–21]. However, the long-distance self-diffusion of Cu adatoms was interrupted and restricted by the LSD adatoms during the rearrangement of adatoms and resulted in an accumulation of Cu and LSD adatoms in a smaller scale. Consequently, smaller grains were formed when the Pt-group elements (Pd, Pt) and Au element were used to stabilize NPCs.

The nanoporous surface morphologies of dealloyed $Ti_{60}Cu_{39}M_1$ (M: Cu, Ag, Au, Ni, Pd, Pt) alloys are shown in **Figure 3**. The mean pore size of the nanoporous structure of as-dealloyed $Ti_{60}Cu_{40}$ ribbons was about 71 nm after dealloying in 0.03 M HF solution. The characteristic length scales of ligaments of NPC obtained from $Ti_{60}Cu_{40}$ alloy were 74 nm in 0.03 M HF solution. The characteristic sizes for the nanopores and ligaments were confirmed to be for 41 and 48 nm for dealloyed $Ti_{60}Cu_{39}Ag_1$ precursor, 16 nm and 27 nm for $Ti_{60}Cu_{39}Au_1$ precursor, 12 nm and 26 nm for $Ti_{60}Cu_{39}Ni_1$ precursor, 9 nm and 24 nm for $Ti_{60}Cu_{39}Pd_1$ precursor, and 8.5 nm and 31 nm for $Ti_{60}Cu_{39}Pt_1$ precursor. **Figure 4** shows a typical bright field TEM image (BFI), their corresponding selected area diffraction pattern (SADP) of $Ti_{60}Cu_{39}M_1$ (M: Cu, Ag, Au, Ni, Pd, Pt) amorphous alloys after dealloying for 43.2 ks. A bi-continuous porous microstructure was formed with a characteristic pore size of 7 nm for the dealloyed $Ti_{60}Cu_{39}Pd_1$ ribbon and ca. 6 nm for the dealloyed $Ti_{60}Cu_{39}Pt_1$ ribbon, respectively (**Figure 4e** and **3f**). The diffraction rings in the SAD patterns were assigned to Cu (111), (200), (220), and (311) (JCPDS
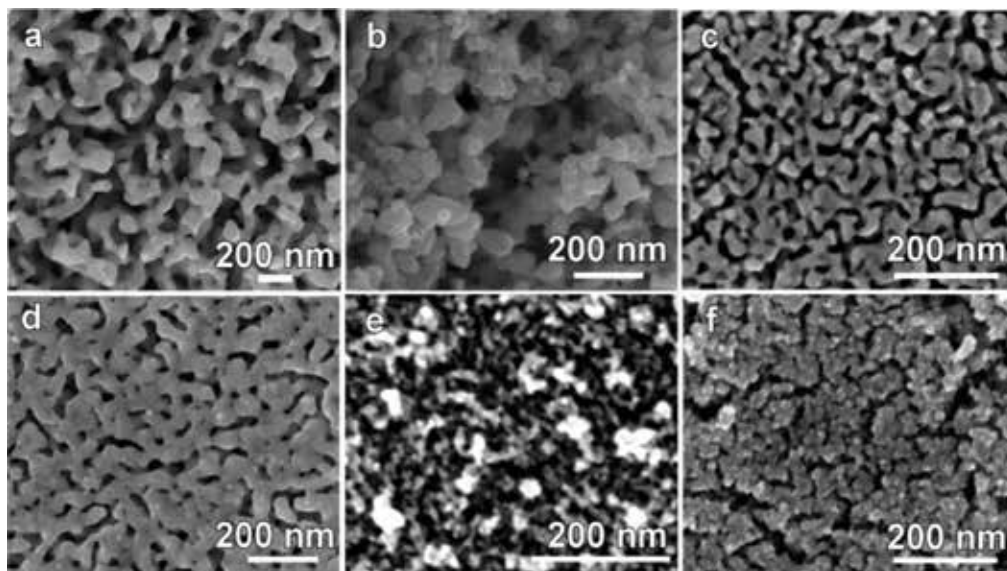
Figure 3. Typical surface morphologies of dealloyed $Ti_{60}Cu_{40}$ (a), $Ti_{60}Cu_{39}Ag_1$ (b), $Ti_{60}Cu_{39}Au_1$ (c), $Ti_{60}Cu_{39}Ni_1$ (d), $Ti_{60}Cu_{39}Pd_1$ (e), and $Ti_{60}Cu_{39}Pt_1$ (f) precursors after dealloying in 0.03 M HF solution for 43.2 ks. Reproduced with permission from Dan et al. [30] Copyright Materials Transactions. Reproduced with permission from Dan et al. [27, 30] copyright Elsevier and Materials Transactions.
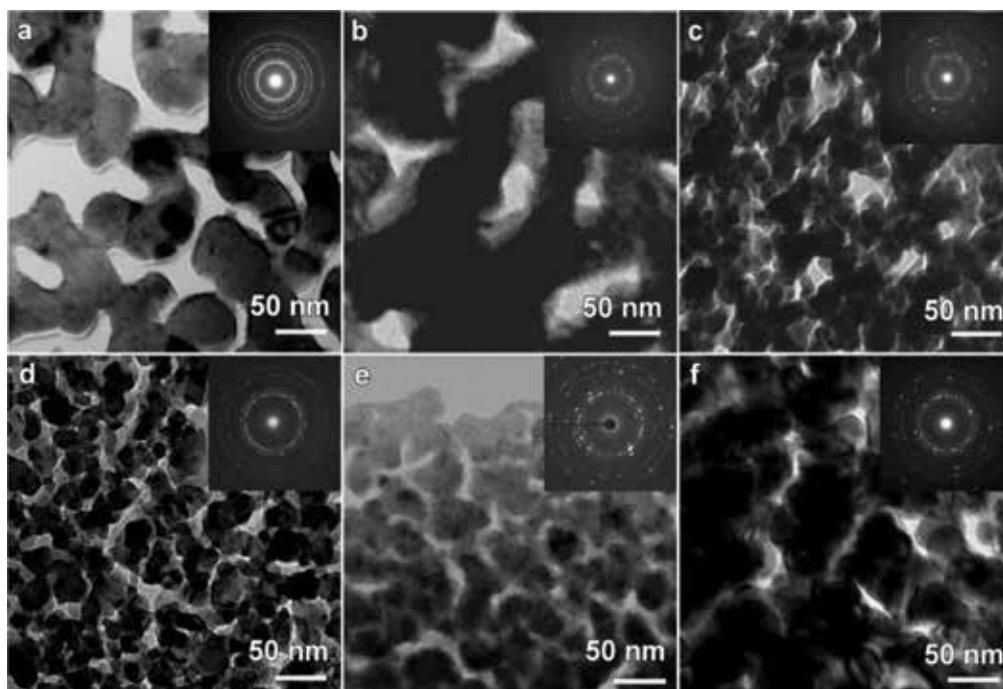
Figure 4. Typical bright field TEM images of dealloyed $Ti_{60}Cu_{40}$ (a), $Ti_{60}Cu_{39}Ag_1$ (b), $Ti_{60}Cu_{39}Au_1$ (c), $Ti_{60}Cu_{39}Ni_1$ (d),$Ti_{60}Cu_{39}Pd_1$ (e), and $Ti_{60}Cu_{39}Pt_1$ (f) precursors after dealloying in 0.03 M HF solution for 43.2 ks. The insets are their corresponding selected area diffraction patterns. Reproduced with permission from Dan et al. [30] Copyright Materials Transactions.

card No. 02-1225), and the inner ring was done for Cu_2O (111) (JCPDS card No. 74-1230). The diffraction rings from the Cu_2O phase were absent in the inset SADP in **Figure 4e**. The ligament sizes were confirmed to be ca. 23 nm for the dealloyed $Ti_{60}Cu_{39}Pd_1$ ribbon and ca. 30 nm for the dealloyed $Ti_{60}Cu_{39}Pt_1$ ribbon. The BFI images mainly reflected the internal nanoporous structures with a finer porosity in comparison to those in the surface regions. It is considered that the finer nanoporous structure in the internal parts mainly resulted from the lower concentration gradients inside the channels. As shown in **Figure 4e** and **f**, the pore size of Pd-stabilized and Pt-stabilized NPCs had a mean pore size of 7 and 6 nm, respectively. As shown in **Figure 4b–d**, the characteristic pore size of NPCs stabilized by the micro-alloying of Ni, Ag, and Au [27–29] has been reported to be 11 nm, 28 nm, and 12 nm on the basis of TEM analysis, respectively. The mean pore size of dealloyed $Ti_{60}Cu_{40}$ ribbons confirmed by TEM observation was 39 nm in **Figure 4a** [20]. The pore size decreased more than one order due to the addition of either Pd or Pt as shown in **Figure 4e** and **f**. The characteristic scale length of the nanopores and ligaments of dealloyed $Ti_{60}Cu_{39}Pd_1$ and $Ti_{60}Cu_{39}Pt_1$ ribbons decreased dramatically. On the basis of XRD, TEM, and SEM-EDX analysis, the residue is considered to be *fcc* CuPd and *fcc* CuPt solid solution. The similarity existed in all LSD-substituted $Ti_{60}Cu_{39}M_1$ (M: Ag, Au, Ni, Pd, Pt). Commonly the Cu(LSD) solid solutions can be regarded as the residual phases after dealloying. However, the selective dissolution is slightly different which caused

the formation of Ag and Au phases [27, 28]. Although NPCs from $Ti_{60}Cu_{39}Ag_1$ precursor had a large final nanopore, the elaborating behavior still happened at the initial dealloying stages with a high refining efficiency [28]. As shown in **Figure 5**, the distribution of Au LSD element was profiled. The uniform distribution of Au elements can be confirmed here. For other precursor alloys, the residual LSD elements had similar profiles which benefited from the uniform distribution of these LSDs in the amorphous precursor alloys.

3.2. Effects of LSDs on surface diffusion

On the basis of the surface diffusion-controlled coarsening mechanism, the surface diffusivity, D_s, at various dealloying temperatures was estimated by the equation [42]:

$$D_s = \frac{[d(t)]^4 kT}{32\gamma t a^4} \tag{1}$$

where k is Boltzmann constant (1.3806×10^{-23} J K^{-1}), γ is surface energy, t is the dealloying time (43,200 s), $d(t)$ is the pore size at t, T is the temperature, and α is the lattice constant. The pore size of NPCs confirmed by TEM micrographs and lattice constants calculated from XRD data were adopted for calculation of D_s. The surface energy of Cu has been reported to be 1.79 J m^{-2} [40, 43]. The surface energy of micro-alloyed elements has been reported to be 1.24 J m^{-2} for Ag, 1.50 J m^{-2} for Au, 2.0 J m^{-2} for Ni, 2.0 J m^{-2} for Pd, and 2.49 J m^{-2} for Pt [40, 43]. The concentration of Au-group elements (Ag, Au) and Pt-group elements (Ni, Pd, Pt) in the precursor alloys was 1 at%. The concentration of added elements (Ag, Au, Ni, Pd, Pt) in NPCs after dealloying should theoretically be 2.5 at% if the dissolution of Cu in HF solution is not considered. Therefore, the surface energy of LSD-stabilized NPCs is considered to be very close to that of Cu. The surface energy of Cu, 1.79 J m^{-2}, was adopted for the calculation of D_s. The characteristic nanopore sizes were summarized in **Figure 6a**, which has been illustrated above. On the other hand, the surface diffusivities of these LSD-stabilized alloys in 0.03 M HF solutions

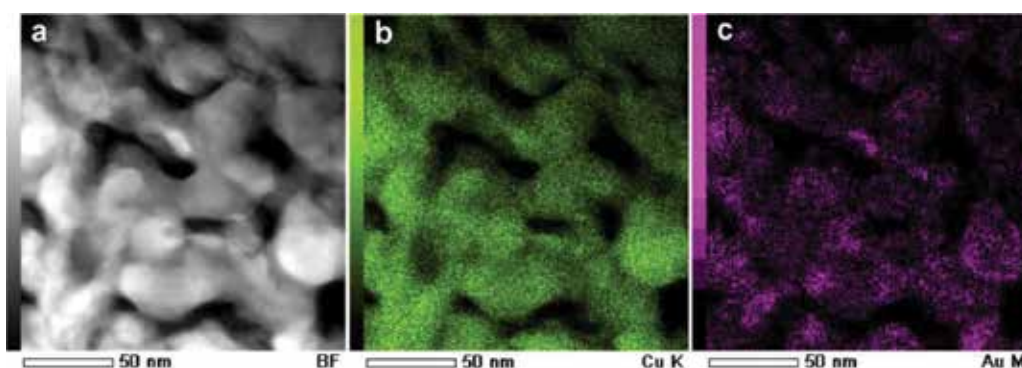**Figure 5.** High-angle annular dark field scanning TEM image (a) and elemental mapping of Cu (b) and Au (c) of dealloyed $Ti_{60}Cu_{39}Au_1$ precursors after dealloying in 0.03 M HF solution for 43.2 ks. Reproduced with permission from Dan et al. [27] Copyright Elsevier.
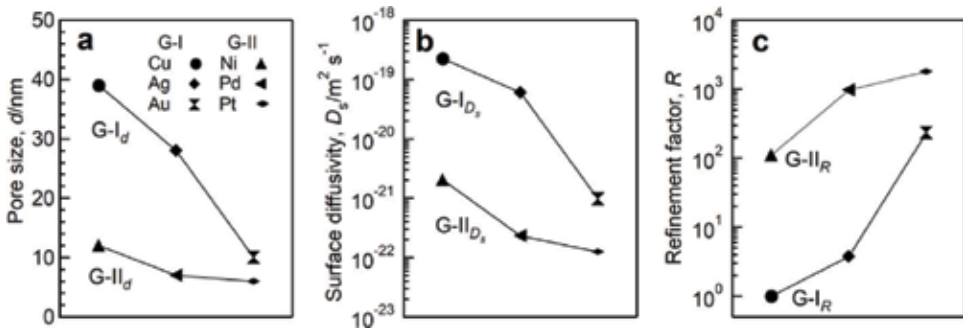
Figure 6. Mean pore size (a), surface diffusivity (b), and refining factor of dealloyed $Ti_{60}Cu_{39}M_1$. M is the selected LSD elements including Ag, Au, Ni, Pd, and Pt. The lines are used for view guide of data points in G-I and G-II. Reproduced with permission from Dan et al. [30] Copyright Materials Transactions.

can be modified. As shown in **Figure 5b**, the value of D_s was estimated to be 2.5×10^{-18} m² s⁻¹ for $Ti_{60}Cu_{40}$ ribbon, 6.0×10^{-20} m² s⁻¹ for $Ti_{60}Cu_{40}$ ribbon, 9.7×10^{-21} m² s⁻¹ for $Ti_{60}Cu_{39}Au_1$ ribbon and 2.0×10^{-21} m² s⁻¹ for $Ti_{60}Cu_{39}Ni_1$ ribbon, 2.3×10^{-22} m² s⁻¹ for $Ti_{60}Cu_{39}Pd_1$ ribbon, and 1.3×10^{-22} m² s⁻¹ for $Ti_{60}Cu_{39}Pt_1$ ribbon, respectively. The surface diffusivity decreased more than four orders of magnitude due to the addition of Pd and Pt. Compared with D_s of the Au-group-stabilized NPCs, the decrease in D_s in the Pt-group-stabilized NPCs was remarkable.

The refining factor, R, is defined as the ratio between the surface diffusivity, D_s, of NPC obtained from amorphous $Ti_{60}Cu_{40}$ precursor (numerator) and NPCs stabilized by LSDs (denominator):

$$R = \frac{D_s^{Cu}}{D_s^L} \approx \frac{[d(t)^{Cu}]^4}{[d(t)^L]^4} \times \frac{[a^{Cu}]^4}{[a^L]^4} \tag{2}$$

As shown in **Figure 6c**, the estimated refining factor was 968 for $Ti_{60}Cu_{39}Pd_1$ ribbon and 1780 for $Ti_{60}Cu_{39}Pt_1$ ribbon, respectively. In other cases, the value of R changed from 4 for the dealloyed $Ti_{60}Cu_{39}Ag_1$ ribbon, 111 for the dealloyed $Ti_{60}Cu_{39}Ni_1$ ribbon, and 231 for the dealloyed $Ti_{60}Cu_{39}Au_1$ ribbon, respectively. The refining efficiency of the micro-alloying of the Pt-group elements into the precursor $Ti_{60}Cu_{40}$ alloy was one order higher than that of the Au-group cases. The lower value of R for $Ti_{60}Cu_{40}$ alloy stabilized by Au-group (G-I) elements could take into account from several aspects: (1) the larger self-diffusion coefficients of Ag and Au than that of Cu [44–48] and (2) the large misfit in the atomic radii [49]. As has been reported before [44–48], the self-diffusion coefficients of Au- and Pt-group elements are ranked as following: Ag > Cu > Au > Ni > Pd > Pt. As such, there are more possibilities for Ag adatoms to meet with other Ag adatoms during the diffusion and rearrangements processes of dealloying to form clusters and to develop the Ag phase because it has a larger self-diffusion coefficient than Cu atoms [44, 48]. The self-diffusion coefficient of Au is slightly smaller than that of Cu [45]. Because the misfit in the atomic radius between Cu and Ag and Cu and Au is about 13%, the incorporation of Ag-Au atoms into the Cu lattice becomes more difficult than that of Cu/Cu atoms. On the other hand, the self-diffusion coefficients of Pt-group (G-II)

elements are more than two orders lower than that of Cu element [47, 48], and the formation of the crystalline phase of G-II elements (Ni, Pd, Pt) was interrupted by the fast diffusion of Cu adatoms. Furthermore, the misfits in the atomic radius between Cu and Pd and Pt elements are ca. 8%, and the incorporation of Pd/Pt into the Cu lattices appears more easily. The changes in the lattice constants of the NPCs stabilized by G-I and G-II indicated by XRD patterns in **Figure 1** and Refs. [27, 28] support the present hypothesis. As has presented above, the formation of the Ag and Au crystalline phases after dealloying is considered to be due to the difference in self-diffusion behaviors and misfits of the atomic radius. The minor addition of Group-I LSDs causes the formation of the crystalline Ag/Au phases, and the refining factors of Group I were small. On the other hand, the micro-alloying by Group-II LSDs mainly resulted in the invasion of the Cu lattices, with some Cu atoms in the lattice substituted by Ni, Pd, and Pt atoms, forming solid solutions, and the refining factors for Group II were high. In some extent, these LSD atoms in the lattice are considered to be the main contributors for the elaboration of NPCs.

The diffusion in the interfacial regions between Cu, LSD adatoms, and Ti adatoms played a key role in the formation of ultrafine NPCs. For example, Evangelakis investigated the diffusion of Au adatoms on Cu and self-diffusion of Cu adatoms by using the molecular dynamic method [50]. They have found that diffusion of Cu adatoms takes place exclusively by hopping from one adatom position to an adjacent one and that multiple jumps are frequent at low temperatures. On the other hand, Au adatoms on the NPC ligaments hopped less frequently than in the case of Cu self-diffusion. The migration energy required for hopping of Au on Cu was almost twice that of the corresponding energy for Cu adatoms. While the diffusion of Au on Cu was more difficult than the diffusion of Cu on Cu, this phenomenon is compatible with the binding energy of Au adatoms, which is found to be 2.77 eV for Au adatoms and 2.26 eV for Cu adatoms. The Au adatoms relaxed at a distance −15% smaller than the bulk interlayer distance, but in the case of the Cu adatoms, it was −10% for the same quantity [50]. The Cu adatoms diffused quickly in and out by themselves; however, the Au adatoms at the activated sites diffused out slowly and hardly ever diffused back to the NPC ligaments. Consequently, Au adatoms gradually accumulated outside the ligaments during the dealloying [27, 30]. As a result, Au adatoms uniformly distributed outside the ligaments after dealloying for 43.2 ks via the hopping mechanism, as shown in **Figure 5**. When more Au was added to TiCu amorphous alloys, the surface coverage of Au adatoms increased during dealloying, suggesting that the accumulation rate of Au adatoms in the more concentrated solutions was higher due to the faster migration of Au and Cu adatoms [27]. Because the accumulated Au adatoms built up a continuous outmost diffusion barrier, the behaviors of diffusion and rearrangements of Cu and Au adatoms can be fulfilled to form ultrafine NPCs from both the LSD-substituted $Ti_{60}Cu_{40}$ amorphous precursor alloys in HF solutions. The diffusion behavior for other LSD-stabilized nanoporous structures was considered to be similar. However, the accumulation of G-II Pt-group elements (Ni, Pd, and Pt) with much slower diffusion rates and Ni, Pd, and Pt cluster or grains with much smaller size less than 7 nm tended to form, which are not sensitive to X-ray [51]. As has been reported [52], a bimodal nanoporous structure with a pore size of 10 nm and 20 nm has been fabricated from $Al_{75}Pd_{17.5}Au_{7.5}$ precursor alloys by successive dealloying. The initial heterogeneous microstructure consisting of Al_2Au- and Al_3Pd-type intermetallics causes the formation of a bimodal nanoporous structure. The similar evolution of bimodal or multimodal nanoporosity on precursor alloys heterogeneous in microstructure

has been reported [11, 12, 14, 20, 41]. Amorphous precursor alloys with homogeneously distributed Cu, Ti, and LSD atoms also have an important refining effect. The uniform distribution of added Pd and Pt atoms in final NPCs resulted in smaller nanopores, as shown in **Figures 3** and **4**. In 2008, fine nanoporous AuPt alloys with a pore size of about 5 nm were fabricated from an $Ag_{65}Au_{29}Pt_6$ precursor [24]. The alloying of 6 at% Pt into the $Ag_{65}Au_{35}$ alloy effectively reduced the pore size from 10 to 20 nm to about 4 nm, which also supports the present results. However, the high cost of Au and Pt weakens their potential application. By minor addition of the 1 at% Pt-group elements, it is possible to elaborate NPCs down to a pore size of approximately 6 nm, comparable to high-cost AuPt nanoporous in nanoporosity. So far the LSD-stabilized NPCs had a relative small nanopores and narrow ligaments comparable to these of NP Au, NP Pd, and NP Pt. If catalytic Au, Pd, or Pt monolayer is electrodeposited on ultrafine NPCs, the catalytic performance of this kind of cost-effective porous materials is able to be close to those Au, Pd, or Pt catalysts. Meanwhile, if the oxides are assembled on ultrafine NPC templates, the new-developed nanocomposites can be used as promising pseudocapacitors to contribute in the energy conversion fields.

4. Conclusions

The 1 at% minor addition of low surface diffusive (LSD) elements in two groups (G-I, Au-group (Ag, Au), and G-II, Pt-group (Ni, Pd, Pt)) is able to elaborate the nanoporous Cu structure dealloyed from micro-alloyed $Ti_{60}Cu_{40}$ alloy efficiently. The chemical compositions of $Ti_{60}Cu_{40}$ alloys stabilized by the addition of G-II metals were shown to be more effective in refining nanoporous structure than the addition of G-I metals. Nanoporous Cu with a pore size of less than 7 nm was obtained from $Ti_{60}Cu_{39}Pd_1$ and $Ti_{60}Cu_{39}Pt_1$ ribbons after dealloying. The residue of dealloyed $Ti_{60}Cu_{39}Pd_1$ and $Ti_{60}Cu_{39}Pt_1$ ribbons was confirmed to be bimetallic solid solutions, such as fcc Cu(Pd) or Cu(Pt) solid solutions, and fcc Cu(Au), Cu(Ag), and Cu(Ni) solid solutions formed after dealloying. The refining factor increases approximately from 3.7 for the $Ti_{60}Cu_{39}Ag_1$ precursor alloy to 1780 for the $Ti_{60}Cu_{39}Pt_1$ precursor alloy. The elaboration was attributed to the dramatic decrease in the surface diffusivity during both preferential dissolution and rearrangement of Cu adatoms. The refinement efficiency of the micro-alloying of the G-II LSDs in Pt-group elements was almost one order higher than that of the G-I LSDs in Au-group elements. The homogeneous distribution of LSD elements in both of the amorphous precursor alloys and the final stabilized NPCs played a key role in refining the NPCs. The strategy outlined in this work has the potential to be applied to other alloy systems to obtain other ultrafine nanoporous metals with comparable nanoporosity to those high-cost catalysts.

Acknowledgements

Conflict of interest

The authors declare no conflict of interest.

Author details

Zhenhua Dan[1,2]*, Fengxiang Qin[3], Izumi Muto[2], Nobuyoshi Hara[2] and Hui Chang[1]

*Address all correspondence to: zhenhuadan@njtech.edu.cn

1 Tech Institute for Advanced Materials and College of Materials Science and Engineering, Nanjing Tech University, Nanjing, China

2 Department of Materials Science, Tohoku University, Sendai, Japan

3 School of Materials Science and Engineering, Nanjing University of Science and Technology, Nanjing, China

References

[1] Zhang JT, Li CM. Nanoporous metals: Fabrication strategies and advanced electrochemical applications in catalysis, sensing and energy systems. Chemical Society Review. 2012;**41**:7016-7031. DOI: 10.1039/C2CS35210A

[2] You TY, Niwa O, Tomita M, Hirono S. Characterization of platinum nanoparticle-embedded carbon film electrode and its detection of hydrogen peroxide. Analytical Chemistry. 2003;**75**:2080-2085. DOI: 10.1021/ac026337w

[3] Weissmueller J, Viswanath RN, Kramer D, Zimmer P, Wuerschum R, Gleiter H. Charge-induced reversible strain in a metal. Science. 2003;**300**:312-315. DOI: 10.1126/science.1081024

[4] Joo SH, Choi SJ, Oh I, Kwak J, Liu Z, Terasaki O, Rvoo R. Ordered nanoporous arrays of carbon supporting high dispersions of platinum nanoparticles. Nature. 2001;**412**:169-172. DOI: 10.1038/35084046

[5] Forty AJ. Corrosion micromorphology of noble metal alloys and depletion gliding. Nature. 1979;**282**:597-598. DOI: 10.1038/282597a0

[6]   Dursun A, Pugh DV, Corcoran SG. Dealloying of ag-au in halide-containing electro-lytes: Affect on critical potential and pore size. Journal of The Electrochemical Society. 2003;**150**:B355-B360. DOI: 10.1149/1.1580824

[7]   Pryor MJ, Fister JC. The mechanism of dealloying of copper solid solutions and inter-metallics phases. Journal of the Electrochemical Society. 1984;**131**:1230-1235. DOI: 10. 1149/1.2115793

[8]   Liu HT, He P, Li ZY, Li JH. High surface area nanoporous platinum: Facile fabrica-tion and electrocatalytic activity. Nanotechnology. 2006;**17**:2167-2173. DOI: 10.1088/ 0957-4484/17/9/015/meta

[9]   Pickering HW. Formation of new phase during anodic dissolution of Zn-rich cu-Zn alloys. Journal of the Electrochemical Society. 1970;**117**:8-15. DOI: 10.1149/1.2407450

[10] Zhao CC, Qi Z, Wang XG, Zhang ZH. Fabrication and characterization of monolithic nanoporous copper through chemical dealloying of Mg-Cu alloys. Corrosion Science. 2009;**51**:2120-2125. DOI: 10.1016/j.corsci.2009.05.043

[11] Qi Z, Zhao CC, Wang XG, Lin JK, Shao W, Zhang ZH, Bian XF. Formation and charac-terization of monolithic nanoporous copper by chemical dealloying of Al-Cu alloys. The Journal of Physical Chemistry C. 2009;**113**:6694-6698. DOI: 10.1021/jp810742z

[12] Zhang ZH, Wang Y, Qi Z, Zhang WH, Qin JY, Frenzel J. Generalized fabrication of nano-porous metals (Au, Pd, Pt, Ag and Cu) through chemical dealloying. Journal of Physical Chemistry C. 2009;**113**:12629-12636. DOI: 10.1021/jp811445a

[13] Liu WB, Zhang SC, Li N, Zheng JW, Xing YL. A facile one-pot route to fabricate nanopo-rous copper with controlled hierarchical pore size distributions through chemical deal-loying of Al-Cu alloy in an alkaline solution. Microporous and Mesoporous Materials. 2011;**138**:1-7. DOI: 10.1016/j.micromeso.2010.10.003

[14] Liu WB, Zhang SC, Li N, Zheng JW, Xing YL. Microstructure evolution of monolithic nanoporous copper from dual-phase Al 35 atom% Cu alloy. Journal of the Electrochemical Society. 2010;**157**:D666-D670. DOI: 10.1149/1.3497308

[15] Liu WB, Zhang SC, Li N, Zheng JW, Xing YL. Dealloying behaviour of dual-phase Al 40 atom % Cu alloy in an alkaline solution. Journal of the Electrochemical Society. 2011;**158**:D91-D94. DOI: 10.1149/1.3511771

[16] Liu WB, Zhang SC, Li N, Zheng JW, Xing YL. Influence of phase constituent and pro-portion in initial Al-Cu alloys on formation of monolithic nanoporous copper through chemical dealloying in an alkaline solution. Corrosion Science. 2011;**53**:809-814. DOI: 10.1016 /j.corsci.2010.11.017

[17] Hayes JR, Hodge AM, Biener J, Hamza AV. Monolithic nanoporous copper by dealloying Mn-Cu. Journal of Materials Research. 2006;**21**:2611-2616. DOI: 10.1557/jmr.2006.0322

[18] Chen LY, Yu JS, Fujita T, Chen MW. Nanoporous copper with tunable nanoporosity for SERS applications. Advanced Functional Materials. 2009;**19**:1221-1226. DOI: 10.1002/ adfm.200801239

[19] Lu HB, Li Y, Wang FH. Synthesis of porous copper from nanocrystalline two-phase Cu-Zr film by dealloying. Scripta Materialia. 2007;**56**:165-168. DOI: 10.1016/j.scriptamat.2006.09.009

[20] Dan ZH, Qin FX, Sugawara Y, Muto I, Hara N. Fabrication of nanoporous copper by dealloying amorphous binary Ti-Cu alloys in hydrofluoric acid solutions. Intermetallics. 2012;**29**:14-20. DOI: 10.1016/j.intermet.2012.04.016

[21] Pugh DV, Dursun A, Corcoran SG. Formation of nanoporous platinum by selective dissolution of Cu from $Cu_{0.75}Pt_{0.25}$. Journal of Materials Research. 2003;**18**:216-221. DOI: 10.1557/JMR.2003.0030

[22] Biener J, Hodge AM, Hayes JR, Volkert CA, Zepeda-Ruiz LA, Hamza AV, Abraham FF. Size effects on the mechanical behavior of nanoporous Au. Nano Letters. 2006;**6**:2379-2382. DOI: 10.1021/nl061978i

[23] Qian LH, Chen MW. Ultrafine nanoporous gold by low-temperature dealloying and kinetics of nanopore formation. Applied Physics Letters. 2007;**91**:083105. DOI: 10.1063/1.2773757

[24] Snyder J, Asanithi P, Dalton AB, Erlebacher J. Stabilized nanoporous metals by dealloying ternary alloy precursors. Advanced Materials. 2008;**20**:4883-4886. DOI: 10.1002/adma.200702760

[25] Sun JZ, Yan XJ, Zhao BG, Liu L, Gao YL, Zhang ZH. Modulation of compositions and electrocatalytic activities of quaternary nanoporous Pt-based alloys via controllable dealloying. International Journal of Hydrogen Energy. 2016;**41**:9476-9489. DOI: 10.1016/j.ijhydene.2016.04.098

[26] Dan ZH, Qin FX, Sugawara Y, Muto I, Hara N. Dependency of the formation of Au-stabilized nanoporous copper on the dealloying temperature. Microporous and Mesoporous Materials. 2014;**186**:181-186. DOI: 10.1016/j.micromeso.2013.12.003

[27] Dan ZH, Qin FX, Sugawara Y, Muto I, Hara N. Elaboration of nanoporous copper by modifying surface diffusivity by the minor addition of gold. Microporous and Mesoporous Materials. 2013;**165**:257-264. DOI: 10.1016/j.micromeso.2012.08.026

[28] Dan ZH, Qin FX, Makino A, Sugawara Y, Muto I, Hara N. Fabrication of nanoporous copper by dealloying of amorphous Ti-Cu-Ag alloys. Journal of Alloys and Compounds. 2014;**586**:S134-S138. DOI: 10.1016/j.jallcom.2013.01.087

[29] Dan ZH, Qin FX, Sugawara Y, Muto I, Makino A, Hara N. Nickel-stabilized nanoporous copper fabricated from ternary TiCuNi amorphous alloys. Materials Letters. 2013;**94**:128-131. DOI: 10.1016/j.matlet.2012.12.028

[30] Dan ZH, Qin FX, Hara N. Refinement of Nanoporous copper: A summary of micro-alloying of Au-group and Pt-group elements. Materials Transactions. 2014;**55**:796-800. DOI: 10.2320/matertrans.M2013445

[31] Qin FX, Dan ZH, Hara N, Li WR, Li YD. Selective dissolution of an amorphous $Mg_{65}Cu_{25}Y_{10}$ alloy in organic acids and dilute HCl solution. Materials Chemistry and Physics. 2016;**179**:27-34. DOI: 10.1016/j.matchemphys.2016.05.001

[32] Dan ZH, Qin FX, Hara N. Polyvinylpyrrolidone macromolecules function as a diffusion barrier during dealloying. Materials Chemistry and Physics. 2014;**146**:277-282. DOI: 10.1016/j.matchemphys.2014.03.022

[33] Dan ZH, Qin FX, Yamaura S, Xie GQ, Makino A, Hara N. Refinement of nanoporous copper by dealloying MgCuY amorphous alloys in sulfuric acids containing polyvinylpyrrolidone. Journal of the Electrochemical Society. 2014;**161**:C120-C125. DOI: 10.1149/2.076403jes

[34] Thorp JC, Sieradzki K, Tang L, Crozier PA, Misra A, Nastasi M, Mitlin D, Picraux ST. Formation of nanoporous noble metal thin films by electrochemical dealloying of Pt_xSi_{1-x}. Applied Physics Letter. 2006;**88**:033110. DOI: 10.1063/1.2161939

[35] Wang XG, Qi Z, Zhao CC, Wang WM, Zhang ZH. Influence of alloy composition and dealloying solution on the formation and microstructure of monolithic nanoporous silver through chemical dealloying of Al-Ag alloys. The Journal of Physical Chemistry C. 2009;**113**:13139-13150. DOI: 10.1021/jp902490u

[36] Klement W, Willens RH, Duwez P. Non-crystalline structure in solidified gold-silicon alloys. Nature. 1960;**187**:869-870. DOI: 10.1038/187869b0

[37] Inoue A, Wang XM. Bulk amorphous FC20 (Fe-C-Si) alloys with small amounts of B and their crystallized structure and mechanical properties. Acta Materialia. 2000;**48**:1383-1395. DOI: 10.1016/S1359-6454(99)00394-8

[38] Ding Y, Kim YJ, Erlebacher J. Nanoporous gold leaf ancient technology. Advanced Materials. 2004;**16**:1897-1900. DOI: 10.1002/adma.200400792

[39] Kumar G, Singh DB, Tripathi VK. Surface enhanced Raman scattering of a surface plasma wave. Journal of Physics D: Applied Physics. 2006;**39**:4436-4439. DOI: 10.1088/0022-3727/39/20/021

[40] Tyson WR, Miller WA. Surface free energies of solid metals: Estimation from liquid surface tension measurements. Surface Science. 1977;**62**:267-276. DOI: 10.1016/0039-6028(77)90442-3

[41] Hakamada M, Mabuchi M. Preparation of nanoporous Ni and Ni-Cu by dealloying of rolled Ni-Mn and Ni-Cu-Mn alloys. Journal of Alloys and Compounds. 2009;**485**:583-587. DOI: 10.1016/j.jallcom.2009.06.031

[42] Dona JM, Gonzalez-Velasco J. Mechanism of surface diffusion of gold adatoms in contact with an electrolytic solution. The Journal of Physical Chemistry. 1993;**97**:4714-4719. DOI: 0022-3654/93/2097-47 14%04.00/

[43] Martienssen W, Warlimont H, editors. Springer Handbook of Condensed Matter and Materials Data. Springer Science & Business Media; 2006

[44] Ghosh G. Dissolution and interfacial reactions of thin-film Ti/Ni/Ag metallizations in solder joints. Acta Materialia. 2001;**49**:2609-2624. DOI: 10.1016/S1359-6454(01)00187-2

[45] Makin SM, Rowe AH, LeClaire AD. Self-diffusion in gold. Proceedings of the Physical Society. Section B. 1957;**70**:545-552. DOI: 10.1088/0370-1301/70/6/301

[46] Wang J, Liu HS, Liu LB, Jin ZP. Assessment of diffusion mobilities in FCC Cu-Ni alloys. Calphad. 2008;**32**:94-100. DOI: 10.1016/j.calphad.2007.08.001

[47] Wang CP, Yan LN, Han JJ, Liu XJ. Diffusion mobilities in the fcc Ag-Cu and Ag-Pd alloys. Calphad. 2012;**37**:57-64. DOI: 10.1016/j.calphad.2012.01.001

[48] Liu CL, Cohen JM, Adams JB, Voter AF. EAM study of surface self-diffusion of single adatoms of fee metals Ni, Cu, Al, Ag, Au, Pd, and Pt. Surface Science. 1991;**253**:334-344. DOI: 10.1016/0039-6028(91)90604-Q

[49] Samsonov GV. Handbook of the Physicochemical Properties of the Elements. Springer US; 1968

[50] Evangelakis GA, Kallinteris C, Papanicolaou NI. Molecular dynamics study of gold adatom diffusion on low-index copper surfaces. Surface Science. 1997;**394**:185-191. DOI: 10.1016/S0039-6028(97)00606-7

[51] Wang XD, Bednarcik J, Saksl K, Franz H, Cao QP, Jiang JZ. Tensile behavior of bulk metallic glasses by in situ X-ray diffraction. Applied Physics Letters. 2007;**081913**(1-3):91. DOI: 10.1063/1.2773945

[52] Wang XG, Sun JZ, Zhang C, Kou TY, Zhang ZH. On the microstructure, chemical composition, and porosity evolution of nanoporous alloy through successive dealloying of ternary Al-Pd-au precursor. The Journal of Physical Chemistry C. 2012;**116**:13271-13280. DOI: 10.1021/jp3035677

Sub-2 μm Silica Particles in Chiral Separation

Diana Ibrahim and Ashraf Ghanem

Additional information is available at the end of the chapter

Abstract

For decades, the race for the shortest chromatogram with the best resolution and separation efficiency has been the focus of researchers and manufacturers. Considerable advancement has been attained in the field of separation science with the widespread applications and outstanding performance of nanomaterials. According to the van Deemter equation, sub-2 micron particles employed in a conventional HPLC short column should subsequently result in analysis time reduction and efficiency improvements without the drawbacks of high pressure associated with sub-2 micron particles. This chapter provides comprehensive discussion about the applications of the new sub 2 microns silica particles in chiral separation of racemates.

Keywords: CHIRALPAK IG-U, HPLC, chiral separation, sub-2 micron, nanomaterials

1. Introduction

1.1. Nanomaterials as stationary phases in separation science

Nanomaterials are nanostructures with sizes in the range of approximately 1–100 nm [1]. These nanomaterials frequently have chemical and physical characteristics that are distinct from those of their macroscopic counterparts [1]. They can be exploited in many fields of science and technology including separation science [2]. In separation science, this term often refers to nano-materials-based stationary phases used to separate chemical compounds [2]. Widespread applications and outstanding performance of nanomaterials have not only accelerated the development of separation science, but also offer many opportunities in other related disciplines, and have a significant impact on many fields of science [2, 3]. Separation science is based on the application of broad chromatographic techniques to achieve separations of compounds. Such separation is achieved by regulating the magnitude of the distribution

IntechOpen

coefficient between two distinct phases namely the stationary and the mobile phases [1–3]. The components separate as they migrate with different rates depending on their unique distribution coefficients, they separate [4]. Different chromatographic techniques are available depending on the type of the phases [4]. The chromatography is known to be liquid chromatography (LC) when it employs a liquid mobile phase [5]. The most sophisticated form of LC is High-performance liquid chromatography (HPLC) where the mobile phase passes through the stationary via a pump at high pressures [4, 5].

2. Applications of nanomaterials in HPLC stationary phases

In conventional HPLC, the stationary phase (SP) plays a pivotal role in the separation technique [5]. The packing particles constituting the SP are of several micrometres in diameter with nanometre-sized pores [6]. Therefore, the industry has pushed researchers to investigate new packing materials as an attempt to achieve high throughput with robust analysis [6]. Packings in HPLC can be divided into three types-polymeric, inorganic, and hybrid materials. At present, inorganic materials, which include silica, hydroxyapatite, graphite, and metal oxides, etc. are widely used in research and applications [7]. Among these materials, silica is almost ideal support given its favourable characteristics, for example, good mechanical strength, high chemical and thermal stability, controllable pore structure and surface area, etc. [7]. Therefore, silica has been developed as the most widely used HPLC packing material [6, 7]. Throughout the years, many silica stationary phases (both porous and non-porous) have been commercialised and widely applied for analysis of pharmaceutical and biological samples [8].

2.1. Porous and non-porous nanomaterials

Non-porous and porous particles are the two major types of spherical packing materials used in HPLC [8]. The significant difference between both particles is that porous particles
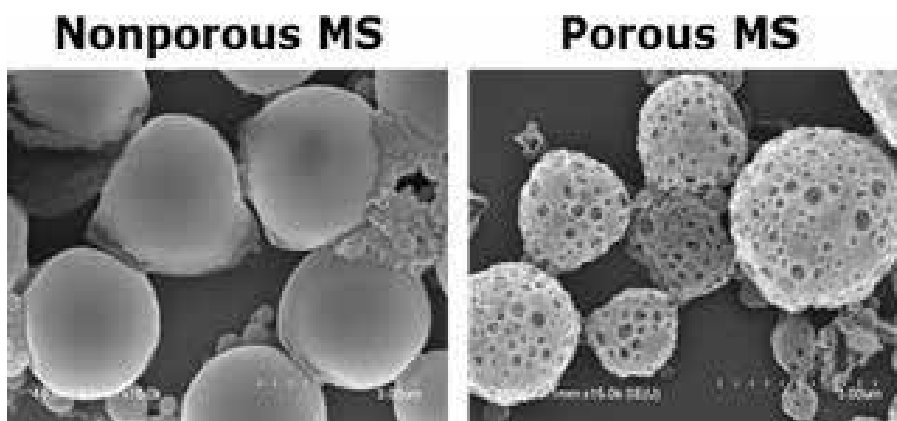
Figure 1. The difference in surface area between porous and non-porous microspheres under scanning electron microspray [2].

have resistance to mass transfer contribution from the stagnant mobile phase in the pores [8]. Decreasing the particle size and increasing the diffusion coefficient can improve the mass transfer of solutes in the mobile phase [3, 5]. Non-porous particles can provide lower mass transfer resistance and higher efficiency than porous particles [8]. However, porous particles have higher surface areas (**Figure 1**) and can provide much higher sample loading capacity [8].

On the other hand, in porous particles, solutes transfer from the mobile phase exterior to the particles into the mobile phase within the pores to interact with the chiral stationary phase (CSP) [9]. Following this interaction, the solute molecule must diffuse out of the particle and continue its journey down the column ahead of the solute [5, 9]. This slow rate of mass transfer into and out of the porous particle is a source of HPLC band broadening [9]. **Figure 2** illustrates a reduction in particle size shortens the path length of this diffusion process, improves mass transfer, and provides better efficiency [9].
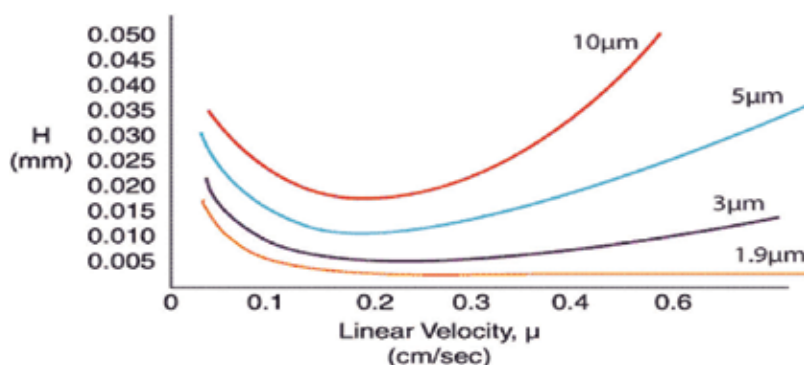
Figure 2. Smaller particle sizes increase efficiency and result in a wider range of flow rates [9].

3. Effect of particle size on the separation efficiency, speed and resolution of chiral separations

3.1. Relationship between particle size, and column efficiency

Particle size is known to be the mean diameter of the spherical support employed in column packing [6]. This physical dimension significantly impacts HPLC column performance [9]. A decrease in particle size increases peak efficiencies (**Figure 2**). This is based on the resolution equation (Eq. (1)) which comprise of three terms: selectivity, retention capacity, and efficiency [10]. The components of an analytical method alter each of these terms. In particular, the column's particle size affects the efficiency factor from the equation [10]. Efficiency is a qualitative term used to measure the number of theoretical plates in a column. Put simply, as particle size is lowered, efficiency increases, and more resolution is achieved [10].

$$R_S = 2(t_{R,2} - t_{R,1})/(w_{b,1} + w_{b,2}) \tag{1}$$

Burns et al. observed a nearly linear correlation between the width of the particle size distribution of commercially available HPLC particles and the minimum reduced plate height, the van Deemter equation (VDE) A-term and the minimum reduced separation impedance [10, 11]. Column efficiency in HPLC is influenced by a number of factors such as particle size, flow rate and degree of cross-linkage of gels [12]. Particle size distribution (PSD) of packing materials is also considered one of the important factors [12]. It has been empirically found that column efficiency is improved by narrowing the PSD [11, 12]. Because the greatest the achievable plate height is, the more effective the PSD has on the separation efficiency [12]. On one side, column efficiency or plate number is dependent on particle size, and the pore size controls the surface area where retention is controlled primarily by the surface area [9–12].

3.2. The impact of the pore size of silica gel on the CSPs

Retention is directly related to surface area; therefore, the use of large-pore columns is not desirable when small-pore columns can be used [13]. Selection of the pore size is based on providing easy access for the molecules to the pores in the column [10–12]. Consequently, the higher surface area associated with small pore-columns is preferred mainly because the analytes are small enough to pass through the pores [12, 13].

The performance of the CSP increases with pore size when the pore diameter is large enough for the penetration of macromolecules [13]. Specific surface area and, therefore, the number of silanol groups on the surface of the silica gel, decreases with increasing of pore size; consequently, the bound amount of the chiral selector depends on the pore size of silica matrix [13]. The particle size of silica gel has a major effect on the performance of the column, increasing the particle size from 3 to 10 μ decreased the theoretical plate number [13]. A reduction in particle size can lead to more compact and stable packing and thus better column efficiency.

3.3. Chromatographic effects of varying particle size and size distributions

In the late 1960s, Horvath and coworkers introduced columns packed with rigid pellicular particles (40–50 μ) applicable under high pressures [14]. The thin porous coat allowed for robust solute mass transfer through the packing, hence, improving column efficiency. However, pellicular particles had a drawback of low sample capacity [16]. In the 1970s, large porous/pellicular particles were reduced down to smaller porous particles of 10 μ to eliminate the drawbacks of pellicular materials [16]. However, particles of silica smaller than 40 μ have demonstrated some difficulties with packing reproducibility [17]. Irregular shapes of microporous particles were used throughout the 1970s until the spherical material was obtained and improved. In the 1980s, 5 μ became the standard particle diameter, and in the early 1990s, 3–3.5 μ particle diameters were also commercially available [16, 17]. The latter demonstrated 30–50% faster analysis times and higher efficiencies compared to 5 μ. Methods can be easily transferred from 5 μ to similar 3 stationary phases [14–17] (**Figure 3**) [15].

History of HPLC Particle Development

Year(s) of Acceptance	Particle Size	Most Popular Nominal Size	Plates / 15cm
1950's		100μm	200
1967		57μm (pellicular)	1,000
1972		10μm	6,000
1985		5μm	12,000
1992		3.5μm	22,000
2003		≤2μm*	>30,000

Figure 3. The reduction of particle packing throughout the years in hope for the shortest fastest chromatogram [16].

4. Small-particle (sub-2-μm) columns for high efficiency and speed

Separation efficiency is inversely proportional to the stationary phase diameter [17]. Stationary phase manufacturers have reduced particles for packing down to micron-sized [17]. If packing materials could be further reduced in the future down to the nanometre scale, the band dispersion would consequently be reduced further by 6 magnitude orders [17, 18]. As a consequence, in 2004, the first available porous silica with small particle size was commercialised (1.7 μ), which allowed better resolution compared to the current 5 or 3.5 μ [18]. Several column suppliers now offer columns packed with particles in the range of 1.5–2 μ [18]. The term sub-2 micron, including particles of 2 μ, is used in this work for the sake of clarity [19]. Different works, dealing with drug and metabolites analysis, bioanalytical as well as environmental separations, compared columns packed with 5 μ and sub-2 micron supports and demonstrated that the latter clearly reduced the analysis time with comparable efficiency [20]. However, the quest towards the use of nanomaterials in chromatography has encountered serious challenges such as extremely high back pressures and problems associated with frits [20, 21].

The high back pressure is induced by the friction of the mobile phase percolating through the sub-2 μm particles stationary phase, generating heat that can be detrimental to the separations [22]. Studies suggest that reducing column internal diameter (i.d.) minimised frictional heating effect from the radial temperature gradient [22, 23]. This is due to fast heat dissipation within such a narrow-bore column [23]. As column length is proportional to the particle size, shortening the columns lead to fast separation with sub-2 μm particles [23].

As shown in **Figure 4**, sub-2 micron particles are noted to be highly efficient and hence, the column length can be shortened while maintaining resolution in a shorter analysis time [23]. To achieve fast separations, short columns and high flow rates are necessary. In such columns, it can be practically difficult to achieve axially and radially homogenous beds [24]. It seems more logical to use smaller diameter columns, such as 3 mm i.d. when using sub-2 micron particles [23, 24]. This significantly reduces the flow rate required to achieve optimum efficiency, which in turn minimises the extra-column dispersion caused by the tubing [25]. Higher linear velocities can be achieved at lower flow rates, with much lower pressure drops in the tubing [25].

If the main goal is reducing analysis time, an increase in the flow rate above the optimum rate allows for robust separations, while maintaining resolution due to the small particles lower mass transfer resistance [24]. On the other side, if the primary goal is higher resolution, maintaining column length can increase resolution with a subsequent increase in analysis time [24]. Particle size reduction has more effect than column length, gradient time, or flow-rate to improve peak capacity in gradient mode [26]. However, these small particles can generate a high bp incompatible with conventional instrumentation [27]. It is evident that a reduction in particle size reduces backpressure because of the inverse square relationship between them [27]. As a result, new HPLC instrumentation such as ultra-high performance liquid chromatography (UHPLC) has been developed to handle elevated pressures above 400 bar [27]. However, employing shorter columns with smaller particles (i.e. sub-2 micron) have the ability to combine high resolution without exceeding the pressure limit of 400 bar associated with conventional HPLC [23–27].

4.1. Van Deemter analysis of sub-2 micron CSPs

According to VDE, the A- and C-terms are directly proportional to the particle size [28]. Therefore, the use of smaller particles provides a decrease of the plate height together with a flatter profile of the right branch of the van Deemter curve [28]. A reduction in column i.d. results in less chromatographic dilution and, consequently, increased concentration of the injected sample on LC system [25]. The chromatographic dilution increases proportionally
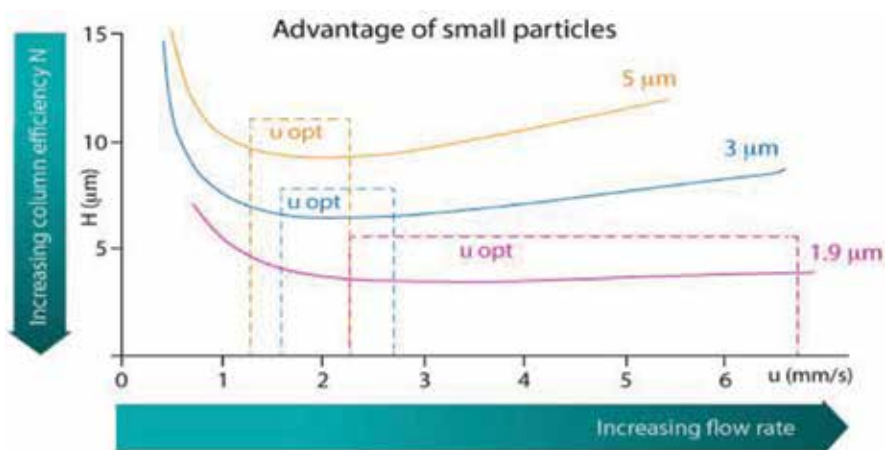
Figure 4. A reduction in particle size results in an increase in column efficiency, a wider range of flow rates is applicable for small particles [23].

with the square of the column radius and with the square root of column length [29]. Thus, a reduction in column diameter results in a significantly lower dilution factor, thereby increasing the concentration in the eluted peak [29]. Downscaling the column used in an analytical method should result in an almost 4000-fold gain in sensitivity [28]. With the reduction in particle size, column efficiency improved further allowing a reduction in column length. Shorter columns are now in vogue [28]. Not only does a shorter column provide faster separations but also solvent use is reduced [28]. Columns of 50 mm in length now provide plate counts formerly obtained on 15- and 25-cm columns packed with larger particles [25, 28, 29]. The sub-2-μm columns have struck the fancy of those who wish to decrease their analysis times by shortening the column length and to those who want to have greater plate count by using longer columns, albeit at the higher pressure [25, 28, 29].

The equation demonstrated the obvious advantage of using small particles to decrease plate height [30]. The chromatographic separating power of HPLC is dependent upon the selectivity of the mobile/stationary phase and the efficiency of the column [12, 13]. The column efficiency is dependent upon multiple factors most importantly: the column length and the packing particle size together with the mobile phase velocity [22]. At a fixed velocity, the column efficiency increases in direct proportion to the column length [24]. At the minimum of the plate height versus velocity curve, the column efficiency increases in inverse proportion with the particle size [22, 24].

As seen in **Figure 5**, van Deemter equation describes that efficiency varies with the linear velocity, and the nature of the second and third terms of the equation indicates a minimum value for plate height (HETP) [31]. In the third term of van Deemter equation, the particle size is squared, and so the curve is steeper for larger particles at high linear velocities [31]. The A term depends
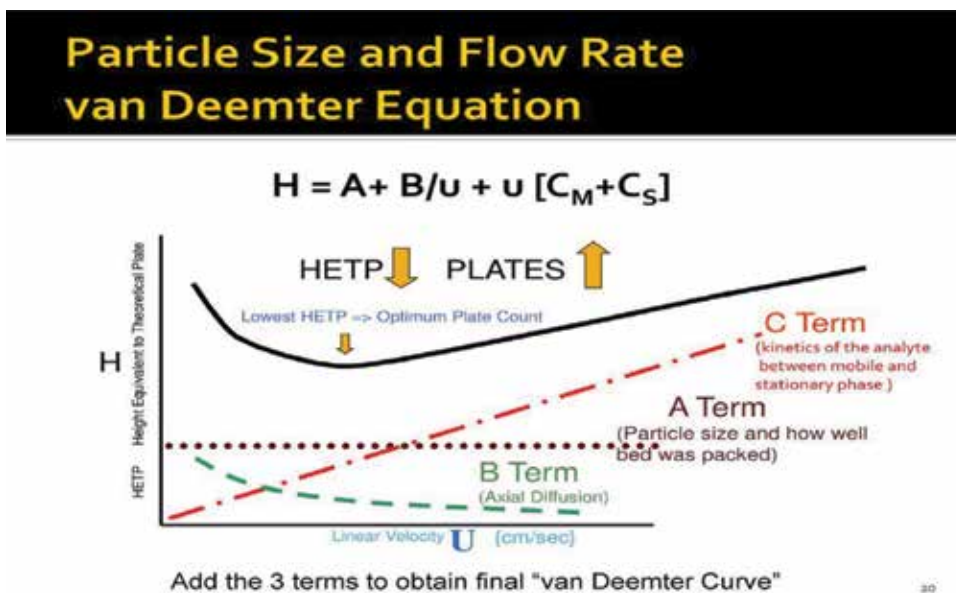
Figure 5. Van Deemter equation describes that efficiency varies with the linear velocity, and the second and third terms indicates a minimum value for HETP [31].

on both the quality of the column packing and the contribution values of the coefficients A, B and C for the different columns, can be accounted for by the minor contribution of several effects (packing characteristics and the combined effects of frictional heating and high pressure) on the velocity-dependence of the plate height. B- and C-terms of the equation depend on analyte retention [32]. The B-term is expected to increase with analyte retention as more time is available for diffusion to take place in the mobile phase [32]. According to the theory, smaller particles should perform lower plate heights and higher optimum linear velocity [31, 32].

The dependence of the third term (C-term), is considered to represent mainly the resistance to mass transfer in the mobile phase, on the square of the particle size translates into a substantial decrease in the plate height with smaller particles, especially at high linear velocities [33]. Small particle diameters induce an increase in efficiency, optimal velocity and mass transfer. Sub-2 micron particles packed into shorter column permit shorter analysis time along with using less solvent without compromising the resolution between closely eluting peaks [34]. Because the H-u curves are flatter (lower C term) for the smaller particle diameters, they also allow conducting separations at linear velocities higher than the optimum without significant loss of efficiency [34]. Using small diameter packing material reduces eddy diffusion and mass transfer resistance in the mobile phase [28, 33]. Van Deemter realised a correlation between increasing peak efficiency and a reduction in particle size [28, 34].

Optimization of efficiency and analysis time can be useful but generally leads to a large increase in the analysis time [35]. Instead, tuning the column length together with the stationary phase morphology (e.g. particle size) can result in a better compromise between the plate count and analysis time [36, 37]. Column length and plate count are related through the height equivalent to one theoretical plate with the relationship between the theoretical plate and mobile phase velocity described by VDE as the sum of different band-broadening contributions [34–36].

Based on VDE, the solution for enhancing chromatographic performance is to use shorter columns with small particle diameters (i.e. sub-2 micron particles) to induce a simultaneous improvement in efficiency, optimal velocity and mass transfer. The use of these sub-2 micron materials in LC is examined, including their applications in normal-phase LC, reversed-phase LC. In this study, the possibilities and restrictions of chromatographic separations obtained with 5 cm long bore columns packed with sub-2 micron particles is presented. Performance of columns immobilised on silica gel with different internal diameters and different lengths will be briefly mentioned to provide an overview of the miniaturisation of HPLC column technology.

5. Performance of CHIRALPAK IG-U®: In terms of enantioselectivity and solvent versatility

In recent years, column miniaturisation has been investigated and tested in order to achieve highly sensitive chromatography [38]. The miniaturised columns are better for handling minute and/or dilute samples, especially in an area such as forensic science and sport drug trails [38]. The idea of miniaturisation is to provide higher sensitivity and peak capacity than standard columns with minimal dead volume for small sample amounts [39]. Narrow-bore

columns are used on a conventional HPLC system [24]. The sub-2 micron silica-based stationary phases have established themselves as an effective analytical tool in achiral applications, but in the field of chiral separations, the technology related to the development of sub-2 micron CSPs is still not used in the market on conventional HPLC [40–43].

Daicel group recently commercialised a sub-2 micron 5 cm column applicable for use on conventional HPLC [44]. The design is based on the simple way of reducing solvent usage by using a shorter column. A more dynamic saving in solvent usage is made by reducing the i.d. of the column, together with an appropriate scaling down in the flow rate [44]. Separation efficiencies are also recovered by reducing particle size down to sub-2 micron; because columns packed with sub-2 micron particles offer advantages over the more traditional systems containing 3 and 5 micron particles by allowing operation at higher flow rates without compromising efficiency [45]. Consequently, this results in shorter analysis times and a reduction in solvent consumption, together with associated improvements in resolving power, sensitivity and peak capacity [45].

Ghanem et al. [46] investigated the impact of reducing the three VDE parameters (Length, i.d. and particle size) on separation and efficiency via the transition from conventional CHIRALPAK IG® to the sub-2 micron CHIRALPAK IG-U®. The effects of miniaturising the three column parameters (i.d., length and particle size) five times from CHIRALPAK IG® (250 mm length, 4.6 mm i.d., and 5 mm particle size) to CHIRALPAK IG-U® (50 mm length, 3 mm i.d., and 1.6 μm or sub-2 micron particle size) using similar CSP amylose *tris* (3-chloro-5-methylphenylcarbamate) for the enantioselective separation of racemates under normal standard, non-standard organic phase, and reversed-phase chromatographic conditions are discussed below [47].

Pore size influences several factors such as: the retention factor, the separation factor, and the resolution of racemates was also examined. CHIRALPAK IG-U® has been tested in normal-phase mode chromatographic separation consisting of *n*-hexane/ethanol screened from 90:10 to 10:90 v/v at 1 mL/min flow rate on CHIRALPAK IG-U® at fixed UV detection 245 nm. Out of the twenty-eight compounds tested, eleven compounds (Naftopidil, Naproxen, Indoprofen, Cizolitrine, Carprofen, Miconazole, Nomifensine, Tocainide, Propafenone, Flavanone, and 6-Hydroxyflavanone) were partially, or baseline separated under either 90:10 or 80:20 v/v *n*-hexane/ethanol mobile phase. Substituting ethanol (EtOH) with 2-propanol (2-PrOH) resulted in the separation of only seven compounds (Naftopidil, Carprofen, Sulconazole, Propafenone, Flavanone, 6-Hydroxyflavanone, and 1-Acenaphthenol) under either 90:10, 80:20, 70:30 or 60:40 v/v n-hexane/2-PrOH. Regarding resolution (Rs) and separation factor (α), EtOH in mobile phase system showed better results than 2-PrOH where (Naproxen, Indoprofen, Miconazole, Nomifensine, and Tocainide) were all separated when 2-PrOH was replaced by n-hexane (See **Figure 6** for examples). This is mainly because the mobile phase travels easily in large spaces between particles and hence particle size affect permeability; smaller particles can be packed closer together, thus, using ethanol resulted in the best separation with the highest resolution and separation factor [46, 47].

CHIRALPAK IG-U® showed great performance in different solvents such as non-standard solvents namely dichloromethane, tetrahydrofuran and Methyl *tert* Butyl Ether [46]. The
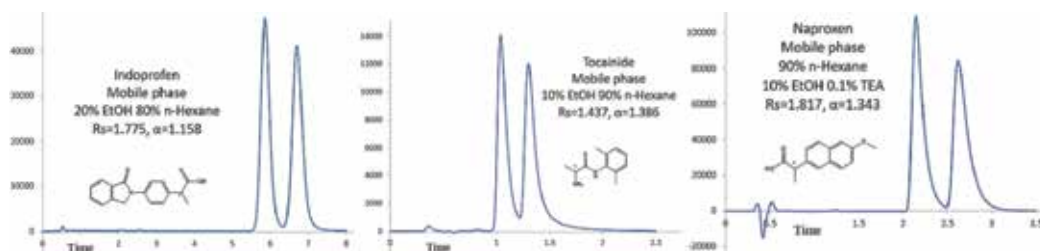
Figure 6. The effect of EtOH in mobile phase composition on Indoprofen, Naproxen, and Tocainide.

addition of non-standard solvents in mobile phase composition enhanced resolution and separation in several tested racemates for example, in case of Tocainide, Rs 1.44 and α 1.39 in standard solvents namely n-hexane/EtOH 90:10 v/v were enhanced to Rs 1.89 and α 1.66 when using non-standard solvent in mobile phase composition (*n*-hexane/DCM/EtOH 50/50/0.2 *v/v/v*) (**Figure 7**) [47]. Of interest, compound 1-phenyl-2,2,2-trifluorethanol which was not resolved under any standard solvents' combination investigated, was baseline separated under non-standard organic solvent (MtBE/EtOH 40/60% *v/v*) with Rs 1.55 and α 1.78. Similarly, compounds Aminoglutethimide and α-Methyl DOPA were only separated under non-standard organic mobile phase composition (MtBE/EtOH 40:60 *v/v*) and (*n*-hexane/DCM 85%/15% *v/v*) [47]. The chiral recognition of sub 2-micron column CHIRALPAK IG-U® is like that of CHIRALPAK IG® where polarity is playing a role. Another reason might be the stereo environment of the chiral cavities in amylose derivatives which might be favorable in the presence of ethanol. Other researchers have speculated that the configuration of the chiral cavities in the amylose tris (3,5-dimethylphenyl carbamate) is determined by the composition of mobile phase in normal phase mode while the configuration of reversed phase mode remains unchanged. It is of essential to note that the chiral recognition is due to different factors such as hydrogen bonding, π-π interactions and the chiral cavities of CSPs with specific configuration responsible for bonding of varying magnitude between the stationary phase and enantiomers [46, 47]. CHIRALPAK IG-U® was investigated under reversed-phase conditions including ACN and H_2O ranging from 10 to 90% (v/v) [46]. The resolution and separation factors were enhanced in several compounds compared to other separations
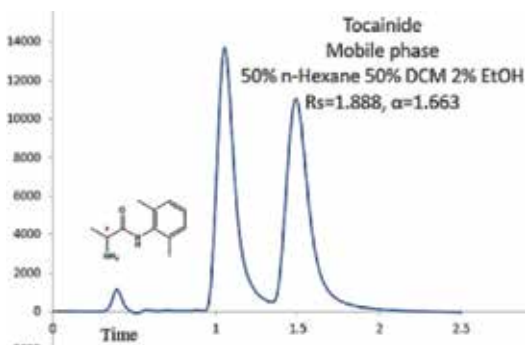
Figure 7. Tocainide resolution and separation factor were enhanced from (Rs:1.44 and α:1.39) under standard solvent (n-hexane/EtOH 90:10 v/v) to (Rs:1.89 and α:1.66) under non-standard solvent (*n*-hexane/DCM/EtOH 50:50:0.2 v/v/v).

achieved under standard and non-standard organic solvents. For example, few separations were achieved for compounds (Naftopidil, Miconazole, Sulconazole, Aminoglutethimide, Tocainide, Propafenone, Flavanone, and 6-Hydroxyflavanone). Compound Naftopidil was baseline separated with a Rs of 2.56 and α 1.62 under (ACN/H_2O/TEA 80:20:0.1% v/v/v) (**Figure 8**) [47]. Similarly, in case of compound Aminoglutethimide; Rs 1.90 and α 1.34 were superior to other separations achieved under standard and non-standard organic solvents. Compound 6-Hydroxyflavanone which was separated under standard and non-standard solvents, was separated under reversed phase condition (ACN/H_2O/TEA 40:60:0.1% v/v/v) with superior Rs 2.39 and α 2.71 (**Figure 8**) [47].

According to the following results and VDE Ghanem et al. [46, 47] and VDE, all three parameters (length, i.d., and particle size) reduced in the transition from conventional CHIRALPAK IG® to the sub-2 micron CHIRALPAK IG-U® resulted in an enhanced separation and resolution (**Figure 9**). However, Practical difficulties that one can expect following the sub-2-micron particle approach are twofold: one is inherently related to the decrease of column permeability
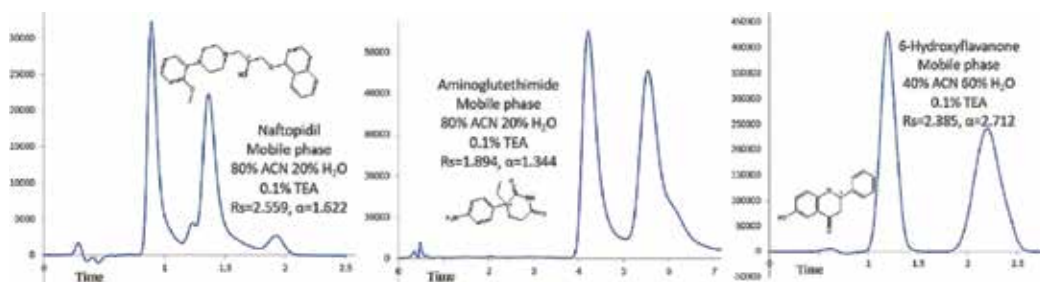
Figure 8. Naftopidil was baseline separated with a Rs of 2.56 and α 1.62 under reversed phase solvent composition (ACN/H_2O/TEA 80:20:0.1% v/v/v). Aminoglutethimide with Rs 1.90 and α 1.34 were superior to other separations achieved under standard and non-standard organic solvents. Compound 6-Hydroxyflavanone which was separated under standard and non-standard solvents, was separated under reversed phase condition (ACN/H_2O/TEA 40:60:0.1% v/v/v) with superior Rs 2.39 and α 2.71.
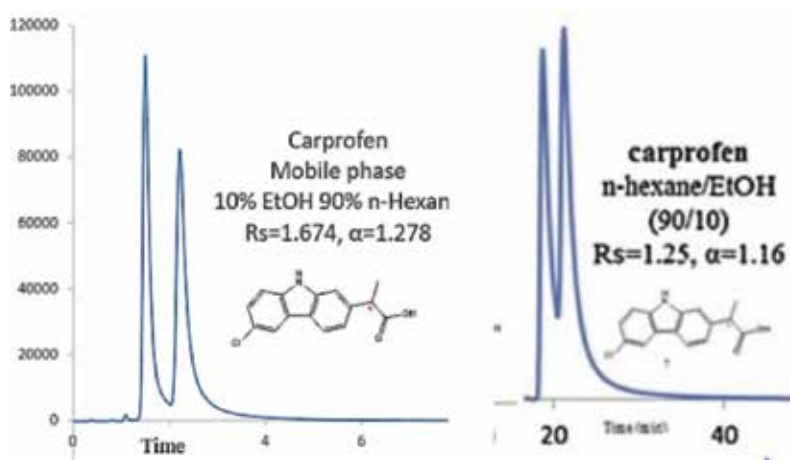
Figure 9. CHIRALPAK IG-U® (left side) shows enhanced separation and resolution in shorter time of 2 minutes compared to 20 minutes using the CHIRALPAK IG® (right side).

that accompanies the particle size reduction; the other one is associated to the adaptation of the surface modification chemistry of classical CSPs to smaller particles [21–26].

The column permeability reduction is linked to the increase in pressure that is proportional to the inverse of the particle diameter squared: thus, reducing the particle diameter by a factor of 3 will result in a ninefold increase in the column back pressure [48]. As a consequence, depending on the column length and eluents viscosity, the full potential of high-speed separations can only be exploited on chromatographic hardware that can withstand elevated pressures (UHPLC) [49]. An additional complication may arise from the pronounced propensity of the smaller particles to aggregate during synthetic steps leading to a final stationary phase with non-optimal performances primarily regarding permeability and/or efficiency [18]. Mechanical resistance and long-term stability of the packed bed are also of significant concern when high flow (and hence high pressure) applications are planned [18].

This area needs considerable attention as solvent efficient narrow-bore columns have already become mainstream for 'greener' chromatography [50]. For ultrafast separations, the sub-2- μm totally porous particles provide better solutions [18, 48]. Thus it can be a viable option to achieve ultrafast separations with slightly lower efficiency, but without a large investment in ultrahigh-pressure instruments [49].

6. Future perspectives

Instruments have been trying to follow the footpath of column developments [51]. The life cycle for instrument development is much longer than what is required for new packings and columns [52]. An area that has been delaying further improvements in column efficiency is the instrument contribution to band dispersion associated with HPLC and UHPLC instruments and their column-instrument interface designs [53]. Integration of column hardware and instrument connections are essential to eliminate dead volumes, much like what has been achieved in some nano and chip instruments [53]. The area of frit and end fitting design needs attention since the column packing where the separation takes place should be located at or near the injector device and the detector measurement device [52, 53]. This may necessitate a new column design that not only cuts down on this extra-column volume but can handle higher pressures associated with smaller particles [53].

Reducing the column i.d. is the first of several critical steps in miniaturising a LC system. Extra column peak broadening must be reduced accordingly to preserve optimal performance [54]. Excessive extra column band-broadening causes considerable loss of separation efficiency and, thereby, sensitivity. Connection tubing should be kept as short and especially as narrow as possible to minimise extra column band broadening and result in an acceptable increase in back pressure [35, 54]. Making connections with silica capillaries can be a challenge to less-experienced users and often has been considered the most difficult part of setting up a nano-liquid chromatography (nano-LC) system [55].LC system implies that all system components should be downscaled, including column, connecting tubing, connections, injector, and the interface to the detector [55]. Nano-LC columns typically require flow rates of 500 nL/min or less [35]. Achieving reproducible flow and gradient formation requires dedicated approaches.

Ideally, the flow should not be split and used directly from the pump as it is used in standard HPLC [35]. These nano-LC systems are often called splitless systems and are commercially available [53]. The direct flow systems can be divided into two groups: the 'solvent refill' systems and the 'continuous flow' systems [53]. Commonly, these systems also are capable of operating at UHPLC pressures. Whereas UHPLC is mostly used to increase throughput in standard-bore LC, its use in nano LC is mainly aimed at improving separation efficiency through the use of longer nano-LC columns packed with 2-μm (or smaller) particles [53].

Further miniaturisation of standard UHPLC instrumentation is possible [50]. Microfluidics has proven a great success as an alternate approach to achieve analytical separations [48]. Such downsizing of the LC experiment would undoubtedly require a major redesign in the column and instrumentation [51, 54]. The use of miniaturised instruments would result in a significant solvent, bench-space, and sample savings, and with mass spectrometry would allow even better interfacing [35, 53–55]. Chip-based LC systems have been extensively investigated, and a limited number of instruments have already been commercialised [55]. However, the adoption rate for commercial instruments has been somewhat slow and, compared to regular analytical columns, in microfluidics column efficiencies are not as high as expected [54]. The packing of microparticles within narrow channels is difficult, and one of the reasons for low column efficiency in microfluidics-based column systems [18, 35, 50–55].

7. Conclusion

Chromatographic technique development has always strived towards higher efficiency and more rapid resolution in diverse areas such as clinical, pharmaceutical and toxicology analysis, as well as enantioselective separation, to reduce costs and enhance throughput. Conventional HPLC, could not fully satisfy these requirements due to the relatively low efficiency and lengthy analysis time. Several approaches have been undertaken to achieve these goals, such as increasing flow rates and shortening the column length by using monolithic columns. However, these approaches may result in low phase ratio and low capacity factor. One promising approach is to use smaller size silica particle (less than 2 μm, as compared to conventional 3 and 5 μm size column packing materials. This is motivated by VDE that shows an inversely proportional relationship between the separation efficiency and particle size. Therefore, nano-or sub-micron size supporting materials may be promising to improve separation efficiency.

Abbreviations

CSP	chiral stationary phase
HETP	plate height
HPLC	high-performance liquid chromatography
i.d.	internal diameter

LC	liquid chromatography
Nano-LC	nano-liquid chromatography
PSD	particle size distribution
SP	stationary phase
UHPLC	ultra-high performance liquid chromatography
VDE	Van Deemter equation

Author details

Diana Ibrahim and Ashraf Ghanem*

*Address all correspondence to: ashraf.ghanem@canberra.edu.au

Chirality Program, School of Science, Faculty of Science and Technology, University of Canberra, Australia

References

[1] Beeram S, Rodrlguez E, Doddavenkatanna S, Li Z, Pekarek A, Peev D, Goerl K, Trovato G, Hofmann T, Hage D. Nanomaterials as stationary phases and supports in liquid chromatography. Electrophoresis. 2017;**38**:2498-2512. DOI: 10.1002/elps.201700168

[2] Nesterenko E, Nesterenko P, Connolly D, He X, Floris P, Duffy E, Paull B. Nano-particle modified stationary phases for high-performance liquid chromatography. The Analyst. 2013;**138**:4229. DOI: 10.1039/c3an00508a

[3] Sierra I, Perez-Quintanilla D, Morante S, Ganan J. Novel supports in chiral stationary phase development for liquid chromatography. Preparation, characterization and application of ordered mesoporous silica particles. Journal of Chromatography. A. 2014;**1363**:27-40. DOI: 10.1016/j.chroma.2014.06.063

[4] Sekhon S. Bhupinder, Enantioseparation of chiral drugs-an overview. Journal of ChemTech Research. 2010;**2**:1584-1594

[5] Fekete S, Veuthey J, Guillarme D. Comparison of the most recent chromatographic approaches applied for fast and high resolution separations: Theory and practice. Journal of Chromatography. 2015;**1408**:1-14. DOI: 10.1016/j.chroma.2015.07.014

[6] Zhi-Jian H et al. Chiral stationary phases and their relationship with enantiomer structures in Enanotioseparation research of analytical laboratory. Journal of the Mexican Chemical Society. 2014;**59**:43-49. DOI: 10.29356/jmcs.v59i1.13

[7] Qiu H, Liang X, Sun M, Jiang S. Development of silica-based stationary phases for high-performance liquid chromatography. Analytical and Bioanalytical Chemistry. 2011;**399**(10):3307-3322. DOI: 10.1007/s00216-010-4611-x

[8] Colwell L, Hartwick R. Non-porous silica supports for high performance liquid Chromatogrphy. Journal of Liquid Chromatography. 1987;**10**(12):2721-2744. DOI: 10.1080/01483918708066822

[9] Cheong W. Porous silica particles as chromatographic separation media: A review. Bulletin of the Korean Chemical Society. 2014;**35**(12):3465-3474. DOI: 10.5012/bkcs.2014.35.12.3465

[10] Barhate C, Wahab F, Breitbach Z, Bell D, Armstrong D. High efficiency, narrow particle size distribution, sub-2 μm based macrocyclic glycopeptide chiral stationary phases in HPLC and SFC. Analytica Chimica Acta. 2015;**898**:128-137. DOI: 10.1016/j.aca.2015.09.048

[11] Horvath K, Lukacs D, Sepsey A, Felinger A. Effect of particle size distribution on the separation efficiency in liquid chromatography. Journal of Chromatography. A. 2014;**1361**:203-208. DOI: 10.1016/j.chroma.2014.08.017

[12] Huang M et al. Preparation of silica microspheres with a broad pore size distribution and their use as the support for a coated cellulose derivative chiral stationary phase. Journal of Separation Science. 2017;**41**:1232-1239. DOI: 10.1002/jssc.201701215

[13] Qin Q, Zhang S, Zhang W, Zhang Z, Xiong Y, Guo Z, Fan J, Zheng S, Finlow D, Yin Y. The impact of silica gel pore and particle sizes on HPLC column efficiency and resolution for an immobilized, cyclodextrin-based, chiral stationary phase. Journal of Separation Science. 2010;**33**(17-18):2582-2589. DOI: 10.1002/jssc.200900831

[14] Nguyen D, Guillarme D, Rudaz S, Veuthey J. Fast analysis in liquid chromatography using small particle size and high pressure. Journal of Separation Science. 2006;**29**:1836-1848. DOI: 10.1002/jssc.200600189

[15] Majors R. HPLC and UHPLC Columns: Then, Now, Next, LCGC. 2018;**36**(2):128-131

[16] Kaczmarski K, Guiochon G. Modeling of the mass-transfer kinetics in chromatographic columns packed with Shell and Pellicular particles. Analytical Chemistry. 2007;**79**(12):4648-4656. DOI: 10.1021/ac070209w

[17] Wiest LA, Jensen DS, Hung CH, Oisen RE, Davis RC, Vail MA, Dadson AE, Nesterenko PN, Linford MR. Pellicular particles with spherical carbon cores and porous nanodiamond/polymer shells for reversed-phase HPLC. Analytical Chemistry. 2011;**83**(14):5488-5501. DOI: 10.1021/ac200436a

[18] Staub A, Zurlino D, Rudaz S, Veuthey J, Guillarme D. Analysis of peptides and proteins using sub-2 μm and sub-3-μm shell particles. Journal of Chromatography. A. 2011;**1218**:8903-8914. DOI: 10.1016/j.chroma.2011.07.051

[19] Durham D, Hurley T. Effect of sub-2-micron particle size on peak efficiency, capacity, and resolution in preparative liquid chromatography. Journal of Liquid Chromatography and Related Technologies. 2007;**30**:1895-1901. DOI: 10.1080/10826070701386462

[20] Fekete S, Ganzler K, Fekete J. Facts and myths about columns packed with sub-3 μm and sub-2 μm particles. Journal of Pharmaceutical and Biomedical Analysis. 2010;**51**(1):55-64. DOI: 10.1016/j.jpba.2009.08.003

[21] Olah E. Fekete S and J, Ganzler K, comparative study of new shell-type, sub-2 μm fully porous and monolith stationary phases, focusing on mass-transfer resistance. Journal of Chromatography. A. 2010;**1217**:3642-3653. DOI: 10.1016/j.chroma.2010.03.052

[22] Wang Y et al. Sub-2 μm porous silica materials for enhanced separation performance in liquid chromatography. Journal of Chromatography. A. 2012;**1228**:99-109. DOI: 10.1016/j.chroma.2011.08.085

[23] Wang Y, Ai F, Ng S, Tan T. Sub-2μm porous silica materials for enhanced separation performance in liquid chromatography. Journal of Chromatography. A. 2012;**1228**:99-109. DOI: 10.1016/j.chroma.2011.08.085

[24] Shaaban H, Gorecki T. Green ultra-fast high- performance liquid chromatographic method using a short narrow- bore column packed with fully porous sub-2 micron particles for the simultaneous determination of selected pharmaceuticals as surface water and wastewater pollutants. Journal of Chromatography. A. 2011;**1218**:252-261

[25] Fekete S, Fekete J, Ganzler K. Shell and small particles: Evaluation of new column technology. Journal of Pharmaceutical and Biomedical Analysis. 2009;**49**:64-71. DOI: 10.1016/j.jpba.2008.10.009

[26] Austin J. Ultra performance liquid chromatography(UPLC)-a review. Journal of Analytical and Pharmaceutical Chemistry. 2015;**2**:1056

[27] Fountain K, Neue U, Grumbach E, Diehl D. Effects of extra-column bacnd spreading, liquid chromatography system operating pressure, and column temperature on the performance of sub-2-μm porous particles. Journal of Chromatography. A. 2009;**1216**:5797-5988. DOI: 10.1016/j.chroma.2009.06.044

[28] DeStefano J, Langlois T, Kirkland J. Characteristics of superficially-porous silica particles for fast HPLC: Some performance comparisons with Sub-2-μm particles. Journal of Chromatographic Science. 2008;**46**(3):254-260. DOI: 10.1093/chromsci/46.3.254

[29] DeStefano J, Boyes B, Schuster S, Miles W, Kirkland J. Are Sub-2 μm particles best for separating small molecules? An alternative. Journal of Chromatography. A. 2014;**1368**:163-172. DOI: 10.1016/j.chroma.2014.09.078

[30] Chawla G, Ranjan C. Principle, instrumentation, and applications of UPLC: A novel technique of liquid chromatography. Open Chemistry Journal. 2016;**3**:1-16. DOI: 10.2174/1874842201603010001

[31] Carr P, Stoll D, Wang X. Perspectives on recent advances in the speed of high performance liquid chromatography. Analytical Chemistry. 2011;**83**(6):1890-1900. DOI: 10.1021/ac102570t

[32] Moody H. The evaluation of the parameters in the van Deemter equation. Journal of Chemical Education. 1982;**59**(4):290. DOI: 10.1021/ed059p290

[33] Gritti F, Guiochon G. The van Deemter equation: Assumptions, limits, and adjustment to modern high performance liquid chromatography. Journal of Chromatography. A. 2013;**1302**:1-13. DOI: 10.1016/j.chroma.2013.06.032

[34] Wren S, Tchelitcheff P. Use of ultra-performance liquid chromatography in pharmaceutical development. Journal of Chromatography. A. 2006;**1119**(1-2):140-146. DOI: 10.1016/j.chroma.2006.02.052

[35] Nazario C et al. Evolution in miniaturized column liquid chromatography instrumentation and applications: An overview. Journal of Chromatography. A. 2015;**1421**:18-37. DOI: 0.1016/j.chroma.2015.08.051

[36] Carr P, Wang X, Stoll D. The effect of pressure, particle size and time on optimizing performance in LC. Analytical Chemistry. 2009;**81**(13):5342-5353. DOI: 10.1021/ac9001244

[37] Calvet E, Bolsico C, Baeza-Baeza J, Celia M, Coque G. Description of the retention and peak profile for Chromolith columns in isocratic and gradient elution using mobile phase composition and flow rate as factors. Journal of Chromatography. 2014;**1**(4):194-210. DOI: 10.3390/chromatography1040194

[38] Guiochon G, Colin H. Chapter 1 Narrow-Bore and Micro-Bore Columns in Liquid Chromatography. Journal of Chromatography. 1984;**28**:1-38. DOI: 10.1016/S0301-4770(08)60692-2

[39] Ishii D, Asai K, Hibi K, Jonokuchi T, Nagaya M, A study of micro-high-performance liquid chromatography: I. Development of technique for miniaturization of high-performance liquid chromatography. Journal of Chromatography A. 1977;**144**(2):157-168. DOI: 10.1016/S0021-9673(00)99351-8

[40] Berger T. Demonstration of high speed with low pressure drops using 1.8 m particles in SFC. Chromatographia. 2010;**72**:597-602

[41] Perrenoud AG, Veuthey JL, Guillarme D. Comparison of ultra-high performance supercritical fluid chromatography and ultra-high performance liquid chromatography for the analysis of pharmaceutical compounds. Journal of Chromatography A. 2012;**1266**:158-167. DOI: 10.1016/j.chroma.2012.10.005

[42] Pauw R, Shoykhet K, Desmet G, Broeckhoven K. Understanding and minimizing the extra-column bandbroadening effects in supercritical fluid chromatography. Journal of Chromatography A. 2015;**1402**:132-137. DOI: 10.1016/j.chroma.2015.05.017

[43] Berger T. Preliminary kinetic evaluation of an immobilized polysaccharide sub-2 μm column using a low dispersion supercritical fluid chromatograph. Journal of Chromatography A. 2017;**1510**:82-88. DOI: 10.1016/j.chroma.2017.06.021

[44] Cancelliere G, Ciogli A, D'Acquarica I, Gasparrini F, Kocergin J, Misiti D, Pierini M, Ritchie H, Simone P, Vilani C. Transition from enantioselective high performance to

ultra-high performance liuid chromatography: A case study of a brush-type chrial stationary phase based on sub-5-micron to sub-2- micron silica particles. Journal of Chromatography A. 2010;**1217**(7):990-999. DOI: 10.1016/j.chroma.2009.10.021

[45] Chen Z, Agarwal A, Lambie B, Xu H, Yang Y, Zhang J, Weber SG. Speed and miniaturization improve separation and sensitivity. Trends in Analytical Chemistry. 2006;**25**(6):535-539. DOI: 10.1016/j.trac.2006.04.007

[46] Ghanem A, Wang C. Enantioseletive separation of racemates using CHIRALPAK IG amylose based chiral stationary phase under normal standard, non standard and reversed-phase high performance liquid chromatography. Journal of Chromatography. A. 2018;**1532**:89-97. DOI: 10.1016/j.chroma.2017.11.049

[47] Wang C, Ibrahim D, Ghanem A. Enantioselective separation of racemates using the sub-2 micron CHIRALPAK IG-U under normal standard, non-standard and reversed-phase high performance liquid chromatography. 2018 Manuscript accepted for publication with revision

[48] Nguyen D, Guillarme D, Rudaz S, Veuthey JL. Chromatographic behaviour and comparison of column packed with sub-2 μm stationary phases in liquid chromatography. Journal of Chromatography. A. 2006;**1128**:105-113. DOI: 10.1016/j.chroma.2006.06.069

[49] Wu N, Clausen A. Fundamental and practical aspects of ultrahigh pressure liquid chromatography for fast separations. Journal of Separation Science. 2007;**30**:1167-1182. DOI: 10.1002/jssc.200700026

[50] Fanali C, Fanali S. Chiral separations using miniaturized techniques: State of the art and perspectives. Journal of Chemistry. 2016;**56**:958-967. DOI: 10.1002/ijch.201600061

[51] Zhang Z, Wang Z, Liao Y, Huwei L. Applications of nanomaterials in liquid chromatography: Opportunities for separation with high efficiency and selectivity. Journal of Separation Science. 2006;**29**:1872-1878. DOI: 10.1002/jssc.200600154

[52] Sestak J, Moravcova D, Khale V. Instrument platforms for nano liquid chromatography. Journal of Chromatography. A. 2015;**1421**:2-17. DOI: 10.1016/j.chroma.2015.07.090

[53] Aturki Z et al. Current applications of miniaturized chromatographic and electrophoretic techniques in drug analysis. Journal of Pharmaceutical and Biomedical Analysis. 2014;**101**:194-220. DOI: 10.1016/j.jpba.2014.03.041

[54] Grinias J, Kresge G. Miniaturizing columns and Instrments in liquid Chormatography. LCGC. 2017;**35**(8):515-516

[55] Zotou A. An overview of recent advances in HPLC instrumentation. Central European Journal of Chemistry. 2012;**10**(3):554-569. DOI: 10.2478/s11532-011-0161-0

Polymeric Micro- and Nanosystems for Wood Artifacts Preservation

Rodica-Mariana Ion, Ramona-Marina Grigorescu,
Lorena Iancu, Paul Ghioca and Nicoleta Radu

Additional information is available at the end of the chapter

Abstract

The complex methods of diagnosis investigation of the wood artifacts state and proper materials for their protection against decay are very important goals in cultural heritage. This chapter focuses on the recent trends in micro- and nanostructured polymer systems for application in cultural heritage and on wood preservation, especially. The synthesis, properties, and applications, as well as the relevant analysis techniques to reveal the structures and properties of polymer systems, are discussed, too. To overcome the specific problems that exist for wood artifacts, some aspects should be treated: effects of the environmental factors, as moisture and pollutant absorption into the wood fibers, over-exposure effect of sun or artificial light sources, biological attack of different microorganisms, and the effects of the protective and decorative coatings.

Keywords: polymers, nanoparticles, PEG, SEBS, ZnO

1. Introduction

The conservation of cultural heritage is essential for humanity in order to preserve the cultural background of a people. Under this context, since most often old wooden objects present serious biological or chemical degradation which affects more or less the structural integrity, the mechanical resistance of the wooden material and their level of the authenticity are reduced [1, 2]. As a natural polymer, wood is composed of cellulose, hemicellulose (rich in free hydroxyl groups, being able to contribute to the hygroscopicity of wood), and

lignin (hydrophobic heteropolymer). The delignification will weaken the water resistance capacity of wood. By heating, the hygroscopicity, moisture uptake rate, and sorption hysteresis will be reduced, due to hemicellulose degradation [3].

Also, wood is an environmentally friendly material, a structural organic tissue, which consists of cellulose fibers embedded in a lignin matrix together with some minor components: terpenoids, resin and fatty acids, pectin, proteins, and inorganics [4].

Wood is hydrophilic; the physico-mechanical properties decrease with increasing the relative humidity below the saturation point, and the surface degradation is accelerated in weathering conditions. Wood quality is mainly influenced by the following external factors: high humidity and oxygen presence, (micro)biological organisms such as fungi, molds, insects, temperature, and electromagnetic radiation (UV, IR, high-energy β or γ, and so forth) [5].

Taking into account these principles, the traditional conservation-restoration methods that in some cases can produce irreversible effects on wooden objects over time have been replaced with modern procedures due to the intensive development of nanotechnologies [6]. The wood protection with micro- and nanopolymeric systems exceeds the disadvantage of multilayer coatings that could affect the optical properties and the surface quality and also reduce the water vapor transmission rate (WVTR) [7].

The degradation induced by UV light represents the main drawback and induces the organic compound decomposition due to the increase in photon's energy that breaks the chemical bonds. An inefficient polymer coating can lead to loss in mechanical properties and integrity of the matrix and wood discoloration due to lignin degradation. New composite materials were developed, as aromatic impregnating agents (insecticides or fungicides) such as creosote, halogenated carbamates, benzothiazoles, pentachlorophenol, (alkyl) imidazoles, bis (tributyltin) oxide, or salt-based impregnates such as borates, quinolinolates, naphthenates of copper, zinc or chromated copper arsenate-based preservatives (CCA) in several commercial variants and so forth [8–10], fluoroalkyl functional oligomeric silane system [11], short-chain amino silicones [12], alkoxysilanes with different organic groups [R'Si(OR")] [13], zinc oxide (ZnO) nanoparticles dispersed in maleic anhydride-modified polypropylene (MAPP) [14], and titanium dioxide (TiO$_2$) nanoparticles [15–19].

During the last decades, an intensification of historical wood artifacts preservation researches has intensified, and the new materials should present reversibility, must be compatible with all the materials encapsulated by the object, must not leech from wood, must be ecologic and biodegradable, and the "artistic" materials are to be treated as a whole [20]. Nanotechnology may provide interesting alternatives to develop new and efficient wood treatments to overcome technologies less feasibly used in the past decades to improve wood properties like heat treatment, chemical modification and impregnation, methods that can expand the dimensional stability, and resistance against microorganism [16]. Due to their very small dimensions (less than 100 nm), the nanomaterials have new properties, especially improved chemical reactivity and high mechanical properties. The nanostructures confer hardness and high wear resistance to the protected wood artifacts in some measure due to the increased density of the material [21, 22].

2. Conservation of the recovered marine shipwrecks

The unanimously used method of conserving the marine shipwrecks consisted of water replacing from the wooden material with polyethylene glycol (PEG), obviating the uncontrolled dehydration that would cause drastic damage of artifacts by fracturing the fragile wood cells [21, 23–25]. In such preserved shipwrecks, an accumulation of sulfur and iron compounds was observed, leading to the acidity increase which facilitates the cellulose depolymerization by the destruction of cellular wood walls and residual lignin degradation [23, 26, 27]. The increase of the system acidity can also produce PEG degradation into acidic byproducts that can act as ionic transporters [28–30]. For the preservation of these shipwrecks, the wood deacidification by using neutralizing alkaline compounds was required. The studies established that the maximal effect of acidity neutralization of archeological wood is achieved with nanodispersed alkaline hydroxides (20–150 nm) in alcoholic or PEG solutions, the most used being Na and Mg hydroxide. The alkaline nanoparticles dispersed into the polymer solution (low-molecular weight PEG: 200–2000 g/mol) deeply penetrate the degraded cellulosic cells, completely neutralizing the acids resulted from the wood degradation and further inhibiting the cellulose hydrolysis [21, 31, 32]. The deposition of calcium and magnesium hydroxide nanoparticles in the wood wall cells inhibits the oxidation of wood, thus increasing the conservation degree of the shipwrecks [22].

3. Historical wood artifacts conservation

The historical wood artifacts show different degrees of chemical and biological degradation that weakens the material resistance, and their physical and structural consolidation is essential in preserving these objects. The use of polymeric resins, which must have a good compatibility with the wood material and a high stability to environmental degradation, has an important contribution in the old wood objects consolidation [33–36]. The consolidation effect of the polymer resins is significantly improved by the nanodispersion in these solutions of mineral materials with reinforcing effect (especially metal oxides) [37]. The nanoinsertions of these nanocomposites into the wood support, besides the role of physical consolidation, also provide an important increase in resistance to oxidative and biological degradation (fungus mildew) and increased flame retardancy [38–41]. The most suitable polymers for wood preservation are aliphatic and aliphatic epoxy acrylic resins due to their stability to oxidative degradation, their adhesion, and processability. The most intensely used polymers for the preservation of modern and archaic wood articles are the polyacrylates, the low-molecular weight ethyl acrylate (Paraloid B 72) a metallic copolymer, recently used as composites with nanometric materials, being representative [42, 43]. The most used nanocomposites of polymeric resins are obtained with metal oxide nanoinsertions mainly ZnO, MgO, TiO_2 and metals Cu, Au and Ag [44–47].

4. Study case

Under such context, poly(styrene-ethylene-butylene-styrene) has the advantage of being able to be used as the base material for polymer films on the one hand and the advantage of high

stability, good mechanical properties, and resistance to biological attack. Also, its composite with ZnO increases the efficacy of this polymer. ZnO has been reported as a substance that provides an increased wood stability against degradation due to UV radiation because ZnO has the ability to block UV rays, both UVA and UVB, acting as physical filters that reflect or disperse UV radiation.

For the polymeric composition, poly(styrene-ethylene-butylene-styrene) block copolymer (SEBS) grafted with maleic anhydride (MA), mixed with ZnO, has been used for the preservation of wood surfaces by spraying the pretreated wood surfaces. A slight color change could be observed at the fir wood treated with SEBS-MA sample, because the consolidant retention, the penetration depth, and the uniformity of the consolidant distribution into the material are parameters that influence the consolidation effectiveness.

The protective behavior of these polymers on these samples was put into evidence by specific analytical techniques: Fourier-transform infrared spectroscopy (FTIR), chromatic analysis, and gloss index analysis [48–51].

The first change that indicates the wood degradation is identified by lignin degradation, through quinone compounds formed responsible for a yellowed surface. These compounds increase the surface roughness, the chemical bonds are weaker, and macroscopic cracks are formed [52]. The treatment of wood with different consolidants causes the alteration of the spectra aspect by the appearance or intensification of some characteristic absorption bands.

The temperature aging is characteristic to a reduction in hydroxyl groups, an increase of the unconjugated carbonyl groups, and an apparent slight increase of lignin. The different behavior of the studied wood species may be explained by their different chemical composition, especially hemicelluloses, lignin, and extractives content.

The color parameters that can indicate the wood change are L^* (degree of color lightness), a^* (green-red chromatic coordinate), b^* (blue-yellow chromatic coordinate), and ΔE (color variation and stability) that can be calculated using Eq. (1)

$$\Delta E = \sqrt{(\Delta L^*)^2 + (\Delta a^*)^2 + (\Delta b^*)^2} \tag{1}$$

where ΔE^*, Δa^*, and Δb^* are the differences between the sample specimens and the reference specimen; ΔL^* is the change of the light in the point, on different time intervals, compared with the initial value: $\Delta L^* = L_1^* - L_{initial}^*$; Δa^* is the chromatic deviation of the a^* coordinates (red and green colors) of the same point, on different time intervals, compared to the initial value: $\Delta a^* = \Delta L^* = a_1^* - a_{initial}^*$; Δb^* is the chromatic deviation of the b^* coordinates (yellow and blue colors), respecting the same mathematic formula: $\Delta b^* = b_1^* - b_{initial}^*$ [53].

ΔE^* value is an evaluation criterion of the overall change color. If the value is smaller than 0.2, the difference is not visible. A small difference in color is given by a value between 0.2 and 2. Between 2 and 3, respectively, between 3 and 6 highlight a color change visible with high-quality, respectively, a medium-quality filter. At a value over 6 of ΔE^*, the color is highly changed or even different [54].

The positive values of Δa^* after 120 h of irradiation indicate a tendency of both wood surfaces to become reddish. But when the exposure time increases, the values of Δa^* become negative, which is associated with a tendency of both wood surfaces to become greenish. Lignin degradation leads to chromophoric groups formation, carbonyl, and carboxyl groups, which affect the color change mechanism [55]. The process of lignin degradation is accentuated by oxygen and moisture presence, decreasing the coating adhesion due to low-molecular degradation products. In these conditions, an efficient coating must respect more requirements, namely enough filter efficiency until 440 nm, oxygen barrier, water vapor permeation, and abrasion, scratch and impact resistance [56].

The color changes in time can be highlighted by the chromatic variations, namely ΔL^*—variation of lightness and Δb^*—variation of the blue-yellow chromatic coordinates. In [56], the authors presented these variations of acrylic-ZnO coating for wood. ΔL^* increase from −20.09 for the wood sample to −5.66 for the sample of impregnated wood with 4% ZnO, Δb^*, the coordinate that marks the wood yellowness after UV exposure, a decrease from 15.27 until 0.99 after impregnation with the UV absorber (**Figure 1**).

Under such context, the gloss parameters could reflect the polymer quality, by irradiation, a small decrease is observed, most probably due to the polymer degradation, faster for SEBS-MA than SEBS-MA + ZnO (**Figure 2**).

Auclair et al. concluded during their study [57] that ZnO is a more efficient photo-protector for wood than CuO. As polymer matrix, urethane-acrylate systems were used. In case of polymer-ZnO nanocomposites, the discoloration of clear-coated wood exposed outdoors was reduced and the higher increase in gloss was obtained.

The photo-yellowing and UV degradation of wood surfaces were overcome by coating with ZnO-maleic anhydride-modified polypropylene (MAPP)-polyurethane transparent
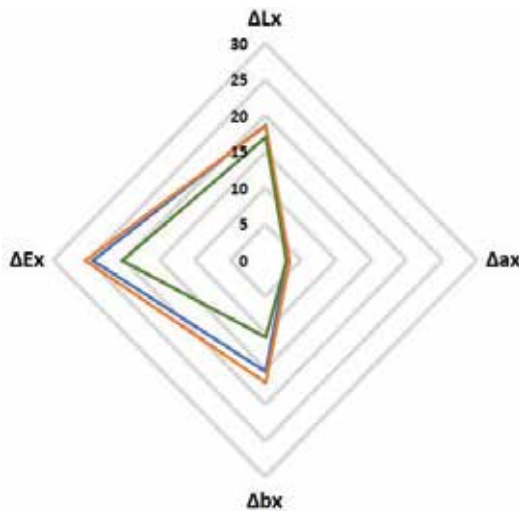

Figure 1. Chromatic parameters of fir wood samples after irradiation (60 min).
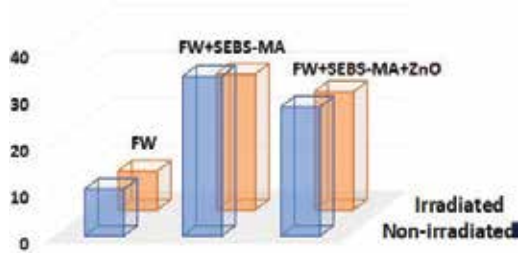
Figure 2. Gloss parameter of fir wood samples under different conditions.

nanosystems [14]. The acid anhydride groups of MAPP ensure the compatibility with OH groups from wood.

FTIR analysis can be used for solid wood samples being a fast-spectroscopic method and requiring an easy sample preparation. Information regarding the wood degradation can be obtained based on composition, functional groups, and molecular structure [52, 58, 59]. The degradation mechanism depending on the wood chemical composition (hemicellulose, lignin, and extractives content) is reflected in the chemical changes regarding the reduction of OH groups, increasing of unconjugated carbonyl groups, and formation of aromatic carbonyl conjugated groups as quinoid structures [60] (**Table 1**) (**Figure 3**).

Using polymeric micro- or nanosystems, the moisture content decreases. Humidity along with density is the physical factor that influences the physical, mechanical, and dimensional properties of wood and also influences the wood structure degradation. According to ISO 13061-1 [61] and Eq. (2), the moisture content is calculated for both native and treated wood:

$$w = \frac{m_w - m_0{}^*}{m_0} \, 100 \qquad (2)$$

where w is the moisture content [%], m_w is the sample weight measured at a certain moisture [kg], and m_0 is the weight of the sample oven-dried [kg].

As the humidity increases in the wood cell membranes, most of the mechanical properties of wood decrease, except for elasticity which increases. In the saturated air, the steady-state humidity will reach a maximum, which is precisely the same saturation humidity (the saturation point of the fiber). At this point, the sorption stops as a phenomenon of wood hygroscopicity, and the desorption begins if the external environment conditions change. Because relative air humidity is a function of temperature and humidity pressure, it results that the equilibrium humidity is directly dependent on relative humidity and temperature and, depending on them, there is a whole range of equilibrium humidities. Curves describing the evolution of sorption and desorption processes of water are not overlap, leading to the hysteresis area. Hysteresis indicates less water retention of dried capillaries as compared to those of the membrane in the wet state, due to the fact that the cell membranes suffer some deformations remaining during sorption. Hysteresis has a special role in drying and steaming wood as well as explaining the internal tensions. Water repellency can be improved by coating with natural wax [62], paraffin wax [63], palm oil [64], and esterified organosolv lignin [65].

Main absorption bands, cm^{-1}	Peak assignment [58]
3300	Stretching of —OH groups
2895	C—H aliphatic
1730–1740	Stretching of carbonyl group
1638	Bending of water (the moisture content)
1596 and 1512	Lignin aromatic ring
1423	Asymmetric C—H deformation
1364–1375	Symmetric bending of methyl groups in lignin and hemicellulose, bending of hydroxyl groups of polysaccharides
1157	Symmetric stretching of bridging oxygen
1025–1029	C—O in cellulose pyranose ring
898	Cellulose
809 and 670	Aromatic C—H from lignin

Table 1. Main FTIR absorption bands of wood.
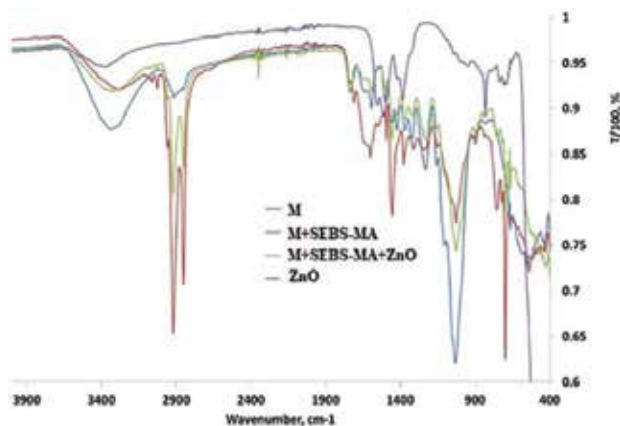
Figure 3. FTIR spectra of fir wood samples.

ZnO is a suitable component for UV protection in coatings. Dispersion in acrylic polymers leads to a reduced yellowing and improved optical properties after artificially weathering for up to 1500 h [56]. Shellac nanosystems were studied in [66] as wood coating and different property modifications were observed using various nanofillers. For shellac-ZnO systems, the inhibition or the slowing down of the UV degradation was obtained. ZrO$_2$ ensures an increased coating hardness. In both cases, the color, film-forming ability, water repellence, and adhesion were preserved.

UV-waterborne polyurethane containing different nanoparticles in order to increase the wood coating was studied. Thus, alumina, silica, ZnO, and CuO were used [7, 67]. The PU coating glass transition temperature is enhanced using alumina and silica that decrease the chains mobility at nanoparticles interface. The water and UV barrier properties are also increased. ZnO ensures a good photo-protection and clear-coated wood.

The coatings without nanoparticles in their composition present photo-yellowing and wood surface degradation when exposed to UV light. Dispersion of ZnO nanoparticles in MAPP and PU coatings restricted the color changes and photodegradation of wood polymers [14].

TiO_2 nanoparticles can impart hydrophobic or hydrophilic properties to the material, fungicidal, and bactericidal protection and present photo-catalytic activity. Using TiO_2 as coating for wood items ensures anisotropy, wettability, and UV protection [46, 68–71].

Zanatta et al. obtained the nanoparticles by a hydrothermal method using microwaves, and then the wood pretreated with chromated copper borate was coated with TiO_2. The wood maintained the natural color and the fungi resistance was improved [15].

The improvement of UV resistance using anatase TiO_2 was demonstrated in [17] when micro- and nanoparticles were impregnated on acacia hybrid wood. The exposure of the treated wood at UV radiation 960 h did not lead to color changes.

Obtaining stable and uniform dispersed coating is an effectiveness indicator. Polypropylene glycol can be considered a good solvent for metal oxides (ZnO, CeO_2 and TiO_2) nanoparticles films. An increased UV resistance and thus a decrease in lignin degradation were observed [72] (**Figures 4–6**).

TiO_2 coatings are a good moisture barrier for wood. If the treated wood is exposed to a 20–60% relative humidity (RH), the weight maintained constant, and at an RH between 60 and 90%, the mass increased with only 6%. TiO_2 coatings drastically decreased the change in anisotropic swelling of wood [19]. Obtaining films with controlled physico-chemical characteristics broadens their field of application. TiO_2 films may have different morphologies and wettability depending on the precursor pH (1–14). This characteristic may be a great advantage in using the nanoparticles coatings in various humidity environments [16].

Impregnation with micronized copper quaternary (MCQ) and UV absorbing acrylic resin (UVA-acrylic) was found to be a good method to increase the wood resistance to weathering conditions, and good visual, physical, and chemical properties were obtained [73].
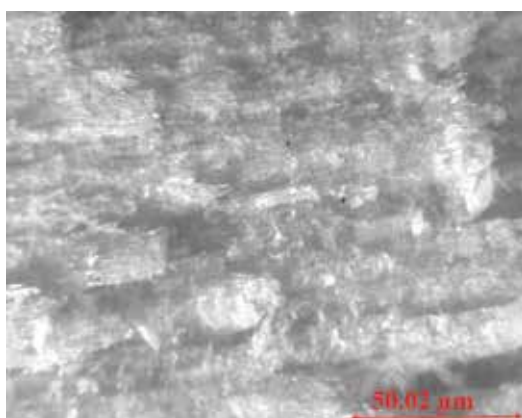
Figure 4. The fracture of the polymeric film from fir wood.
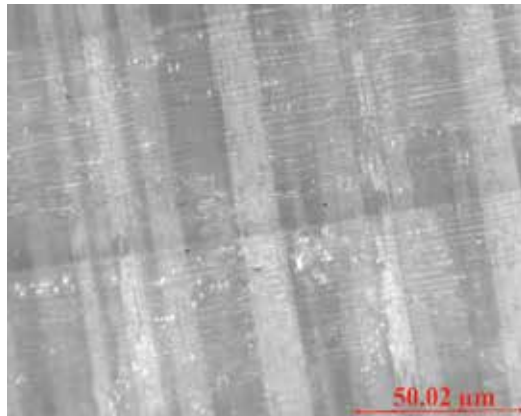
Figure 5. The fracture of the polymeric film from fir wood + SEBS-MA.
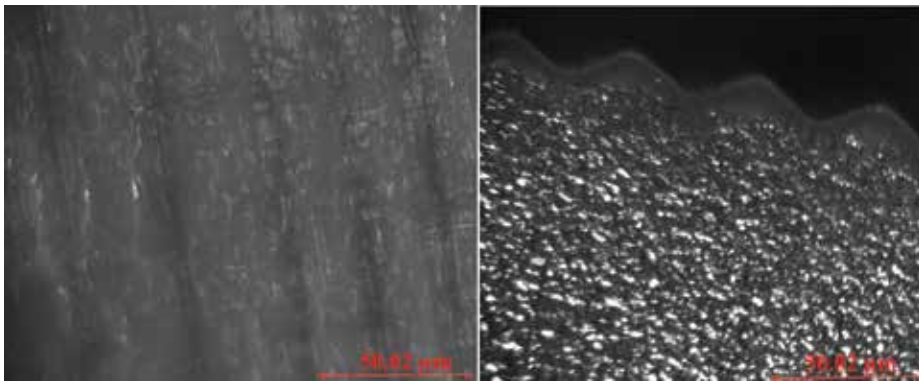
Figure 6. The fracture of the polymeric film from fir wood + SEBS-MA + ZnO.

Nkeuwa et al. [7] studied the behavior of UV-cured multilayer coatings where only the top coat consists of a nanoparticle—nanoclay with the RH variation. The color and gloss of initial, during, and after accelerated aging coatings were investigated. The color of coated samples does not present visual changes during and after aging. The studied color parameters (ΔL^*, Δa^*, Δb^*, and ΔE^*) increase with increasing RH while the gloss retention is lowered. At high RH, significant changes are observed.

Other additives used for wood protection are the fire retardants (FR). A good flame retardancy can be obtained using phosphorous, boron, and silicone. Phosphorous FR can exhibit both condensed and/or gas phase action and can generate less toxic gases and smoke during combustion [74]. Systems containing both phosphorous and nitrogen components are good substitutes for halogenated FR due to their synergistic effect [38, 39]. In [40], nitrogen-phosphorous FR dispersed in poly(sodium silicate-aluminum dihydrogen phosphate) (PSADP) was used to reduce poplar wood hygroscopicity and to improve its fire resistance. These two components present a synergic effect on the two properties being distributed over the inner surface and penetrate the cell cavities of wood.

5. Microbial degradation of wood

The degradation of wood materials depends on physico-chemical and biological factors such as temperature, humidity, nutrients, and the type of wood (hardwood or softwood), specific to the environment in which they are exposed. Among the biological factors, insects, macro- and micromycetes, and bacteria, the microbial load of the environment, corroborated with humidity and temperature, plays an important role in the biodegradation processes of this material. Of the microbiological agents, the most common types of biodegradation are those caused by fungi and bacteria, which manage to degrade the wood through enzymatic mechanisms with the enzymes they are secreting. The fungi types that attack wood materials are divided into three classes:

1. White-root fungi can degrade all cellular components by using nonspecific enzymes that they secrete, but in a first stage, they degrade the lignin using hemicellulose as a carbon source. Following the degradation with these types of fungi, the attacked surfaces get a whitish appearance [75]. This class includes macromycetes such as *Phanerochaete chrysosporium* (*Sporotrichum pulverulentum*), *Phanerochaete sordida*, *Phlebia radiata*, and *Phlebia tremellosa* [76] which is able to degrade wood lignin to CO_2 and water.

2. Brown-root fungi generally degrade cellulose and hemicellulose from wood, but they also degrade lignin. The mechanisms used by brown rot fungi in the biodegradation of wood are both enzymatic and non-enzymatic. These micromycetes do not produce lignin degradation enzymes but have a mechanism that results in lignin modification and slow reduction of lignin content in the attacked wood. This class includes macromycete species as *Serpula lacrymans*, *Postia placenta*, *Gloeophyllum trabeum, and Tyromyces palustris*. Surfaces attacked by fungi of this class get a brownish look [77]. Studies on wood sample of *Pinus sylvestris* and *Populus euramericana* showed that after vacuum treatment with inorganic or organic preservatives, which contain Cr^{6+}, Cu^{2+}, As^{5+}, organic salts of ammonia and N-alkylbenzyldimethylammonium chloride, inoculated with macromycetes from the species *S. lacrymans 1*, *S. lacrymans 2*, *P. placenta*, *G. trabeum, and T. palustris*, reveal a substantial reduction in wood loss due to the inhibition of the biological activity of the macromycetes tested [77].

3. Soft root fungi, or micromycetes, from which the most popular are *Penicillium chrysogenum* and *Aspergillus niger*, perform deterioration from edge to center of wood. In a study of wood artifacts from Islamic Art Museum, the Grand Egyptian Museum and Saqqara necropolis [78], two species of of the genus *Alternaria*, 15 species of *Aspergillus*, three species of the genus *Cladosporium*, six species of *Penicillium*, two species of *Trichophyton*, along with species of the genus *Cladosporium*, *Chaetomium*, *Phoma*, *Stemphylium*, *Ulocladium*, and *Syncephalastrum*, were found most of them with cellulolytic enzymatic activity, able to degrade the wood [78]. Their frequency on the analyzed artifacts was between 7.1 and 35.7%; the most common fungal species being (**Figure 7**) *Aspergillus. brasiliensis*, *Aspergillus flavus* var. columnaris, *Penicillium* sp.2, *Aspergillus parasiticus*, *Aspergillus terreus*, *Aspergillus versicolor*, *Cladosporium* sp.1, *and Penicillium* sp.3, the rest being encountered at a frequency of 7.1% [78].

In vitro tests performed in order to establish the biological action of three types of inorganic nanomaterials with Ag, Ti, and Cu (AgNPs, CuNPs, TiNPs) on fungi and bacteria (*Bacillus alvei, Short Bacilli, Bacilli Spore Former, Aspergillus niger, Aspergillus flavus, Aspergillus fumigatus*)

isolated from funerary masks of degraded wood from Saqqara showed that the most effective of the tested materials is AgNPs, followed by CuNPs and TiNPs [79], both for fungi and bacteria (**Figures 8** and **9**). The action mechanism of AgNP includes processes such as adherence to microbial cells, penetration into cells, free radical generation, DNA and RNA damage [79, 80].

Another study performed on China's degraded wood objects [81] found in the Dingtao King Mausoleum during the Dynasty West Dynasty (206 BC-25 AC) revealed a massive degradation of the wooden objects. Determinations have shown that the degradation is caused by fungi. DNA sequencing of isolated fungi showed that there are 114 genres of fungi. However, in all samples, the most abundant genus was *Hypochnicium* sp., which represent 98.61–99.45% of the total of the fungal community.

Wood objects exhibited in museums are subject to deterioration of biological agents. The wood Jesuit sculptures from South America exposed at the Museum of Natural Sciences of La Plata, Buenos Aires Argentina, are subject to the biodegradation [82]. Determinations made on a strip of degraded wood of the *Cedrela fissilis* species led to the identification of two fungi species*: Nigrospora sphaerica* and *Chaetomium globosum. Chaetomium* is a recognized macromycete for its ability to destroy wood, but for *Nigrospora sphaerica*, very few things are

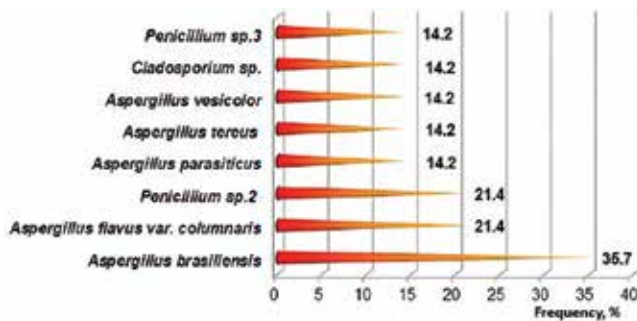**Figure 7.** Fungal species frequency (%) (micromycetes) identified on biodeteriorated wood artifacts, from Islamic Art Museum, Saqqara necropolis, Grand Egyptian Museum, Cheops Solar Boat [78].
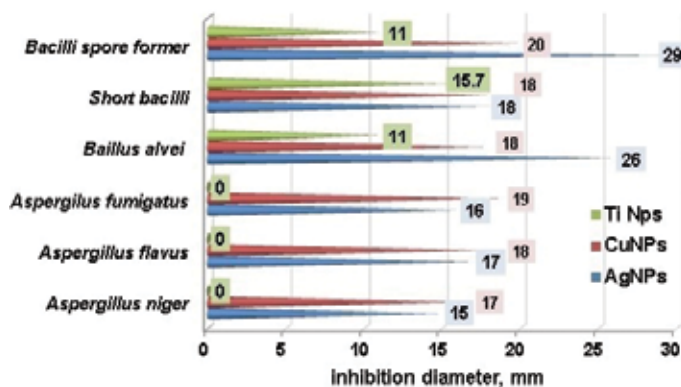

Figure 8. Effect of inorganic nanomaterial with AgNPs, CuNPs, TiNPs, on some fungal and bacterial strain isolated from wood artifacts from Saqqara necropole. Concentration of nanoproduct applied: = 10 μg/mL [79].

Figure 9. Effect of inorganic nanomaterial with AgNPs, CuNPs, TiNPs, on some fungal and bacterial strain isolated from wood artifacts from Saqqara necropole. Concentration of nanoproduct applied: = 15 µg/mL [79].
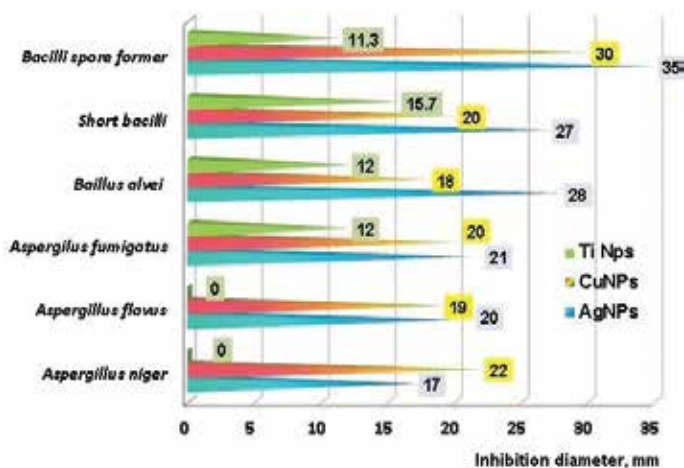
known regarding its effects on wood [82]. Bacteria are another class of biological agents that can affect the structure of the wood. Thus, in studies conducted to find an optimal method of disinfection and protection of wood surfaces in the historical area of Auschwitz-Birkenau II, bacterial species such as *Pseudomonas fluorescens*, *Staphylococcus equorum*, and *Bacillus cereus* have been isolated from this site. In terms of fungi, the following species have been identified on the wood surfaces: *Alternaria alternata*, *Chaetomium globosum*, *Cladosporium cladosporioides*, *Engyodontium album*, and *Penicillium citreonigrum*.

In vivo tests, made on new pieces of white poplar wood, previously sterilized and treated with a mixture of cultures of bacteria and/or fungi, were aimed at the evaluation of the number of living microorganisms on the surfaces (bacteria) and the estimation of the percentage from the wood surface altered by fungal activity, as well as the changes in color and luminance of the treated samples. The study reveals that the best commercially available biocidal products are B, ABM-1, and R 101 (**Figure 10**) (product B containing 24% benzyl alkyl (C12–16) dimethyl-ammonium chlorides, 5% boric acid ABM-1 contains N-3-aminopropyl-1,3-propanediamine, N,N-dialkyl (C10–C16)-N-methyl N-polyoxyethylene ammonium propionate, N,N-dialkyl (C10–C14) [3-dodecanoylamino)] propyl dimethyl ammonium acetate; product R101 contains 40–60% N,N-dodecyl-N,N-dimethylammonium chloride and 20–25% isopropanol). The best results were obtained for product R101, followed by AM-1, applied by spray or fogging exposure. The color (ΔE) and luminance (ΔL) tests showed that for the treatments chosen, no remarkable differences compared to the untreated control were observed (**Figure 11**). In another study, the effects of some aqueous dispersions of silver or zinc nanoparticles (AgNPs, ZnNPs) to air and liquid permeability of *Paulownia* wood samples exposed to *Trametes versicolor* were assessed [83]. The wood samples were heat treated at 100 and 150°C, after which they were exposed to *T. versicolor*. Permeability values were measured before and after exposure to fungal activity. The results obtained showed significant decreases in permeability in all treatments after exposure to fungi (**Figure 12**). The permeability difference was related to the growth and accumulation of fungal hyphae along the lumen vessels, which block the fluid transfer. The best results were obtained by heat treatment at 150°C, followed by impregnation
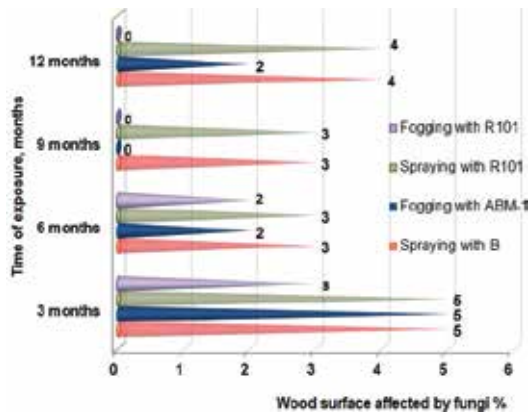
Figure 10. Biocidal effect of some commercial products on the wood samples inoculated with fungal strains, by spraying or fogging [84].
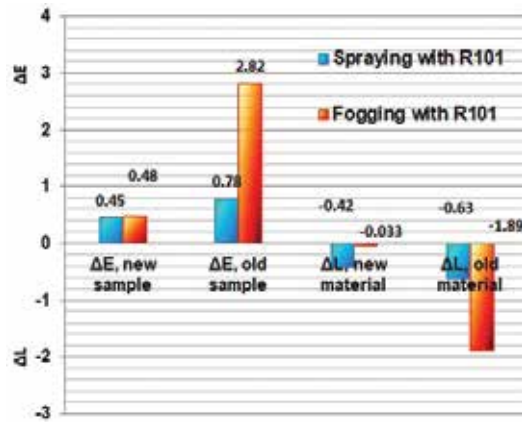
Figure 11. The color and luminance difference of wood samples after biocidic product applications. ΔE = difference of color; ΔL = difference of luminance [84].
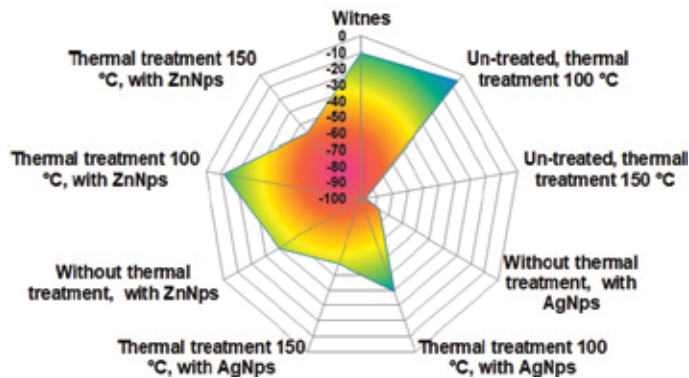
Figure 12. Specific air permeability in wood samples treated with ZnNps and/or AgNps nanomaterials after exposure to action of rot-white fungus *Trametes versicolor* [83].

with ZnNps or AgNps which significantly inhibited the growth of the microorganism, reducing the mass loss of impregnated wood samples subjected to fungal attack [83].

Regarding methods of treatment against wood degradation, there are currently several methods of protection against decomposition caused by biological agents. From these, organic compounds based on quaternary ammonium salts were the most used. Studies conducted to determine the antimicrobial activity of three biocides against *Pseudomonas fluorescens*, *Staphylococcus equorum*, *Bacillus cereus*, *Bacillus muralis*, *Sporosarcina aquimarina*, *Rhodococcus fascians*, and some fungi species such as *Chaetomium globosum*, *Penicillium citreonigrum*, *Cladosporium cladosporioides 1*, *Acremonium strictum*, *Aspergillus fumigatus* and *Cladosporium cladosporioides 2*, all isolated from wood or brick surfaces, showed that species such as *Staphylococcus equorum*, *Bacillus cereus*, *Sporosarcina aquimarina*, *Rhodococcus fascieni*, *Cladosporium cladosporioides*, and *Acremonium strictum* have a high susceptibility to quaternary ammonium biocides [85]. Thus, the wood objects with a historical value can be efficiently disinfected by three times application of a biocide (30% v/v) which contains dodecyl dimethyl ammonium chloride, citric acid, propiconazole, and propanol [85]. The mechanism of action of ammonium quaternary salts is based on the dissolution of certain sites from cell walls, which results in the loss of microbial cell integrity, followed by exposure of cell content and release of the material out of the cell, followed by degradation of proteins, of nucleic acids, and cell lysis, the latter caused by autolytic enzymes [85].

Protecting degradation of wood by biological agents can also be done without biocides based on quaternary ammonium salts. A wood protection variant is based on the application of a titanium isopropoxide gel and ammonium cerium nitrate as a stabilizer for wood treatment [86]. As a mechanism of action, it is assumed that the hydrolysis of titanium isopropoxide is initiated by the wood-based OH groups as well as by the moisture in the cellular wood wall resulting in a layer of cerium-doped TiO_2 which seals the wood surface and thus limiting the direct exposure of micro- or nanopores of wood to fungal hydrolytic enzymes. Studies conducted on Norway spruce have shown that this method can be protected against degradation by biological agents such as *Gloeophyllum trabeum*, *Rhodonia placenta*, and *Coniophora puteana*.

6. Conclusions

The maintaining of wood quality in time is usually achieved with the help of preservatives. These are individual chemical compounds or mixtures that make wood less susceptible to attack from a large variety of degradative factors or organisms. These organisms include insects, marine borers, and various types of fungi such as stain and decay. Some of these chemicals are effective against a wide range of organisms, while others are very specific and protect wood from only one type of organism.

Acknowledgements

Conflict of interest

The author(s) declared no potential conflicts of interest.

Author details

Rodica-Mariana Ion[1,2]*, Ramona-Marina Grigorescu[1], Lorena Iancu[1,2], Paul Ghioca[1] and
Nicoleta Radu[1]

*Address all correspondence to: rodica_ion2000@yahoo.co.uk

1 ICECHIM, Research Group "Evaluation and Conservation of Cultural Heritage",
Bucharest, Romania

2 Doctoral School of Materials Engineering, Valahia University, Targoviste, Romania

References

[1] Reinprecht L. Wood Deterioration, Protection and Maintenance. Wiley Online Library;
Chichester, West Sussx, UK. 2016. DOI: 10.1002/9781119106500

[2] Wörlea M, Hubert V, Hildbrand E, Hunger K, Lehmann E, Mayer I, Petrak G, Pracher
M, von Arx U, Wülfert S. Evaluation of decontamination methods of pesticide contami-
nated wooden objects in museum collections: Efficiency of the treatments and influence
on the wooden structure. Journal of Cultural Heritage. 2012;**13**:S209-S215. DOI: 10.1016/j.
culher.2012.01.006

[3] Salminen E, Valo R, Korhonen M, Jernlas R. Wood preservation with chemicals.
Copenhagen, Denmark: Best Available Techniques (BAT) Nordic Council of Ministers; 2014

[4] Ghetiu MM, Toporet V. Chimia Lemnului. Chisinau: Ed. Tehnica-Info; 2010. ISBN: 978-
99-75-63-310-9

[5] Clausen CA. Biodeterioration of Wood. Madison, Wisconsin: Forest Products Laboratory,
United States Department of Agriculture Forest Service; 2010

[6] Ion R-M, Doncea S-M, Ţurcanu-Caruţiu D. Nanotechnologies in Cultural Heritage—
Materials and Instruments for Diagnosis and Treatment. In: Kyzas G, editor. Novel
Nanomaterials. IntechOpen; 2018. pp. 173-190. DOI: 10.5772/intechopen.71950

[7] Nkeuwa WN, Riedl B, Landry V. Transparent UV-cured clay/UV-based nanocomposite
coatings on wood substrates: Surface roughness and effect of relative humidity on opti-
cal properties. Journal of Coatings Technology and Research. 2017;**14**(3):555-569. DOI:
10.1007/s11998-016-9873-6

[8] Nami Kartal S, Tenzi E, Yilmaz H, Goodell B. Bioremediation and decay of wood treated
with ACQ, microionized ACQ, nano-CuO and CCA wood preservatives. International
Biodeterioration & Biodegradation. 2015;**99**:95-101. DOI: 10.1016.j.ibiod.2015.01.004

[9]   Lin LD, Chen YF, Wang SY, Tsai MJ. Leachability, metal corrosion, and termite resistance of wood treated with copper-based preservative. International Biodeterioration & Biodegradation. 2099;**63**(4):533-538. DOI: 10.1016/j.ibiod.2008.07.012

[10] Cicardi C, Schwarze FWMR, Wick P. Microionized copper wood preservatives: An efficiency and potential health risk assessment for copper-based nanoparticles. Environmental Pollution. 2015;**200**:126-132. DOI: 10.1016/j.envpol.2015.02.018

[11] Hochmanska P, Krystofiak T, Mazela B. Hydrophobicity and weathering resistance of wood treated with silane-modified protective systems. Drewno. 2014;**57**(191):99-111. DOI: 10.12841/wood.1644-3985.060.07

[12] Ghosh SC, Militz H, Mai C. Modification of *Pinus sylvestris* L. wood with quat- and amino-silicones of different chain lengths. Holzforschung. 2013;**67**(4):421-427. DOI: 10.1515/hf-2012-0103

[13] Cappelletto E, Maggini S, Girardi F, Bochicchio G, Tessadri B, Di Maggio R. Wood surface protection with different alkoxysilanes: A hydrophobic barrier. Cellulose. 2013;**20**(6): 3131-3141. DOI: 10.1007/s10570-013-0038-9

[14] Salla J, Pandey KK, Srinivas K. Improvement of UV resistance of wood surfaces by using ZnO nanoparticles. Polymer Degradation and Stability. 2012;**97**(4):592-596. DOI: 10.1016/j.polymdegradstab. 2012.01.013

[15] Zanatta P, Lazarotto M, de Cademartori PHG, Cava SD, Moreira ML, Gatto DA. The effect of titanium dioxide nanoparticles obtained by microwave-assisted hydrothermal method on the color and decay resistance of pinewood. Maderas-Ciencia Y Tecnologia. 2017;**19**(4):495-506. DOI: 10.4067/s0718-221x2017005000901

[16] Gao LK, Zhan XX, Lu Y, Li J, Sun QF. pH-dependent structure and wettability of TiO_2-based wood surface. Materials Letters. 2015;**142**:217-220. DOI: 10.1016/j.matlet.2014.12.035

[17] Tuong VM, Chu TV. Improvement of color stability of acacia hybrid wood by TiO_2 nano sol impregnation. Bioresources. 2015;**10**(3):5417-5425

[18] Wang BL, Feng M, Zhan HB. Improvement of wood properties by impregnation with TiO_2 via ultrasonic-assisted sol-gel process. RSC Advances. 2014;**4**(99):56355-56360. DOI: 10.1039/c4ra04852k

[19] Sun Q, Yu H, Liu Y, Li J, Lu Y. Improvement of water resistance and dimensional stability of wood through titanium dioxide coating. Holzforschung. 2010;**64**:757-761. DOI: 10.1515/hf.2010.114

[20] Christensen M, Kutzke H, Hausen FK. New materials used for the consolidation of archaeological wood. Past, attemps, present struggles and future requirements. Journal of Cultural Heritage. 2012;**135**:S183-S190. DOI: 10.1016/j.culher.2012.02.013

[21] Baglioni P, Giorgi R, Dei L. Soft condensed matter for the conservation of cultural heritage. Comptes Rendus Chimie. 2009;**12**(1-2):61-69. DOI: 10.1016/j.crci.2008.05.017

[22] Hamed SAM. Possibilities application on nanoscience and nanotechnology in conservation of archaeological wood. A review. Journal of American Science. 2013;**6**(10):1186-1194

[23] Almkvist G, Persson I. Degradation of polyethylene glycol and hemicellulose in the vasa. Holtzforschung. 2008;**62**:64-70. DOI: 10.1515/hf.2008.009

[24] Almkvist G, Persson I. Fenton-induced degradation of polyethylene glycol and oak hemicellulose. A model experiment in comparison to change observed in conserved waterlogged wood. Holtzforschung. 2008;**62**:704-708. DOI: 10.1515/hf.2008.129

[25] Giauchi G, Capretti C, Macchioni N, Pizzo B, Donato ID. A methodological approach in the evaluation of the efficacy of treatments for the dimensional stabilization of water-logged archaeological wood. Journal of Cultural Heritage. 2010;**1**:91-101. DOI: 10.1016/j.culher.2009.04.003

[26] Almkvist G, Persson I. Analysis of acids and degradation products related to iron and sulfur in the swedish warship vasa. Holtzforschung. 2008;**62**:694-703. DOI: 10.1515/HF.2008.130

[27] Zoia L, Orlandi M, Tamburini D, Colombini MP. Chemical characterization of the whole plant cell wall in archaeological wood: An integrated approach. Analytical and Bioanalytical Chemistry. 2017;**409**(17):4233-4245. DOI: 10.1007/s00216-017-0378-7

[28] Lars E. Vasa—Recent preservation research. 11th ICOM-WOAM Conf.; Greeville, NC, USA. 2010

[29] Hocker E, Almkvist G, Sahlstedt M. The Vasa experience with polyethylene glycol: A conservator's perspective. Journal of Cultural Heritage. 2012;**13**(1):S175-S 182. DOI: 10.1016/j.culher.2012.01.017

[30] Gregory D, Jensen P, Strætkvern K. Conservation and in situ preservation of wooden shipwrecks from marine environments. Journal of Cultural Heritage. 2012;**13**:139-148. DOI: 10.1016/j.culher.2012.03.005

[31] Poggi G, Toccafondi N, Chelazzi D, Canton P, Giorgi R, Baglioni P. Calcium hydroxide nanoparticles from solvothermal reaction for the deacidification of degraded water-logged wood. Journal of Colloid and Interface Science. 2016;**473**:1-8. DOI: 10.1016/j.jcis.2016.03.038

[32] Giorgi R, Chelazzi D, Fratini E, Eanger S, Niklasson A, Rademar M, Svensson JE, Baglioni P. Nanoparticles of calcium hydroxide for wood deacidification. Decreasing the emission of organic acid vapor in church organ environments. Journal of Cultural Heritage. 2009;**10**:206-213. DOI: 10.1016/j.culher.2008.06.012

[33] Sassoni E. Hydroxyapatite and other calcium phosphates for the conservation of cultural heritage: A review. Materials. 2018;**11**(4):1-48. DOI: 10.3390/ma11040557

[34] Sakuno T, Schniewind AP. Adhesive qualities of consolidants for deteriorated wood. Journal of the American Institute for Conservation. 2013;**29**:33-44. DOI: 10.1179/019713-690806046127

[35] deSilva M, Henderson J. Sustainability in conservation practice. Journal of the Institute of Conservation. 2011;**34**:5-15. DOI: 10.1080/19455224.2011.566013

[36] Rogerio-Candelera MA, Lazzari M, Cano E. Science and Technology for the Conservation of Cultural Heritage. New York, USA: CRC Press; 2013

[37] Stankovic A, Dimitrevic S, Uskokovic D. Influence of size and morphology on bacterial properties of ZnO powder hydrothermally synthesized using different surface stabilizing agents. Colloid and Surfaces B: Biointerfaces. 2013;**102**:21-28. DOI: 10.1016/j.colsurfb.2012.07.033

[38] Chambhare SU, Yagtap R, Lockhande G. Design and UV-curable behaviour of boron based reactive diluent for epoxy acrylate oligomer used for flame retardant wood coating. Designed Monomers & Polymers. 2016;**20**(1):125-135. DOI: 10.1080/15685551.2016.123102

[39] Dasari A, Cai G, Yu Y-Y, Mai Y-W. Recent developments in the fire retardancy of polymeric materials. Progress in Polymer Science. 2013;**38**(9):1357-1387. DOI: 10.1016/j.progpolymsci.2013.06.006

[40] Zhang XT, Mu J, Chu DM, Zhao Y. Synthesis of fire retardants based on N and P and poly(sodium silicate-aluminum dihydrogen phosphate) (PSADP) and testing the flame-retardant properties of PSADP impregnated poplar wood. Holzforschung. 2016;**70**(4):341-350. DOI: 10.1515/hf-2014-0362

[41] Sow C, Riedl B, Blanchet P. UV-waterborne polyurethane-acrylate nanocomposite coatings containing alumina and silica nanoparticles for wood: Mechanical, optical, and thermal properties assessment. Journal of Coatings Technology and Research. 2011;**8**(2):211-221. DOI: 10.1007/s11998-010-9298-6

[42] Crisci GM, Malagodi M, La Russa MF, Ruffolo SA. Consolidating properties of Regalrez 1126 and Polaroid B72 applied to wood. Journal of Cultural Heritage. 2010;**11**:304-308. DOI: 10.1016/j.culher.2009.12.001

[43] Crisci GM, La Russa MF, Malagodi M, Ruffolo SA. The Effect of acrylic polymer Paraloid B72 used in conservation. Journal of Cultural Heritage. 2010;**11**:304-308

[44] Nami Kartal S, Clausen CA, Green F. Do the unique properties of nanometals affect leachability or efficacy against fungi and termites? International Biodeterioration & Biodegradation. 2009;**63**(4):490-495. DOI: 10.1016/j.ibiod.2009.01.007

[45] Dumitrescu I, Manciulea I. Nanocomposites materials based on polymers and alumina nanoparticles. Environmental Engineering and Management Journal. 2009;**8**(4):953-956

[46] Lu Y, Li J, Sun Q, Cui Y, Liu Y. Growth of TiO_2 coating on wood surface using controlled hydrothermal method at low temperatures. Applied Surface Science. 2010;**256**:5046-5050. DOI: 10.1016/j.apsusc.2010.03.053

[47] Pasquet J, Chevalier Y, Couval E, Bouvier D, Bolzinger M-A. Zinc oxide as a new antimicrobial preservative of topical products: Interactions with common formulation ingredients. International Journal of Pharmaceutics. 2015;**479**:88-95. DOI: 10.1016/j.ijpharm.2014.12.031

[48] Tolvaj L, Varga D, Papp G. Colour Measurement for Determining the Steaming Properties of Wood. Óbuda Univ. e-Bull. 2012:99-104

[49] JIS Z 8729. Colour Specification-CIELAB and CIELUV Colour Spaces. 4th ed. Japan: Japanese Standards Association (JSA); 2008

[50] Matsuo M, Yokoyama M, Umemura K, Gril J, Yano K, Kawai S. Color changes in wood during heating: Kinetic analysis by applying a time-temperature superposition method. Applied Physics A. 2010;**99**(1):47-52. DOI: 10.1007/s00339-010-5542-2

[51] Giuriani E, Cominelli S, Marini A, Gubana A. The penetration test to evaluate wood decay after 20 years timber structure assessment experience. Advanced Materials Research. 2013;**778**:201-208. DOI: 10.4028/www.scientific.net/AMR.778.201

[52] Timar MC, Varodi A, Hacibektasoglu M, Campean M. Color and FTIR analysis of chemical changes in beech wood (*Fagus sylvatica* L.) after light steaming and heat treatment in two different environments. BioResources. 2016;**11**(4):8325-8343. DOI: 10.15376/biores.11.4.8325-8343

[53] Schanda J. Colorimetry. Understanding the CIE System. Hoboken: New Jersey, Wiley-Interscience, John Wiley & Sons, Inc; 2007

[54] Barcik S, Gasparik M, Razumov EY. Effect of temperature on the color changes of wood during thermal modification. Cellulose Chemistry and Technology. 2015;**49**(9-10):789-798

[55] Yeniocak M, Goktas O, Colak M, Ozen E, Ugurlu M. Natural coloration of wood material by red beetroot (*Beta vulgaris*) and determination color stability under UV exposure. Maderas. Ciencia y Tecnología. 2015;**17**(4):711-722. DOI: 10.4067/S0718-221X201500-5000062

[56] Weichelt F, Beyer M, Emmler R, Flyunt R, Beuer E, Buchmeiser M. Zinc oxide based coatings for the UV-protection of wood for outdoor applications. In: Camino G, Frache A, Tabuani D, editors. Eurofillers. Weinheim: Wiley-VCH Verlag Gmbh; 2011. pp. 23-30. DOI: 10.1002/masy.201150304

[57] Auclair N, Riedl B, Blanchard V, Blanchet P. Improvement of photoprotection of wood coatings by using inorganic nanoparticles as ultraviolet absorbers. Forest Products Journal. 2011;**61**(1):20-27. DOI: 10.13073/0015-7473-61.1.20

[58] Timar MC. An investigation of consolidants penetration in wood. Part 2: FTIR spectroscopy. Pro Ligno. 2011;**7**(1):22-38

[59] Dobrica I, Bugheanu P, Stanculescu I, Ponta CFTIR. spectral data of wood used in Romanian traditional village constructions. Analele Universităţii din Bucureşti–Chimie. Anul XVII (serie nouă). 2008;**17**(I):33-37

[60] Xin YL, Timar MC, Varodi AM, Sawyer G. An investigation of accelerated temperature-induced ageing of four wood species: Colour and FTIR. Wood Science and Technology. 2016;**51**:357-378. DOI: 10.1007/s00226-016-0867-4

[61] ISO 13061-1: 2014 Physical and mechanical properties of wood—Test methods for small clear wood specimens—Part 1: Determination of moisture content for physical and mechanical tests

[62] Humar M, Kržišnik D, Lesar B, Thaler N, Ugovšek A, Zupančič K, Žlahtič M. Thermal modification of wax-impregnated wood to enhance its physical, mechanical and biological properties. Holzforschung. 2017;**71**(1):57-64. DOI: https://doi.org/10.1515/hf-2016-0063

[63] Wang W, Huang Y, Cao J, Zhu Y. Penetration and distribution of paraffin wax in wood of loblolly pine and Scots pine studied by time domain NMR spectroscopy. Holzforschung. 2018;**72**(2):125-131. DOI: 10.1515/hf-2017-0030

[64] Lee SH, Ashaari Z, Chen Lum W, Fei Ang A, Abdul Halip J, Halis R. Chemical, physico-mechanical properties and biological durability of rubberwood particle boards after post heat-treatment in palm oil. Holzforschung. 2018;**72**(2):159-167. DOI: https://doi.org/10.1515/hf-2017-0086

[65] Gordobil O, Herrera R, Llano-Ponte R, Labidi J. Esterified organosolv lignin as hydrophobic agent for use on wood products. Progress in Organic Coatings. 2017;**103**:143-151. DOI: 10.1016/j.porgcoat.2016.10.030

[66] Weththimuni ML, Capsoni D, Malagodi M, Milanese C, Licchelli M. Shellac/nanoparticles dispersions as protective materials for wood. Applied Physics A. 2016;**122**(12):1058. DOI: 10.1007/s00339-016-0577-7

[67] Sow C, Riedl B, Blanchet P. UV-waterborne polyurethane-acrylate nanocomposite coatings containing alumina and silica nanoparticles for wood: Mechanical, optical, and thermal properties assessment. Journal of Coatings Technology and Research. 2011;**8**(2):211-221. DOI: 10.1007/s11998-010-9298-6

[68] Godnjavec J, Znoj B, Venturini P, Žnidaršič A. The application of rutile nano-crystalline titanium dioxide as UV absorber. Informacije MIDEM. 2010;**40**(1):6-9

[69] Veronovski N, Verhovšek D, Godnjavec J. The influence of surface-treated nano-TiO_2 (rutile) incorporation in water-based acrylic coatings on wood protection. Wood Science and Technology. 2013;**47**(2):317-328. DOI: 10.1007/s00226-012-0498-3

[70] Srinivas K. Pandey KK. Enhancing photostability of wood coatings using titanium dioxide nanoparticles. Wood is Good: Current Trends and Future Prospects in Wood Utilization. 2017:251-259. DOI: 10.1007/978-981-10-3115-1_23

[71] Auer G, Woditsch P, Westerhaus A, Kischkewitz J, Griebler W-D, Rohe M, Liedekerke M. Pigments, Inorganic, 2. White Pigments. In: Ullmann's Encyclopedia of Industria Chemistry, Chichester, West Sussx, UK. 2017. DOI: 10.1002/143-56007.n20_n01.pub2

[72] Nair S, Pandey KK, Gridhar NN. UV stabilization of wood by nano metal oxides dispersed in propylene glycol. Journal of Photochemistry and Photobiology. B, Biology. 2018;**183**. DOI: 10.1016/j.jphotobiol.2018.04.007

[73] Ozgenc O, Yildiz UC. Weathering resistance of oriental spruce wood treated with different protection processes. Journal of Materials in Civil Engineering. 2016;**28**(8). DOI: 10.1061/(ASCE)MT.1943-5533.0001493

[74] Lokhande G, Chambhare S, Jagtap R. Synthesis and properties of phosphate-based diacrylate reactive diluent applied to UV-curable flame-retardant wood coating. Journal of Coatings Technology and Research. 2017;**14**(1):255-266. DOI: 10.1007/s11998-016-9849-6

[75] Ohm RA, Riley R, Salamov A, et al. Genomics of wood-degrading fungi. Fungal Genetics and Biology. 2014;**72**:82-90. DOI: 10.1016/j.fgb.2014.05.001

[76] Abdel-Hamid AM, Solbiati JO, Cann IK. Insights into lignin degradation and its potential industrial applications. Advances in Applied Microbiology. 2013;**82**:1-28. DOI: 10.1016/B978-0-12-407679-2.00001-6

[77] Kose C, Kartal SN. Tolerance of brown-rot and dry-rot fungi to CCA and ACQ wood preservatives. Turk Journal of Agriculture and Forestry. 2010;**34**:181-190. DOI: 10.3906/tar-0902-43

[78] Osman ME-S, EL-Shaphy AAE-N, Meligy DA, Ayid MM. Survey for fungal decaying archaeological wood and their enzymatic activity. International Journal of Conservation Science. 2014;**5**(3):295-308

[79] Helmi FM, Ali NM, Ismael SM. Nanomaterials for the inhibition of microbial growth on ancient Egyptian funeral masks. Mediterranean Archaeology and Archaeometry. 2015;**15**(3):87-95. DOI: 10.5281/zenodo.18360

[80] Dakal TC, Kumar A, Majumdar RS, Yadav V. Mechanistic basis of antimicrobial actions of silver nanoparticles. Frontiers in Microbiology. 2016;**7**:1-17. DOI: 10.3389/fmicb.2016.01831

[81] Liu Z, Wang Y, Pan X, Ge Q, Ma Q, Li Q, Fu T, Hu C, Zhu X, Pan J. Identification of fungal communities associated with the biodeterioration of waterlogged archaeological wood in a Han Dynasty Tomb in China. Frontiers in Microbiology. 2017;**8**:1-9. DOI: 10.3389/fmicb.2017.01633

[82] Fazio AT, Papinutti L, Gómez BA, Parera SD, Rodríguez Romero A, Siracusano G. Fungal deterioration of a Jesuit South American polychrome wood sculpture. International Biodeterioration & Biodegradation. 2010;**64**:694-701. DOI: 10.1016/j.ibiod.2010.04.012

[83] Taghiyari HR, Kalantari A, Ghorbani M, Bavaneghi F, Akhtari M. Effects of fungal exposure on air and liquid permeability of nanosilver- and nanozincoxide-impregnated Paulownia wood. International Biodeterioration & Biodegradation. 2015;**105**:51-57. DOI: 10.1016/j.ibiod.2015.08.014

[84] Koziróg A, Rajkowska K, Otlewska A, Piotrowska M, Kunicka-Styczynska A, Brycki B, Nowicka-Krawczyk P, Koscielniak M, Gutarowska B. Protection of historical wood against microbial degradation—Selection and application of microbiocides. International Journal of Molecular Sciences. 2016;**17**(1364):1-15. DOI: 10.3390/ijms17081364

[85] Rajkowska K, Koziróg A, Otlewska A, Piotrowska M, Nowicka-Krawczyk P, Brycki B, Kunicka-Styczyńska A, Gutarowska B. Quaternary ammonium biocides as antimicrobial agents protecting historical wood and brick. Acta Biochimica Polonica. 2016;**63**(1):153-159. DOI: 10.18388/abp.2015-1134

[86] Guo H, Bachtiar EVRibera J, Heeb M, Schwarze FWMR, Burgert I. Non-biocidal preservation of wood against brown-rot fungi with a TiO_2/Ce xerogel. Green Chemistry. 2018;**20**:1375-1382. DOI: 10.1039/C7GC03751A

Engineering, Models and Applications

Magnetic Materials by Melt Spinning Method, Structural Characterization, and Numerical Modeling

Marcelo Rubén Pagnola, Jairo Useche Vivero and
Andrés G. Marrugo

Additional information is available at the end of the chapter

Abstract

Chill block melt spinning is used in industrial processes for the production of metallic glasses. It is a rapid solidification process whereby a liquid metal is ejected at high pressure and temperature via a nozzle onto a rotating wheel solidifying in the form of a ribbon. In this work, starting from an alloy with the composition of $Fe_{78}Si_9B_{13}$ (% at.) reproduces the melt spinning technique to get the amorphous magnetic material. A *CFD3D* model based on the finite volume method (*FVM*) is proposed. For this purpose, the *OpenFoam*® open source code is used. In the ribbon production stage, it has been observed that the turbulence involved in the first reported transient lasts a few milliseconds, enough time to study the process with high-speed cameras. We measure the ejection speed by using optical flow on the melt contour. This enables us to check defects in the ribbons, which are predicted with the computational model, such as the case of cracks caused by irregularities in the first formation of the solid layer. The temperature measurement method relies on the fact that the digital camera is sensitive to electromagnetic radiation between 400 and 1000 nm in wavelength and the fact that the image gray level, which is proportional to the temperature *T*, provided the background illumination level is negligible.

Keywords: melt spinning, magnetic materials, OpenFoam, CFD, finite volume method

1. Introduction

Since the 1980s, the production of magnetic materials has been carried out mainly through the melt spinning process. These materials, obtained in the form of low thickness ribbons, have increased magnetic capacities with the utilization of alloys with amorphization capacity and

nanocrystalline. Among these alloys, those of $Fe_{78}B_{13}Si_9$ (% at.) for electric transformer cores are the most used because they manage to reduce vacuum losses up to 80% when compared to those of the cores constructed with oriented grain $FeSi$ sheets, normally used in these devices. The melt spinning process consists of forming a thin sheet of metal alloy on a rotating flat surface at a constant temperature. In this process, a jet of liquid metal is expelled through a nozzle by the overpressure of an inert gas, and it impacts on the surface of a rotating solid copper wheel. In this way, it forms a thin layer of molten material that quickly solidifies as a continuous ribbon that is then collected and rolled to obtain the magnetic coils as the final product. According to the distance between the nozzle and the rotating wheel (gap), the following processes are determined: *chill block melt spinning* (*CBMS*) and *planar flow casting* (*PFC*). In the *CBMS*, the jet of liquid metal is expelled through a nozzle with a gap >1 mm. In the *PFC*, however, the gap is less than 1 mm. In these sections, we will talk about the production of amorphous magnetic ribbons and the numerical modeling of the shaping process and its control of variables through the capture of high-resolution images.

2. Materials and methods

2.1. Set-up and production

$Fe_{78}Si_9B_{13}$ (% at.) ribbons are produced from an initial ingot previously melted in a vacuum atmosphere and a graphite crucible, from noncommercial alloys. The impurities in the noncommercial alloy are *Al*, *C*, *Ca*, and *S*. Their quantity is lower than 0.3% wt. These ribbons were cooled on the copper wheel with temperature controlled by optical pyrometer on a tripod located at 1 m of focal distance from the melted sample [1, 2].

These operations are developed in a 7.5 kW induction furnace *RDO*™ model *LFI-7.5* mounted as shown in **Figure 1**. The arrangement is formed by an induction coil inside a vacuum chamber, where an inert atmosphere is produced previously with a mechanical vacuum pump. The gap values used are typical to identify this methodology as chill block melt spinning [3].
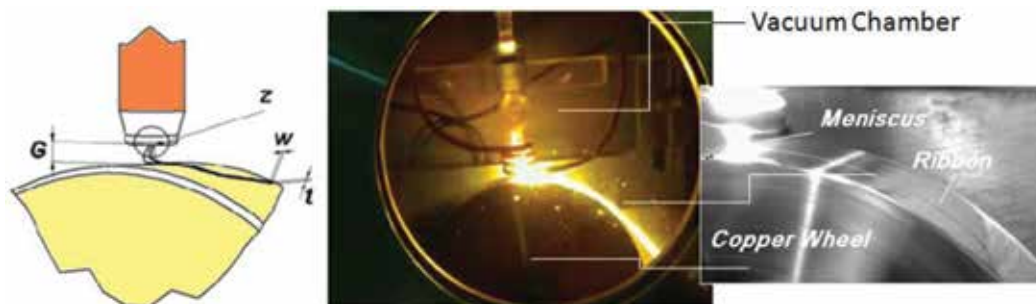

Figure 1. Melt spinning equipment and process of $Fe_{78}B_{13}Si_9$ (% at.) ribbons.

With an argon overpressure, the alloy melted is expulsed through the nozzle at an ejection velocity over the spinning wheel. Our implementation of the process captured with a high-speed camera can be observed in **Figure 2(a)**. It is similar to the one reported by Ames Laboratory, USA in **Figure 2(b)**.

To determine the width (w), we used a vernier with 0.02 mm precision and an external micrometer (0–25 mm) with 0.01 mm precision for thickness (t) determination. Three sections of approximately 100 mm of each ribbon were selected in five measurement places. An average value was reported.

2.2. Obtained product and results

The cooling rate was estimated according to -2.73×10^6 K/s with a wheel speed (V_x) in accordance with **Table 1**, and the relationship $x/z = 3.8395$, being $z = 0.0006$ m the orifice diameter in the nozzle with a solidification time of 9.4×10^{-7} s [4].

In **Figure 3**, the z/w ratio decay for the measured values with gaps (G) 2, 3, and 4 mm and orifice diameter (z) of 0.7 mm is shown. Between 35 and 40 m/s in the 2 mm gap curve, microspheres were obtained without ribbon formation, due to speeds of over 30 m/s, local vortices appear in the surrounding atmosphere that increases the convective flow along the wheel surface. These values define the vorticity in the contact zone, showing the influence of the coefficient of convective heat transfer (h) and the Biot number (B_i) as shown in **Figure 4**.

This effect is indicative of the Newtonian cooling in the solidification process of amorphous ribbons. The features are already reported by Pagnola et al. [4, 5]. For wheel speeds between 5 and 40 m/s, the thickness (t) values are compared with Tkatch et al. [6] and are plotted in **Figure 5**.

a)   b)
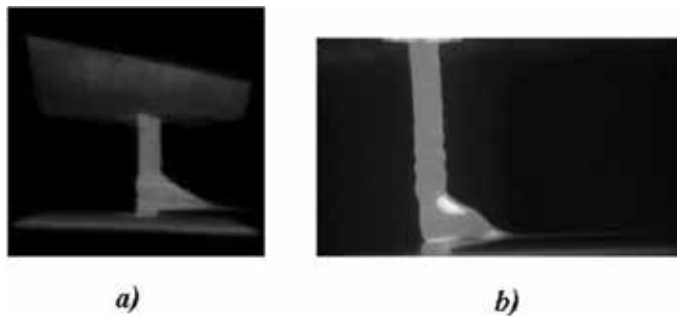
Figure 2. (a) *CBMS* of $Fe_{78}B_{13}Si_9$ (% at.) in *Pilot Plant of Magnetics Materials* (*INTECIN*) in **Table 1** conditions. (b) Similar *CBMS* process courtesy of *Ames Lab, US DOE*.

Speed wheel (m/s)	Gap (mm)	Ejection pressure (bar)
5–40	2, 3, and 4	0.3

Table 1. Production parameters.
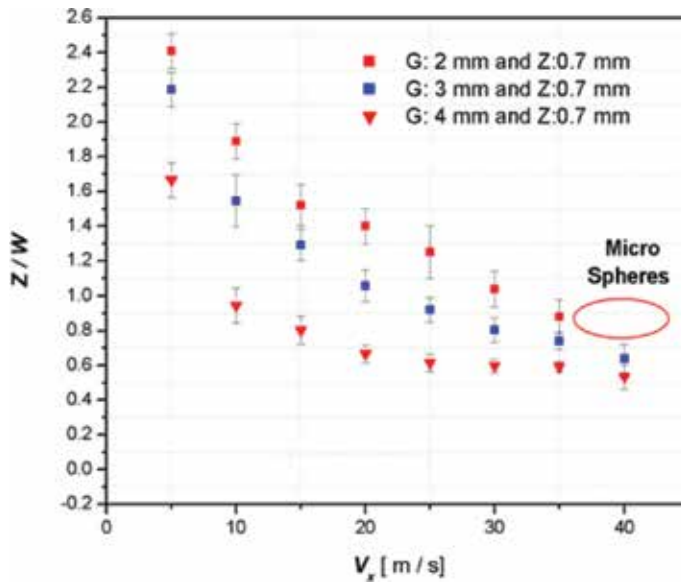
Figure 3. Comparative decreasing of *z/w* ratio with the tangential velocity *Vx*.
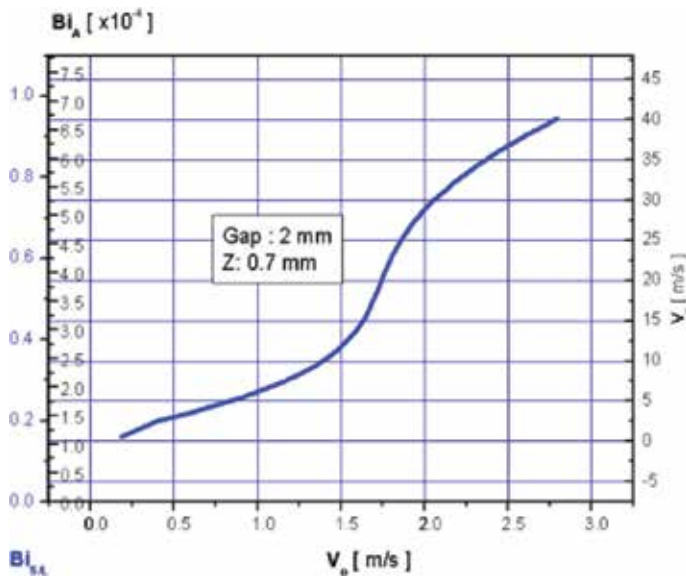
Figure 4. Triple entrance curve for the velocity values in the nozzle (V_0) that determine the Biot number according to the speed of the wheel *Vx* for *G* = 2 and *Z* = 0.7 mm.

The turbulence involved in the reported solidification times lasts a few milliseconds. Enough time to study the process with high-speed cameras and recreate *3D* numerical simulations that originate the defects that appear in the conformation of the ribbon is as follows:
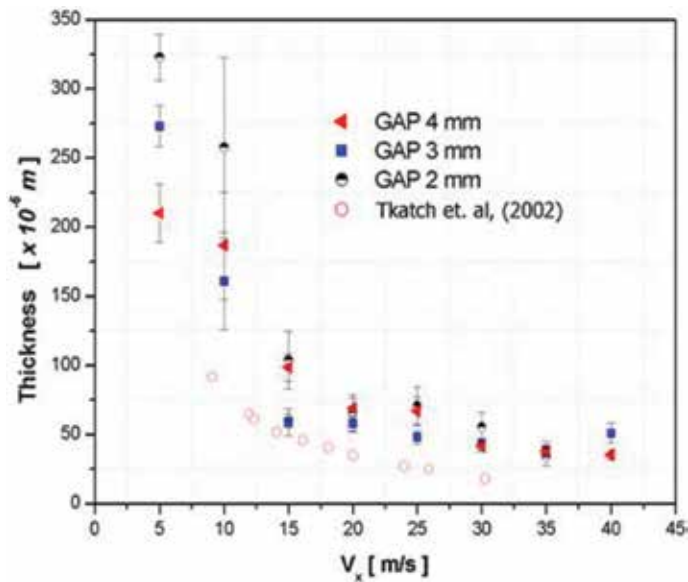
Figure 5. Comparative decreasing of ribbon thickness (t) with V_x.

Defects in the solidification: At the beginning of the ejection, the formation of a meniscus of material generates an irregular profile with changes in the ribbon thickness, which is still in a liquid state. The contact of this irregular thickness profile makes the solidification process begin in the thinnest part of the film because this is the one that changes its temperature faster and, therefore, its viscosity. This mechanism causes a continuous solid contour similar to that of a hole to be generated, which propagates in the film while continuing to maintain that thin thickness (*Point 1*—**Figure 6**).

Transition zone: It appears in a more stable meniscus, and subsequently, some are observed irregularities. This zone has a constant contour, and the ribbon with almost imperceptible defects of the order of 5 μm can be observed (*Point 2*—**Figure 6**).

Zone of homogeneous thickness: Once the turbulence in the meniscus is over after which the process stabilizes, the defects disappear giving way to a continuous ribbon with properties and qualities ready for specific use in electronic devices and with qualities that far exceed standard materials, such as its frequency response to variable magnetic fields. The scanning electron microscopy (*SEM*) view (*Point 3*—**Figure 6**) is consistent with the expectation of an achieved high cooling rate that avoids the total crystallization, resulting in an amorphous structure confirmed by X-ray diffraction (*XRD*) and Mössbauer Microscopy (*MS*) analysis. Similar to the report by Miglierini [7], it can be attributed to *Fe* atoms surrounded by *Si* atoms, in a remanent amorphous phase attributed to *FeB* environments, according to Franke et al. [8], and environments rich in *Si* [4]. The difficulty of analyzing with the transmission electron microscopy (*TEM*) is due to the obtained average thickness of the ribbons because their commended thickness is limited to few hundreds of nanometers in this technique [9]. Later isothermal annealing on these tapes at temperatures close to 700°C indicates predominantly the formation of *nanocrystalline*
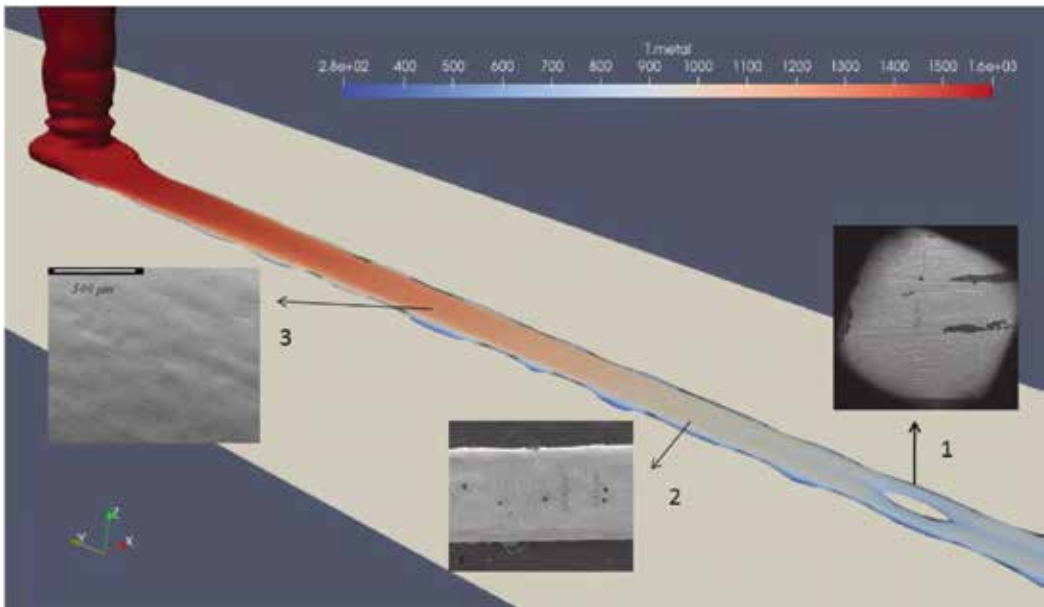
Figure 6. Characteristic zones of the production process.

structures with sizes that reach 6.31 nm over phases such as *FeB* [4]. Another way to obtain nanostructures is by isothermal annealing of melt-spun ribbons at 823 K for 1 h with the replacement of *B* for *Ge*: $Fe_{73.5}Si_{13.5}Ge_2B_7Nb_3Cu_1$ and $Fe_{73.5}Si_{13.5}Ge_4B_5Nb_3Cu_1$ [10].

The Vickers microhardness *HV 0.05* was determined in an average of a total of 10 measurements (**Figure 7**), obtaining a hardness of *1070 HV0.05*, equivalent to approximately *70 HRC*, *Rockwell C* scale.
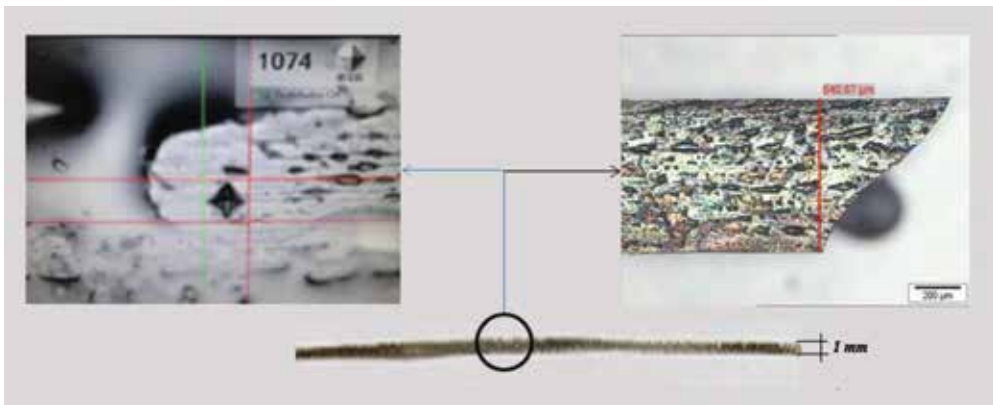
Figure 7. $Fe_{78}B_{13}Si_9$ (% at.) obtained ribbon.
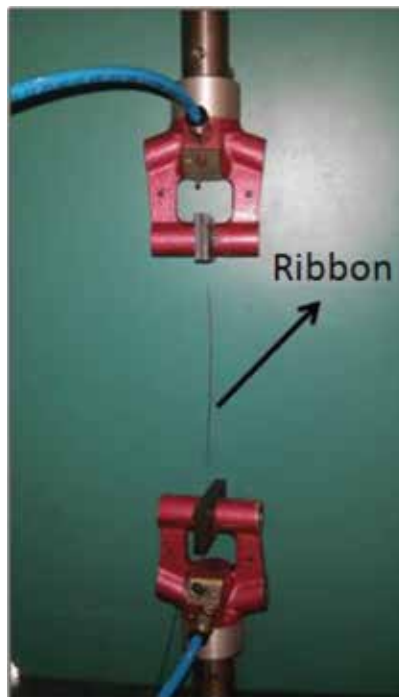
Figure 8. Tensile test on $Fe_{78}B_{13}Si_9$ ribbons.

Sample	n
Breakage average load (N)	11.95
Average section (mm^2)	0.063
Average resistance to traction (MPa)	190

Table 2. Average results of tensile tests on $Fe_{78}B_{13}Si_9$ ribbons.

For the tensile test of the ribbons, the device of **Figure 8** was used. Average values in 10 different samples were determined in **Table 2**.

3. Computational modeling

The work of Bussmann et al. [11] proposes a numerical solution of the equations of momentum and energy to study the condition of stable flow and temperature field in the puddle of the process of melt spinning. The proposed model considers the inertial effects, viscous, the surface tension, and the dependence of the viscosity with the temperature until the solidification of the material to an amorphous state.

In the work of Babei et al. [12], a numerical formulation based on the finite difference method is proposed to model the flow and heat transfer phenomenon transient in melting process. The results are contrasted with experimental models finding high consistency between the results.

In the work of Hui et al. [13], a numerical model is proposed for the study of the process of heat transfer and transient flow in the melt spinning process using the Navier-Stokes equations and the heat transfer equation. The proposed model allows the calculation of the cooling speeds along the thickness of puddle for different wheel speeds. Using experimental models, temperature distributions and cooling velocities were obtained, and similar results to those found in the numerical model were obtained.

Wang and Matthys [14] present a bi-dimensional finite difference semi-implicit numerical model for the study of the flow field and heat transfer with phase change in the casting model process. The boundary-layer theory is used to model these fields during the solidification process of the puddle.

Steen and Karcher [15] present the analysis of casting metals using spinning wheels. This work presents a broad discussion of flow stability, a relevant aspect in non-stable flow phenomena, which influences the movement of the meniscus, final texture, and instability of the morphological type of the solidification front.

Theisen et al. [16] focus their study on the behavior of the melt spinning process in time. The model developed is based on the equations of mass balance in unstable state combined with the Bernoulli equation of the flow. The proposed model allows to establish variations in different time scales, allowing to determine the time scale in which the process can be considered as stable. The evolution of the length of the puddle and the thickness of the produced metal tape indicates that the solidification speed varies over time.

In the work of Sowjanya and Kishen Kumar Reddy [17], they investigate the flow field of molten material in the puddle by determining pressure profiles, flow lines, and current function according to the injection pressure of the material in the nozzle. The proposed model allows to determine the point of separation of the material of the wheel to form the tape.

Sowjanya and Kishen Kumar Reddy [18] propose a bi-dimensional numerical model to model the molten puddle during the melt spinning process by finding stable puddle formation times related to its injection pressure. The comparison of experimental thicknesses with numerical results has a high concordance.

3.1. Governing equations

The numerical model is based on the following assumptions [11]:

- The width of the tape is much greater than the height of the gap, then puddle is considered essentially two dimensional.

- As the diameter of the wheel is much greater than the length of the puddle, the curvature of the wheel beyond the puddle is negligible. In addition, the lower surface of the puddle is considered flat.

- Molten material and the fluid that surrounds the puddle are considered as incompressible and a Newtonian fluid with laminar behavior.

- Density, surface tension, and thermal diffusivity of the molten material are considered constant. Kinematic viscosity depends on temperature.

- The heat flow between the tape and the wheel is of the convective type. The temperature of the wheel remains constant. The transfer of heat by radiation from the puddle is negligible.

The basic equations that govern the phenomenon of molten metal flow in the melt spinning process are given by the mass balance equation:

$$\nabla.v = 0 \tag{1}$$

where v is the velocity field. The equation of momentum balance for a Newtonian fluid is given by:

$$\rho \frac{Dv}{Dt} = -\nabla p + \eta \Delta v + \rho b \tag{2}$$

where ρ is the density of the fluid; p is the pressure field; η is the kinematic viscosity; and b is the vector of mass forces. The energy conservation equation:

$$\rho c_p \frac{DT}{Dt} = -\nabla.(\lambda \nabla T) + \eta \acute{\gamma}2 + \acute{q}_{LH} \tag{3}$$

where c_p is the specific calorific capacity of molten material; T specifies the temperature field value; λ is the thermal conductivity of the fluid; $\acute{\gamma}$ represents the rate of deformation; and $\acute{q}_{LH}$ is the latent heat flux. The transportation equation that controls the movement of the free surface is given by:

$$\frac{\partial \Phi}{\partial t} + \nabla.(\Phi v) = \frac{D\Phi}{Dt} + \Phi.(\nabla.v) = 0 \tag{4}$$

In this equation, $\Phi(x)$ is the volume of fluid function (*VOF*), which is a discontinuous function that measures the amount of fluid present in a volume element taking values between 0 and 1 ($\Phi(x) = 0$, if the volume of fluid does not contain molten material and $\Phi(x) = 1$, when the volume contains entirety molten material).

3.2. Boundary conditions

On the solid surfaces of the injection and wheel nozzle, a non-slip and non-penetration flow condition is considered. On the surface of the wheel, the fluid moves at the same speed as the wheel. The *VOF* model is used through the transport equation to model the puddle-air interface. On the free surface of the inlet nozzle, a known pressure condition is used, which is equal to the injection pressure condition of the molten metal. As we have explained in [19], the flow of heat between the puddle and the wheel is modeled by:

$$\lambda \nabla T = h(T_{int} - T_\infty) \tag{5}$$

where h is the convective coefficient; T_{int} is the temperature at molten material on the wheel; and T_∞ is the room temperature [20].

4. Image-based measurements

CBMS is a highly sensitive process in which many variables should be taken into account both for computational modeling purposes and for quality control. To monitor the ribbon production stage and to validate our proposed model, we carried out several experiments via high-speed image acquisition using a *Vision research Phantom-HD* [21]. Using a high-speed camera, we can accurately determine the ejection speed and the temperature of the molten alloy as it flows from the nozzle to the spinning wheel. In the following subsections, we explain the image-based measurement details.

4.1. Ejection velocity measurement

The most frequently used technique for studying the *2D* and *3D* velocity field of fluids is called *particle image velocimetry* (*PIV*) [22]. It is an optical method of flow visualization in which the fluid is seeded with small tracer particles, assumed to follow the flow dynamics, and illuminated so that the particles are visible. The motion of the seeding particles is used to calculate the velocity field of the flow. However, to use *PIV*, the fluid has to be transparent and at temperatures that typically do not exceed 200°C [23]. In our case, *PIV* is not readily an option because the considered molten alloy in the melt spinning process is not transparent, and seeding a fluid at temperatures above 1000°C is not possible. Therefore, we limit our analysis to the measurement of the ejection velocity.

The ejection velocity of the molten alloy is a parameter that is directly linked to the ejection pressure, the fluid viscosity and temperature, and nozzle size. This velocity can be measured using image-based velocimetry. Recently, image-based velocimetry has become more attractive than *PIV* because of the advancement in computing power [24]. The most used image-based technique for estimating *2D/3D* motion or velocity fields is optical flow. Optical flow methods try to calculate the motion between the two image frames acquired at times t and $t + \Delta t$ at every pixel position. For a *2D + t* dimensional case, the assumption is that a pixel at location (x, y, t) with an intensity $I(x, y, t)$ will have moved by Δx, Δy, and Δt between the two image frames. This assumption is called the brightness constancy constraint and is given by the following expression [25]:

$$I(x, y, t) = I(x + \Delta x, y + \Delta y, t + \Delta t) \tag{6}$$

On the assumption that the movement is small, the image constraint at $I(x, y, t)$ can be expanded with a Taylor series to get

$$I(x + \Delta x, y + \Delta y, t + \Delta t) = I(x, y, t) + \frac{\partial I}{\partial x}\Delta x + \frac{\partial I}{\partial y}\Delta y + \frac{\partial I}{\partial t}\Delta t + H.O.T. \tag{7}$$

From these equations, it follows that

$$\frac{\partial I}{\partial x}V_x + \frac{\partial I}{\partial y}V_y + \frac{\partial I}{\partial t} = 0 \tag{8}$$

where V_x and V_y are the x and y components of the velocity or optical flow of $I(x, y, t)$, and $\frac{\partial I}{\partial x}$, $\frac{\partial I}{\partial y}$, and $\frac{\partial I}{\partial t}$ are the derivatives of the image at (x, y, t) in the corresponding directions. Eq. (8) has two unknowns and cannot be solved without additional equations or constraints. All optical flow methods introduce additional conditions for estimating the actual flow. In this work, we use the Lucas-Kanade method [26] in which the underlying assumption is that the flow is essentially constant in a local neighborhood of the pixel under consideration. Therefore, the optical flow equations for all the pixels in a given neighborhood are solved in the least-square sense.Using optical flow, we can compute the two components (u, v) of velocity per pixel. However, often such high-resolution optical flow is not needed, and at that resolution, the resulting flow is noise prone. In our implementation, the optical flow estimation uses median filtering to obtain a noise robust *2D* velocity field from which we can obtain the ejection velocity. In addition, we obtain a binary mask to compute the optical flow from the region of interest to avoid detecting changes in brightness or reflections on the wheel as motion. In **Figure 9**, we show the successive image frames during ejection for a single experiment. The first frame shows the crucible, and the nozzle before the ejection, the intermediate frames show the ejection of the molten alloy, and the final frame shows the instant when the alloy comes into contact with the spinning wheel and starts to flow. From these data, we can calculate many parameters related to the ejection. We show the maximum speed per frame. At a frame rate of 5602 fps, the molten alloy takes about 14 frames to be ejected and comes into contact with the rotating wheel. Knowing the gap between the nozzle and the wheel (2 mm) and the fact that the alloy takes 2.499 ms to come into contact with the wheel, we compute an average speed of 0.80 m/s (**Figure 2**). This value is in agreement with the computed maximum speeds as shown in **Figure 9**.

4.2. Temperature measurement

CBMS is a technological process characterized by high-material velocities in which a precise high-speed temperature measurement is essential. Due to the presence of multiple flow phases and the high temperatures of the molten alloy (often above 1500°C), only non-contact methods can be used to measure the temperature. Pyrometers and infrared cameras are the most common non-contact temperature measurement devices [27]. However, on the one hand, pyrometers are only capable of single-point temperature measurements. On the other hand, despite the high cost, infrared cameras are not appropriate for high-speed applications due to their limited spatial resolution and dynamic response.The ejected molten alloy in the melt spinning process can reach temperatures well above 1500°C. At this temperature, the alloy emits a considerable amount of light in the visible and near infrared part of the electromagnetic spectrum. Roughly between
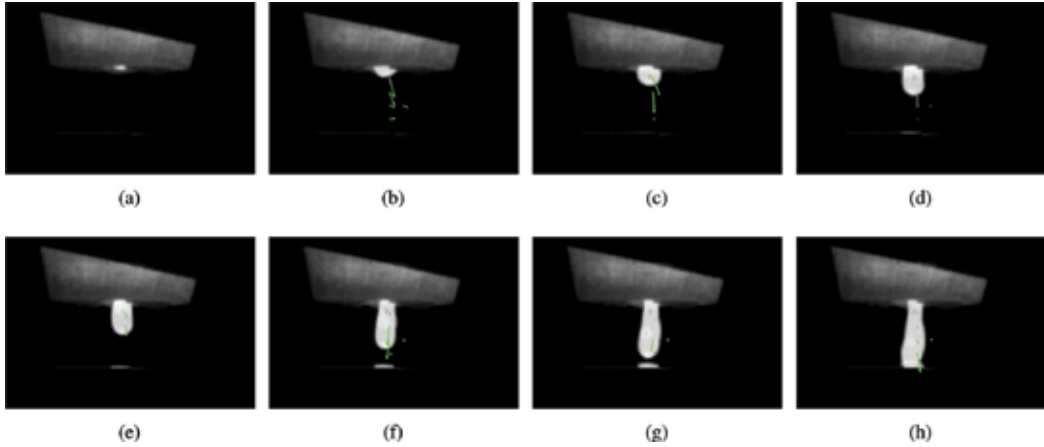
Figure 9. Velocity measurement of molten alloy ejection by optical flow. The arrows indicate the most significant velocity. Maximum speed: (a) 0.008 m/s; (b) 0.087 m/s; (c) 0.408 m/s; (d) 1.227 m/s; (e) 1.354 m/s; (f) 1.193 m/s; (g) 0.745 m/s; and (h) 0.806 m/s.

400 nm and 1000 nm, this band is where standard *CCD* and *CMOS* camera sensors are most sensitive. This advantage is the reason for using conventional high-speed imaging cameras for temperature measurement.In our *CBMS* experimental set-up, we measured the temperature of the molten alloy using the recently proposed method by Bizjan et al. [28]. Using a high-speed monochrome camera, we capture intensity images in 10-bit resolution and size 320×200 at 5602 fps. For the temperature calculation, the required input is the normalized image gray level G, 0 (black) $\leq G \leq 1$ (white). This gray level is assumed to be proportional to the camera sensor voltage response due to the incident light, which in turn depends on the equations for gray body radiation. The equations for calculating the temperature are as follows:

$$T_k = C^4 \sqrt{\frac{G}{k \cdot \eta(T_k) \cdot t_E \cdot \sigma_s}} \tag{9}$$

$$\eta = \frac{\int_0^\infty Y(\lambda) B_\lambda(\lambda) d\lambda}{\int_0^\infty B_\lambda(\lambda) d\lambda} \approx \frac{\sum_{0.4\ \mu m}^{1\mu m} Y(\lambda) B_\lambda(\lambda) \Delta\lambda}{\frac{2}{15} \frac{\pi^4 k_B^4}{h^3 c^2}} \tag{10}$$

$$B_\lambda = \frac{2hc^2}{\lambda^5} \frac{1}{\exp\left(hc/\lambda k_B T_K\right) - 1} \tag{11}$$

In Eqs. (9)–(11), T_K is the absolute temperature in (K); k is the camera sensor sensitivity; t_E is the camera shutter time; η is the light efficacy; Y is the sensor quantum efficiency; λ is the wavelength of light; and B_λ is the spectral radiance. The physical constants are $\sigma_s = 5.67 \times 10^{-8}$ W m^{-2} K^{-4} (Stefan-Boltzmann constant); $k_B = 1.381 \times 10^{-23}$ J/K (Boltzmann constant); $h = 6.626 \times 10^{-34}$ J s (Planck constant); and $c = 2.998 \times 10^8$ m/s (speed of light in vacuum).

As proposed by Bizjan et al. [28], many variables are not directly measured or known, but it is safe to assume that they remain constant during the experiment. The constant C implicitly contains all these variables, and its value depends on the measurement set-up. These variables
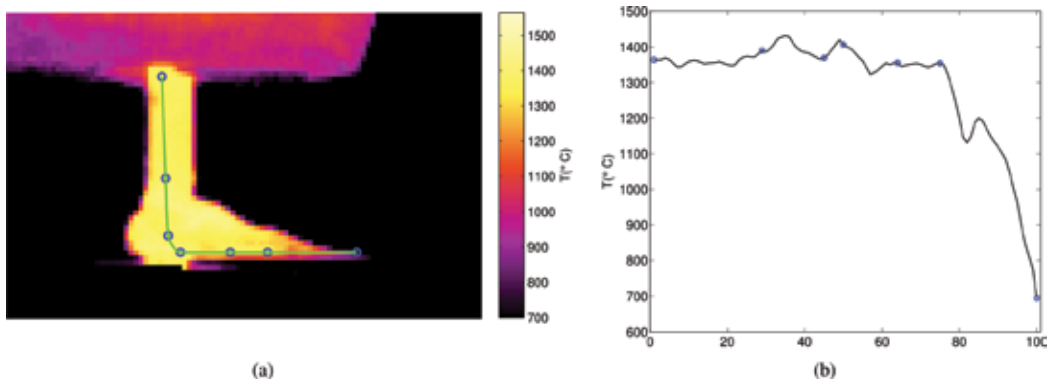
Figure 10. Temperature measurement by high-speed camera.
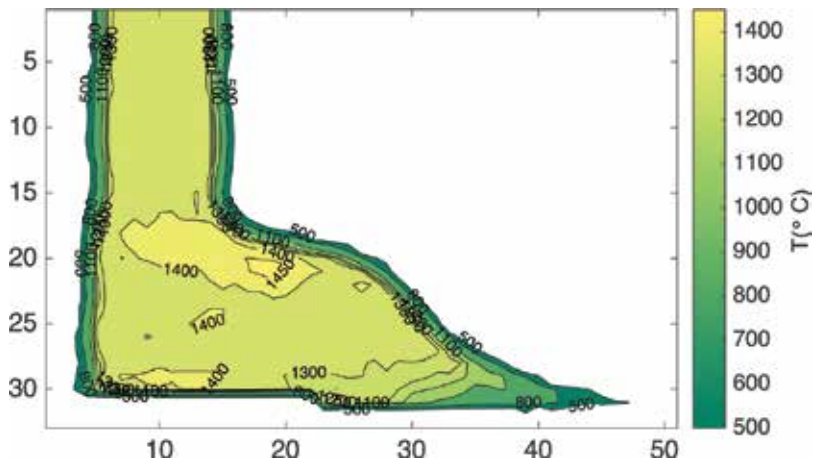
Figure 11. Temperature field as a contour plot.

include the surface emissivity e (proportional to C^4), the lens aperture setting, the focal distance, and the internal light absorption. The constant C is obtained from Eq. (6) by means of calibration to a surface with a known reference temperature and the corresponding image gray level at that location. In our experiments, we measured the reference temperature with a pyrometer.

In **Figure 10**, we show the stable flow of the molten alloy in the *CBMS* process. The green profile indicates the rapid cooling rate with a drop from approximately 1300 to 400°C in a distance of less than 1 mm. To accurately assess the beginning of the solidification process, we show in **Figure 11** the temperature flow field as a contour plot and note the lower regions with temperatures below 800°C.

5. Conclusions

In this chapter, we have described the *CBMS* industrial process for a commercial alloy of $Fe_{78}Si_9B_{13}$ (% at.) used in the industry as a magnetic material for applications in the electrical

transformer industry. We have studied this practical process from the generation of a mother alloy to its casting into a thin ribbon for its industrial application. The production parameters corresponding to its ejection have been reported under different conditions and compared with those obtained by other authors, resulting in similar characteristics in both thickness (*t*) and width (*W*). The mechanical parameters of the produced ribbons are reported. In addition, we have described the turbulence phenomena reported in previous works. This turbulence was introduced in the numerical modeling with the *FVM* methodology, agreeing with defects found in the rugosity of the ribbon in different areas perfectly differentiated characteristics in the solidification process (see **Figure 6**). In the computational modeling of the process, we provide a brief review of other numerical methodologies used by different authors and the equations that govern the phenomenon along with the boundary conditions used in the numerical simulation procedure. We describe the most critical process for the considered parameters. In addition, we showed different methodologies for the digital capture of data to compare the temperature and velocity profiles obtained in the process that allow validating the temperature profiles obtained in the numerical simulations to obtain the solidification profiles in the finished product.

Acknowledgements

Conflict of interest

It is hereby acknowledged that all the authors participating in this work do not present any real or potential conflict of interest, including financial aspects.

Author details

Marcelo Rubén Pagnola[1]*, Jairo Useche Vivero[2] and Andrés G. Marrugo[2]

*Address all correspondence to: mpagnola@fi.uba.ar

1 University of Buenos Aires, National Council of Scientific and Technical Research, Institute of Technology and Engineering Sciences "Ing. Hilario Fernández Long" (INTECIN), Buenos Aires, Argentine

2 Facultad de Ingeniería, Universidad Tecnológica de Bolívar, Cartagena, Colombia

References

[1] Pagnola M, Saccone F, Ozols A, Sirkin H. Improvement to approximation of second order function of hysteresis in magnetic materials. COMPEL: The International Journal for Computation and Mathematics in Electrical and Electronic Engineering. 2009;**28**(6):1579-1589. DOI: 10.1108/03321640910999879

[2] Pagnola M, Katabian R. Development of a winding mechanism for amorphous ribbon used in transformer cores. In: Gokcek M, editor. Mechanical Engineering. Rijeka: InTech; 2012. pp. 277-291. DOI: 10.5772/37331. ISBN: 978-953-51-0505-3, Chapter 12

[3] Pavuna D. Production of metallic glass ribbons by the chill-block melt spinning technique in stabilized laboratory conditions. Journal of Materials Science. 1981;**16**(9):2419-2433. DOI: 10.1007/BF01113578

[4] Pagnola M, Malmoria M, Barone M, Sirkin H. Analysis of $Fe_{78}Si_9B_{13}$ (% at.) ribbons of noncommercial scrap materials produced by melt spinning equipment. Multidiscipline Modeling in Materials and Structures. 2014;**10**(4):511-524. DOI: 10.1108/MMMS-11-2013-0068

[5] Pagnola M, Barone M, Malmoria M, Sirkin H. Influence of z/w relation in chill block melt spinning (CBMS) process and analysis of thickness in ribbons. Multidiscipline Modeling in Materials and Structures. 2015;**11**(1):23-31. DOI: 10.1108/MMMS-02-2014-0008

[6] Tkatch VI, Limanovski AI, Denisenko SN, Rassolov SG. The effect of the melt-spinning processing parameters on the rate of cooling. Materials Science and Engineering A. 2002;**323**:91-96. DOI: 10.1016/S0921-5093(01)01346-6

[7] Miglierini M. Mossbauer-effect study of the hyperfine field distributions in the residual amorphous phase of Fe-Cu-Nb-Si-B nanocrystalline alloys. Journal of Physics: Condensed Matter. 1994;**6**(7):1431-1438. DOI: 10.1088/0953-8984/6/7/015

[8] Franke H, Dey S, Rosemberg M. Hyperfine fields and local magnetic moments of metallic glasses of 3D-transition metals. Journal of Magnetism and Magnetic Materials. 1980;**15/18**: 1364-1366. DOI: 10.1016/0304-8853(80)90323-6

[9] Busby Y, Pireaux JJ. Metal nanoparticle size distribution in hybrid organic/inorganic films determined by high resolution X-ray photoelectron spectroscopy. Journal of Electron Spectroscopy and Related Phenomena. 2014;**192**:13-18. DOI: 10.1016/j.elspec.2013.12.010

[10] Muraca D, Silveyra J, Pagnola M, Cremaschi M. Nanocrystals magnetic contribution to FINEMET-type soft magnetic materials with Ge addition. Journal of Magnetism and Magnetic Materials. 2009;**321**:3640-3645. DOI: 10.1016/j.jmmm.2009.07.005

[11] Bussmann M, Mostaghimi J, Kirk DW, Graydon JW. A numerical study of steady flow and temperature fields within a melt spinning puddle. International Journal of Heat and Mass Transfer. 2002;**45**:3997-4010. DOI: 10.1016/S0017-9310(02)00112-6

[12] Babei R, Esmaellian H, Varahram N, Davami P. Mathematical and computational modeling of mold filling and heat transfer in metal casting. Iranian Journal of Science & Technology, Transaction B, Engineering. 2005;**29**(B5):511-530. DOI: 10.1.1.573.5964&rep=rep1&type=pdf

[13] Hui XD, Yang YS, Chen XM, Hu ZQ. Transient heat transfer and fluid dynamics during the melt spinning process of $Fe_{78}Si_9B_{12}Mo$ amorphous alloy. Science and Technology of Advanced Materials. 2001;**2**:265-270. DOI: 10.1016/S1468-6996(01)00067-5

[14] Wang GX, Matthys EF. Mathematical simulation of melt flow heat transfer and non-equilibrium solidification in planar flow casting. Modelling and Simulation in Materials Science and Engineering. 2002;**10**:35-55. DOI: 10.1088/0965-0393/10/1/304/pdf

[15] Steen PH, Karcher C. Fluid mechanics of spin casting of metals. Annual Review of Fluid Mechanics. 1997;**29**:373-397. DOI: 10.1146/annurev.fluid.29.1.373

[16] Theisen EA, Davis MJ, Weinstein SJ, Steen PH. Transient behaviour of the planar-flow melt spinning process. Chemical Engineering Science. 2010;**65**:3249-3259. DOI: 10.1016/j.ces.2010.02.018

[17] Sowjanya M, Kishen Kumar Reddy T. Flow dynamics in the melt puddle during planar flow melt spinning process. Materials Today Part A. 2017;**4**(2):3728-3735. DOI: 10.1016/j.matpr.2017.02.268

[18] Sowjanya M, Kishen Kumar Reddy T. Obtaining stable puddle and thinner ribbons during planar flow melt spinning process. Materials Today Part A. 2017;**4**(2):890-897. DOI: 10.1016/j.matpr.2017.01.100

[19] Pagnola M, Malmoria M, Barone M. Biot number behaviour in the chill block melt spinning (CBMS) process. Applied Thermal Engineering. 2016;**103**:807-811. DOI: 10.1016/j.applthermaleng.2016.04.077

[20] Carpenter JK, Steen PH. Heat transfer and solidification in planar-flow melt-spinning: High wheelspeeds. International Journal of Heat and Mass Transfer. 1997;**40**(9):1993-2007. DOI: 10.1016/S0017-9310(96)00305-5

[21] Marrugo AG, Barone M, Useche J, Pagnola M. Experimental investigation of high-speed melt spinning by means of digital image analysis, presented at the Latin America Optics and Photonics Conference; Washington, D.C; 2016. p. LTh2C.5. DOI: 10.1364/LAOP.2016.LTh2C.5

[22] Nigen S, El Kissi N, Piau JM, Sadun S. Velocity field for polymer melts extrusion using particle image velocimetry. Journal of Non-Newtonian Fluid Mechanics. 2003;**112**(2):177-202. DOI: 10.1016/S0377-0257(03)00097-1

[23] Wernet MP, Hadley JA. A high temperature seeding technique for particle image velocimetry. Measurement Science and Technology. 2016;**27**(12):1-10. DOI: 10.1088/0957-0233/27/12/125201/meta

[24] Zhang G, Chanson H. Application of local optical flow methods to high-velocity free-surface flows: Validation and application to stepped chutes. Experimental Thermal and Fluid Science. 2018;**90**:186-199. DOI: 10.1016/j.expthermflusci.2017.09.010

[25] Beauchemin SS, Barron JL. The computation of optical flow. ACM Computing Surveys (CSUR). 1995;**27**(3):433-466. DOI: 10.1145/220000/212141/p433-beauchemin.pdf?

[26] Lucas BD, Kanade T. An iterative image registration technique with an application to stereo vision. In: Proceedings of Imaging Understanding Workshop; 1981. pp. 121-130

[27] Bizjan B, Kuznetsov A, Jeromen A, Govekar E, Sirok B. High-speed camera thermometry of laser droplet generation. Applied Thermal Engineering. 2017;**110**(C):298-305. DOI: 10.1016/j.applthermaleng.2016.08.182

[28] Bizjan B, Širok B, Drnovšek J, Pušnik I. Temperature measurement of mineral melt by means of a high-speed camera. Applied Optics. 2015;**54**(26):7978-7984. DOI: 10.1364/AO.54.007978

Nanomaterials in Structural Engineering

Małgorzata Krystek and Marcin Górski

Additional information is available at the end of the chapter

http://dx.doi.org/10.5772/intechopen.79995

Abstract

Development of structural engineering, daring structures with record spans or heights, meets two serious obstacles—the limitations of traditionally used materials and the need of continuous monitoring of new structures subjected to complex loads, including those of dynamic nature. Considering the responsibility for the life of people and the budget of new structures, the need of constant monitoring is inevitable. This is why structural engineers seek for new solutions; among them, smart structures based on self-monitoring materials seem to be one of the most attractive proposals. It is still an unexplored area, but current research shows a high potential of the use of composites reinforced by carbon-based nanomaterials as self-sensing structural materials. Nanomaterials also influence other important features of structural materials, such as microstructure, mechanical, and transport-related properties. In this chapter, we present the state of art of the use of nanomaterials in structural engineering in various areas including mechanical and electrical properties as well as issues referring to durability.

Keywords: nanomaterials, structural engineering, graphene, smart materials, smart structures

1. Introduction

In 1959, during the Meeting of the American Physical Society at CalTech, the physicist Richard Feynman gave his famous speech entitled *"There's plenty of room at the bottom,"* and thus, the new nanotechnology era begun [1]. Feynman presented the idea of modifying and controlling matter at the scale of individual atoms and molecules [2]. However, it was only in 1974 when the term *"nanotechnology"* was created by Norio Taniguchi and was defined as processing materials by one atom or by one molecule [1, 3]. Since then, the definition of *"nanotechnology"*

has been modified several times over the years. Today, it can be defined as *"the application of scientific knowledge to manipulate, control and restructure matter at the atomic and molecular level in the range of 1–100 nm to exploit the size-dependent and structure-dependent properties and phenomena distinct from those at different scales"* [3]. Basically, nanotechnology is based on the statement that we can change any property of any material with reducing at least one dimension of this material into the nanoscale [4].

While nanotechnology has attracted attention in many fields of science and technology, including chemistry, electronics, medicine, or biology, its application in civil engineering, up to date, remains limited [1, 5–7]. These days, searching in SCOPUS database for the terms *"nanomaterial"* AND *"civil engineering"* within titles, abstracts and keywords of published papers returns only 18 document results. The RILEM TC 197-NCM Report [5] has highlighted, for the first time in 2004, the potential applications of nanotechnology in construction materials. The e-mail survey carried out among researchers, construction professionals, and large construction companies was the basis of reported information. The report revealed that little awareness of nanotechnology applications in construction is an effect of insufficient information on this subject. Therefore, nanotechnology was perceived as expensive and highly complex, thus discouraging potential customers. However, the results of the survey have shown that nearly 100 research projects carried out by respondents were based on nanotechnology. The potential nanotechnology applications were pointed out as follows:

- understanding nanostructure of materials,

- nanostructure modification of materials,

- functional films and coatings,

- smart structures and devices,

- environment-friendly applications [5].

Since then, research introducing nanotechnology in civil engineering has followed mainly these abovementioned development paths.

This chapter presents a review of the achievements of nanotechnology in Structural Engineering with special emphasis on improved physical parameters of structural materials and their potential in strengthening repairs and Structural Health Monitoring.

2. Improvement of mechanical properties and durability

Improvement of mechanical properties and durability of cementitious materials is mostly obtained by their nanostructure modification, that is, the incorporation of nanomaterials into cement matrix. Nanoparticles possess a high chemical reactivity due to a high surface area and can promote the growth of cement hydration products. Nanomaterials employed in cementitious composites, up to date, are nano-silica, nano-titania, nano-iron oxide, nano-alumina, nano-clay particles, carbon nanotubes, graphene oxide (GO), and graphene nanoplatelets (GNPs) [7].

Nano-silica (nano-SiO_2) is proved to enhance the compressive, tensile, and flexural strength of OPC pastes and mortars [8]. The addition of nano-SiO_2 effects in denser cement paste microstructure with improved porosity thus leads to a decreased water penetration and sorptivity [8] and therefore to the reduction of calcium leaching [9]. Nano-alumina (nano-Al_2O_3) matches the performance of nano-silica—it leads to a more compacted microstructure of cementitious composites, decreases their porosity, and enhances the compressive strength [10, 11]. It is worth noting that nano-alumina was proved to improve concrete performance at both elevated and low temperatures [10, 11]. The incorporation of nano-titania (nano-TiO_2) may lead to the enhancement of compressive and flexural strength as well as to the improvement in the resistance to chloride penetration due to a refined pore structure of the composites [12]. The impact of nano-titania addition on the performance of cementitious composites at an elevated temperature turned out to be comparable to composites incorporating nano-alumina [13].

However, the most studied nanomaterials to be used in cementitious composites are carbon-based nanomaterials. Until 1985, only two allotropic forms of solid carbon had been known, these had been diamond and graphite, which both feature covalently bonded networks [14]. In 1985, the new era of carbon nanomaterials had begun, when fullerenes—molecules composed of 60 carbon atoms, C60—had been discovered [14, 15]. It was less than 6 years later when it turned out that carbon atoms can also form cylindrical tubes. In 1991, Iijima [16] observed first the multi-walled carbon nanotubes (MWCNTs) and then in 1993, Iijima and Ichihashi [17] reported single-walled nanotubes (SWCNTs).

CNTs possess extraordinary electrical, thermal, and mechanical properties, highly relying on their dimensions. The diameters are in the range of 1.4–100 and 0.4–3 nm for MWCNTs and SWCNTs, respectively. Young's modulus for SWCNTs and MWCNTs is equal to ca. 1 and 0.21 TPa, respectively, while the tensile strength for both types of CNTs reaches 500 and 10–63 GPa [15].

Manufacturing of cementitious composites incorporating carbon-based nanomaterials is an extremely challenging task due to the crucial problem of obtaining a homogeneous dispersion of a nanomaterial within cement matrix. Carbon-based nanomaterials are prone to form aggregates and bundling as an effect of both their high hydrophobicity and strong van der Waals forces [18–20]. Nonuniformly dispersed nanoparticles strongly influence the workability and microstructure of cement composites and hinder the ongoing hydration; thus, it is of significant importance to adopt an appropriate treatment to obtain a sufficient consistency and dispersion of nanomaterial within cement matrix.

Several different attempts to obtain a homogeneous dispersion of CNTs in cement mix were reported, including carboxylation of CNTs [21], that is, special treatment to attach carboxylic acid to their surface or functionalization of CNTs with COOH groups [22, 23]. Nevertheless, the main approach employed to fabricate cement-CNT composites is, clearly, stirring and ultrasonication of aqueous dispersion of CNTs with various types of surfactants, such as polycarboxylic acid-based superplasticizers [23–25], anionic sodium dodecyl sulfate [20, 26], sodium dodecyl benzene sulfonate [27], nonionic polyoxyethylene(23) laurylether [20], Gum Arabic [22, 28], polyacrylic acid polymer [22], and cetyltrimethylammonium bromide [27], to name a few, or solvents, for instance, acetone [29]. It is worth noting that the studies on CNTs

dispersion [20, 30] have shown that the most beneficial dispersion is the one with a CNT-to-surfactant ratio of 1:1–1:5.

CNTs can enhance both the compressive and flexural strength of cementitious composites up to 50 [22] and 87% [24], respectively. The addition of CNTs also improves both the fracture energy and flexural toughness [31]. Young's modulus of cement mortars containing 0.1 wt% of CNTs can be even 100% higher compared to reference samples [24]. According to SEM images, the interaction between cement hydration products and CNTs is observed [32]. CNTs increase the crack bridging capacity of cementitious composites, acting as networks between the crack and the pores [23, 31, 33]. Moreover, nanoindentation investigation indicates that CNTs contribute to a higher growth of strong C–S–H phase [30]. CNTs act as the nanofiller of voids and thus reduce the total pore volume of cement paste [21, 23, 30, 32]. Interestingly, the addition of CNTs decreases the drying shrinkage of composites. Indeed, the authors [34] attributed this behavior to the reduction of micropores. It is worth noting that the influence of CNTs on the microstructure, porosity, and thereby mechanical properties of cementitious composites is highly dependent on the quality of their dispersion within cement matrix as well as on the type of surfactant to be used. Several studies show that the addition of CNTs may also deteriorate the properties of cementitious nanocomposites [28, 29, 33].

Over the past decades, graphene—another carbon allotrope, which is a single, planar, two-dimensional carbon layer [35]—has attracted considerable attention in science and technology, while its extraordinary properties have been extensively studied by various research groups. Especially, due to its outstanding mechanical [36] and electrical properties [37], graphene has emerged as the most promising nanomaterial for smart structures. Graphene is known to exhibit the intrinsic tensile strength of 130 GPa with a corresponding strain of 0.25, while its Young's modulus may be estimated at 1 TPa [36].

Nevertheless, studies on graphene-cement composites remain, up to date, limited due to the abovementioned perplexing problem of obtaining a uniform dispersion of a nanomaterial within cement matrix. For this reason, over the past years, special attention was paid to one of graphene derivatives, that is, graphene oxide (GO). Graphene oxide is highly dispersible in water [38] and therefore, as was assumed, also in cement mix. However, several studies [39–41] show that calcium ions present in cement paste negatively affect graphene oxide dispersion due to the chemical cross-linking phenomena. To circumvent this problem, different approaches have been persuaded, including the sonication of graphene oxide with polycarboxylate superplasticizer [42, 43] or silica fume [39, 40], which provide surface modification of nanomaterial and thereby separate graphene oxide nanoplatelets from calcium ions.

However, various cementitious composites incorporating graphene oxide, with or without surface modification, have emerged as materials with improved microstructure, mechanical properties, and durability. With the dosage of 0.03–0.05 wt% of GO, the increase up to 47, 61, and 79% has been reported for compressive [44], flexural, and tensile-splitting strength [45], respectively. The strengthening mechanism of GO in cement matrix is attributed to the chemical reaction between -COOH groups attached on the GO flakes and calcium ions from calcium hydroxide present in cement; thus, a 3D network structure is formed. Moreover, graphene oxide promotes and accelerates the growth of cement hydration products due to the

nucleation effect [46–48]. As a consequence of this 3D network, the microstructure of cement composites is visibly densified with a higher crystal growth and less prominent microcracks. Furthermore, also brittle crystals of ettringite are hardly observed [49]. The addition of GO remarkably refines the porosity, reducing the critical pore size and the volume of macropores [48, 50]. For the reason of reduced porosity, the incorporation of even small amount of GO into cementitious composites leads to a decreased sorptivity [50, 51]. The decrease up to 8 and 44% has been reported for initial and secondary sorptivity, respectively [50]. Therefore, cement-GO composites feature with a tremendously reduced ingress of chlorides. Even the marginal addition of graphene oxide of 0.01 wt% may effect in significant decrease of chloride penetration depth from 26 to 5 mm [51]. Interestingly, the addition of GO and its acceleration effect on cement hydration lead to a higher drying shrinkage at early stages of hydration. Nevertheless, since drying shrinkage depends on the tension of capillary pores, which are highly reduced in composites reinforced with graphene oxide, drying shrinkage after 28 days is then reduced [47].

Some attempts [19, 52] of introducing graphene nanoplatelets (GNPs) to improve the barrier properties and enhance the durability of cementitious composites have been reported. In this respect, this low-cost graphene derivative matches the performance of graphene oxide in concrete. The addition of 1.5 wt% of GNPs contributes to pore refinement, reducing the critical pore diameter and the average void size, thereby decreasing the water permeability, chloride diffusion, and chloride migration by 80, 80 and 40%, respectively [52]. It is worth noting that according to various authors, the addition of GNPs does not improve [52] or may even, to some extent, deteriorate [53] the strength of concrete.

3. Self-monitoring materials

Electrical properties of carbon-based materials in structural engineering are drawing attention of scientists for many years, giving hope for smart materials and self-monitoring structures.

One of the first attempts of using carbon-based materials in concrete was made almost three decades ago when cut carbon fibers were mixed with concrete for traffic monitoring and weighting in motion [54]. The results were promising; however, this solution had never been implemented in large scale.

The development of science and technologies during recent years has brought new nanomaterials as graphene or carbon nanotubes with even more interesting properties, also electrical. Former experiences in structural engineering materials but also in other areas of science as medicine or aviation encouraged scientists to return to the concept of self-monitoring materials for smart structures. Clearly, carbon nanotubes are the most studied carbon nanomaterial for self-monitoring applications in concrete.

Typically, various types of sensors are used to evaluate structural health, including optical fibers, strain gauges, and piezoresistive sensors. However, these sensors possess some serious limitations and disadvantages, such as high cost, poor durability, low sensitivity, and insufficient compatibility with concrete and expensive peripheral equipment [6, 55]. The

new generation of nanotechnology-based microelectromechanical system (MEMS) sensors has emerged as cheaper, more compact, and easier to install sensors than traditional ones. Nanotechnology/microelectromechanical systems were used, for instance, to measure temperature and internal relative humidity of concrete [56] or to detect cracks in concrete structures [57]. Sensors for detecting the structural integrity of concrete were fabricated as wireless cement-carbon nanotube sensors embedded into concrete beams [57]. These CNTs-cement sensors have emerged as a low-cost small wireless sensor with good sensitivity, significant repeatability, and low hysteresis. Moreover, Lebental et al. [58] have developed well-aligned, ultra-thin, dense carbon nanotube membranes to be used as a vibrating membrane in a capacitive micrometric ultrasonic transducers, which could be used in the durability monitoring of porous materials. Kang et al. [59] have fabricated a long biomimetic artificial neuron sensor, with features such as low cost, simple installation, and low weight. Due to low bandwidth and appropriate strain sensitivity, it can be used for the detection of both small and large strains and cracks in concrete structures, also under dynamic loading.

Interestingly, Nanni et al. [60] have presented self-sensing nanocomposite rods to be applied as both reinforcing elements and sensors in concrete structures. The self-sensing rods are composed of an internal conductive core, that is, glass fibers embedded in epoxy resin with carbon nanoparticles (CNPs) and an external insulting GFRP skin. The nanocomposite rods have proved to be suitable for self-monitoring of concrete beams under a four-point static bending as well as for concrete cure monitoring.

The concept of weighting loads in motion came back then recently with those new materials [61]. The research team conducted tests on compressed blocks of the concrete with carbon nanotubes and registered its performance under static and dynamic loads. The authors registered changes of electrical resistance readings, proving that even micro-strains may be measured by such smart materials. This very recent work demands more calibrating studies; still, it proves high potential of nano-concrete.

Outstanding electrical properties and low cost make graphene nanoplatelets (GNPs) an attractive nanomaterial for use in smart self-sensing concrete. As demonstrated by recent studies [62], the addition of 1.6 wt% of GNPs (a surface area of 192 m^2/g, a diameter of 6.8 μm, and a thickness of 5.0 nm) decreases more than one order of magnitude the resistivity of tested composites, thus attaining the percolation point, above which GNPs form the continuous conductive network in cement matrix. Interestingly, during the piezoresistive tests under compression, it turned out that no piezoresistive reactions were detected for samples containing 1.6 wt% of GNPs, indicating that conductive network created by tunneling of GNPs is unstable under applied loading. Indeed, the addition of only 6.4 wt% of GNPs has led to a sufficient and stable response of electrical parameters under cyclic loads. Other studies by Lee et al. [63] have revealed that, for GNPs with a surface area of 352 m^2/g, a diameter of 2.6 μm, and a thickness of 2.6 nm, the percolation threshold was obtained for 3.6 wt% amount of nanomaterial. Tests on samples with different notch depths confirmed the electrically conductive characteristics of manufactured mortar.

A very interesting and novel approach for use in structural engineering is connected with the proposal of Smart Bricks for Structural Health Monitoring of existing, often historical

structures endangered by hazardous loads as, for example, earthquakes [64]. Such products have the potential of creating self-sensing systems in historical structures, giving possibility for high-performance repairs and relatively cheap and invisible monitoring solution.

4. Other applications

Numerous exciting examples of antimicrobial and self-cleaning surfaces as well as energy-harvesting applications have also been reported in the last decade [6].

Recently, it has been shown [6, 65] that some nanoparticles possess tremendous antimicrobial properties and can be used to fabricate antimicrobial materials or coatings. In particular, TiO_2 nanoparticles proved to completely damage *Escherichia coli* cells after 1 week under UV irradiation of 1 mW/cm^2. Moreover, it has been reported that the addition of silver or copper may enhance the photocatalytic activity of nano-titania even under weak UV light [66]. Interestingly, Hochmannova and Vytrasova [67] have presented paints based on aqueous acrylic dispersion with the 5 vol% addition of nano-ZnO, which proved to be a better photocatalytic coatings than the one containing nano-TiO_2. The normal domestic fluorescent light was sufficient for nano-ZnO to activate the photocatalytic and microbial processes, deactivating the tremendously wide spectrum of bacteria and fungi. Furthermore, the studies on phenylpropyl type interior wall paints incorporating nano-MgO [68] have revealed that, in contrast to paints with nano-TiO_2 and nano-ZnO, nano-MgO possess a sufficient antimicrobial activity in the absence of light irradiation. In addition, the addition of silver nanoparticles to paints and coating effects in significant antimicrobial properties in case of both Gram-positive and Gram-negative bacteria [6, 69]. In case of carbon nanomaterials, SWCNTs can cause physical cell membrane damage and oxidative stress, impacting also metabolic activity and morphology of *E. coli* bacteria [70]. Grover et al. [71] have prepared laccase-based and chloroperoxidase-based paints, incorporating MWCNTs for biocatalytic coatings. These enzyme-nanotube-based paints exhibited a high bactericidal activity against different evaluated bacteria.

Apart from antibacterial surfaces, the addition of nanomaterials may also enhance the self-cleaning abilities of construction materials. Self-cleaning surfaces are mainly classified into two categories: hydrophobic and hydrophilic surfaces. As reported by previous studies [72–74], nano silica may be used to fabricate transparent superhydrophobic films and coatings on glass. The nanoporous structure made out of nano-SiO_2 also possesses antireflection properties [72, 73]. Hydrophobic surfaces were also developed with the use of carbon nanotubes (CNTs). Transparent, conductive, and superhydrophobic films incorporating CNTs were prepared on a glass substrate using, for instance, fluoropolymer-grafted MCWNTs [75] or CNTs produced by plasma-enhanced chemical vapor deposition and functionalized by a 1H,1H-2H,2H perfluorodecyl-trichlorosilane and hexane mixture [76]. Nanoparticles used typically in hydrophilic surfaces are materials with photocatalytic properties. Tan et al. [77] have revealed that transparent TiO_2 films fabricated by the growth of TiO_2 nanotube arrays on glass substrate have exhibited a higher photocatalytic activity than nanoparticulate TiO_2 thin films due to a higher surface area. Interestingly, Pan et al. [78] have presented nanofiber-based TiO_2 films with stable super-amphilicity, which possessed superhydrophilic properties even after 240 days in the

absence of UV irradiation. It is worth noting that the effect of various forms of TiO_2 [79] as well as the interaction between TiO_2 and pigments has been investigated in the case of cement mortars [80]. Mortar with the addition of 3% of anatase powder and 2% of anatase suspension has emerged as a commercially attractive material with optimal photoactivity [79].

Nanomaterials as conductive materials have also the potential for energy harvesting. Tests on this issue are conducted in many research centers, not connected with structural engineering. Some of them, especially those connected with obtaining energy from mechanical actions [81] and solar [82] activity, have the potential, which could also be considered in large engineering and special structures made out of smart nanomaterials.

5. Nano-toxicity

Among all nanomaterials, the toxicity of carbon nanotubes (CNTs) draws most attention due to their fiber structure and insolubility in lungs, thus significant similarity to asbestos [83]. Evaluation of carbon nanotubes (CNTs) toxicity is an extremely challenging task, since the reactivity of CNTs is influenced by many factors, such as surface area, size and shape, structural defects, purity, chemical composition, solubilization, surface chemistry, and charge [14, 83]. CNTs may cause inflammatory, genotoxic, and fibrotic effects in the lungs, thus contributing to lung cancer [84]. In addition, exposure to CNTs may also lead to skin irritation [84]. When CNTs ingress human cells, they can accumulate in cytoplasm and contribute to cell death [14].

Graphene oxide (GO) and graphene family nanomaterials (GFNs) have a strong antibacterial and antifungal activity. However, they may also negatively affect the biological structures of cells and cause side effects. First of all, the oxidative stress is detrimental to cellular macro-molecules: proteins, DNA, or lipids, just to name a few [85]. Moreover, due to sharp edges of graphene, it may damage cell membranes, thus causing the membrane destabilization [85, 86]. It is worth noting that graphene nanomaterial accumulations may be potentially toxic for certain organs, including lungs and liver [85]. Importantly, the toxicity of graphene and derivatives thereof depends strongly on the type of nanomaterial, its shape and size, purity, surface properties, synthesis method and post-producing treatment, dispersion degree, concentration, oxidative state, and functional groups [86, 87].

6. Conclusion

Nanotechnology has a high potential for applications in civil engineering. Nanomaterials such as nano-alumina, nano-titania, nano-silica, nano-magnesium oxide, nano-zinc oxide, silver nanoparticles, carbon nanotubes, or graphene derivatives may have enhanced hydration, microstructure, porosity, and thus mechanical properties and transport-related properties of cementitious composites (**Table 1**). Moreover, nanoparticles can also ensure completely new capabilities of structural composites, namely self-cleaning, self-sensing, and antimicrobial activities. Recent nanotechnological developments in civil engineering open up new avenues for the technological applications of nanomaterials in high-performance cement composites

Nanomaterial	Effect on the properties of building materials	References
Nano-alumina	Improved mechanical properties	[8, 10, 11]
	Refined microstructure and porosity	[8, 11]
	Accelerated hydration	[8]
	Reduced water absorption	[8]
	Increased impermeability	[10]
	Improved performance at elevated temperatures	[10]
	Enhanced frost resistance	[11]
Nano-silica	Improved mechanical properties	[9, 11]
	Refined microstructure and porosity	[9, 11]
	Enhanced corrosion resistance	[9]
	Enhanced frost resistance	[11]
	Self-cleaning properties	[72–74]
Nano-titania	Improved mechanical properties	[13]
	Refined microstructure and porosity	[12, 13]
	Enhanced corrosion resistance	[12]
	Increased impermeability	[13]
	Improved performance at elevated temperatures	[13]
	Self-cleaning properties	[66, 77–80]
	Antibacterial activity	[66]
Carbon nanotubes	Improved mechanical properties	[14, 18, 20–24, 27–33]
	Refined microstructure and porosity	[14, 21, 30–32]
	Reduced shrinkage	[14]
	Self-sensing properties	[24, 25, 27, 58, 59, 61]
	Enhanced corrosion resistance	[24]
	Self-cleaning properties	[75, 76]
	Antibacterial activity	[70, 71]
Graphene nanoplatelets	Refined microstructure and porosity	[19, 52]
	Reduced water absorption	[19, 52]
	Enhanced corrosion resistance	[19, 52, 62]
	Self-sensing properties	[53, 62, 63]
Graphene oxide	Improved mechanical properties	[41–43, 45, 46, 48–50]
	Refined microstructure and porosity	[41, 42, 44–46, 48–51]
	Accelerated hydration	[44, 47, 48]
	Reduced water absorption	[50, 51]
	Enhanced corrosion resistance	[51]
Silver nanoparticles	Antibacterial activity	[69]
Nano-magnesium oxide	Antibacterial activity	[68]
Nano-zinc oxide	Antibacterial activity	[67]

Table 1. Effect of the incorporation of various nanomaterials into building materials.

as well as in structural health monitoring. However, of significant importance is to focus on new solutions, which will facilitate the use of nanotechnology in real industrial-scale applications. Moreover, a key focus for the nanotechnology of structural composites should be ensuring the comprehensive toxicological studies.

Acknowledgements

Conflict of interest

The authors declare no conflict of interest.

Author details

Małgorzata Krystek and Marcin Górski*

*Address all correspondence to: marcin.gorski@polsl.pl

Silesian University of Technology, Gliwice, Poland

References

[1] Pacheco-Torgal F, Jalali S. Nanotechnology: Advantages and drawbacks in the field of construction and building materials. Construction and Building Materials. 2011;**25**:582-590. DOI: 10.1016/j.conbuildmat.2010.07.009

[2] Garrett SL, Poese ME. There's (still) plenty of room at the bottom. Applied Thermal Engineering. 2013;**61**:884-888. DOI: 10.1016/j.applthermaleng.2013.04.038

[3] Dahman Y, Lo HH, Edney M. An introduction to nanotechnology. In: Nanotechnology and Functional Materials for Engineers. Amsterdam, Netherlands: Elsevier; 2017. pp. 1-17. DOI: 10.1016/B978-0-323-51256-5.00001-0

[4] Hochella MF. Nanoscience and technology: The next revolution in the Earth sciences. Earth and Planetary Science Letters. 2002;**203**:593-605. DOI: 10.1016/S0012-821X(02)00818-X

[5] Zhu W, Bartos PJM, Porro A. Application of nanotechnology in construction summary of a state-of-the-art report. Materials and Structures. 2004;**37**:649-658. DOI: 10.1617/14234

[6] Hanus MJ, Harris AT. Nanotechnology innovations for the construction industry. Progress in Materials Science. 2013;**58**:1056-1102. DOI: 10.1016/j.pmatsci.2013.04.001

[7] Sanchez F, Sobolev K. Nanotechnology in concrete—A review. Construction and Building Materials. 2010;**24**:2060-2071. DOI: 10.1016/J.CONBUILDMAT.2010.03.014

[8] Nazari A, Riahi S. Al_2O_3 nanoparticles in concrete and different curing media. Energy and Buildings. 2011;**43**:1480-1488. DOI: 10.1016/j.enbuild.2011.02.018

[9] Gaitero JJ, Campillo I, Guerrero A. Reduction of the calcium leaching rate of cement paste by addition of silica nanoparticles. Cement and Concrete Research. 2008;**38**:1112-1118. DOI: 10.1016/J.CEMCONRES.2008.03.021

[10] Farzadnia N, Abang Ali AA, Demirboga R. Characterization of high strength mortars with nano alumina at elevated temperatures. Cement and Concrete Research. 2013;**54**:43-54. DOI: 10.1016/J.CEMCONRES.2013.08.003

[11] Behfarnia K, Salemi N. The effects of nano-silica and nano-alumina on frost resistance of normal concrete. Construction and Building Materials. 2013;**48**:580-584. DOI: 10.1016/J.CONBUILDMAT.2013.07.088

[12] Zhang M, Li H. Pore structure and chloride permeability of concrete containing nanoparticles for pavement. Construction and Building Materials. 2011;**25**:608-616. DOI: 10.1016/J.CONBUILDMAT.2010.07.032

[13] Farzadnia N, Abang Ali AA, Demirboga R, Anwar MP. Characterization of high strength mortars with nano Titania at elevated temperatures. Construction and Building Materials. 2013;**43**:469-479. DOI: 10.1016/J.CONBUILDMAT.2013.02.044

[14] Siddique R, Mehta A. Effect of carbon nanotubes on properties of cement mortars. Construction and Building Materials. 2014;**50**:116-129. DOI: 10.1016/J.CONBUILDMAT.2013.09.019

[15] Liew KM, Kai MF, Zhang LW. Carbon nanotube reinforced cementitious composites: An overview. Composites. Part A, Applied Science and Manufacturing. 2016;**91**:301-323. DOI: 10.1016/J.COMPOSITESA.2016.10.020

[16] Iijima S. Helical microtubules of graphitic carbon. Nature. 1991;**354**:56-58. DOI: 10.1038/354056a0

[17] Iijima S, Ichihashi T. Single-shell carbon nanotubes of 1-nm diameter. Nature. 1993;**363**:603-605. DOI: 10.1038/363603a0

[18] Sindu BS, Sasmal S. Properties of carbon nanotube reinforced cement composite synthesized using different types of surfactants. Construction and Building Materials. 2017;**155**:389-399. DOI: 10.1016/J.CONBUILDMAT.2017.08.059

[19] Du H, Pang SD. Enhancement of barrier properties of cement mortar with graphene nanoplatelet. Cement and Concrete Research. 2015;**76**:10-19. DOI: 10.1016/J.CEMCONRES.2015.05.007

[20] Sobolkina A, Mechtcherine V, Khavrus V, Maier D, Mende M, Ritschel M, et al. Dispersion of carbon nanotubes and its influence on the mechanical properties of the cement matrix. Cement and Concrete Composites. 2012;**34**:1104-1113. DOI: 10.1016/J. CEMCONCOMP.2012.07.008

[21] Li GY, Wang PM, Zhao X. Mechanical behavior and microstructure of cement composites incorporating surface-treated multi-walled carbon nanotubes. Carbon. 2005;**43**:1239-1245. DOI: 10.1016/j.carbon.2004.12.017

[22] Cwirzen A, Habermehl-Cwirzen K, Penttala V. Surface decoration of carbon nanotubes and mechanical properties of cement/carbon nanotube composites. Advances in Cement Research. 2008;**20**:65-73. DOI: 10.1680/adcr.2008.20.2.65

[23] Zou B, Chen SJ, Korayem AH, Collins F, Wang CM, Duan WH. Effect of ultrasonication energy on engineering properties of carbon nanotube reinforced cement pastes. Carbon. 2015;**85**:212-220. DOI: 10.1016/J.CARBON.2014.12.094

[24] Konsta-Gdoutos MS, Batis G, Danoglidis PA, Zacharopoulou AK, Zacharopoulou EK, Falara MG, et al. Effect of CNT and CNF loading and count on the corrosion resistance, conductivity and mechanical properties of nanomodified OPC mortars. Construction and Building Materials. 2017;**147**:48-57. DOI: 10.1016/J.CONBUILDMAT.2017.04.112

[25] Kim H-K. Chloride penetration monitoring in reinforced concrete structure using carbon nanotube/cement composite. Construction and Building Materials. 2015;**96**:29-36. DOI: 10.1016/J.CONBUILDMAT.2015.07.190

[26] Yu J, Grossiord N, Koning CE, Loos J. Controlling the dispersion of multi-wall carbon nanotubes in aqueous surfactant solution. Carbon. 2007;**45**:618-623. DOI: 10.1016/j. carbon.2006.10.010

[27] Luo J, Duan Z, Li H. The influence of surfactants on the processing of multi-walled carbon nanotubes in reinforced cement matrix composites. Physica Status Solidi (A) Applications and Materials. 2009;**206**:2783-2790. DOI: 10.1002/pssa.200824310

[28] Sáez De Ibarra Y, Gaitero JJ, Erkizia E, Campillo I. Atomic force microscopy and nanoindentation of cement pastes with nanotube dispersions. Physica Status Solidi (A) Applications and Materials. 2006;**203**:1076-1081. DOI: 10.1002/pssa.200566166

[29] Musso S, Tulliani J-M, Ferro G, Tagliaferro A. Influence of carbon nanotubes structure on the mechanical behavior of cement composites. Composites Science and Technology. 2009;**69**:1985-1990. DOI: 10.1016/J.COMPSCITECH.2009.05.002

[30] Konsta-Gdoutos MS, Metaxa ZS, Shah SP. Highly dispersed carbon nanotube reinforced cement based materials. Cement and Concrete Research. 2010;**40**:1052-1059. DOI: 10.1016/j.cemconres.2010.02.015

[31] Wang B, Han Y, Liu S. Effect of highly dispersed carbon nanotubes on the flexural toughness of cement-based composites. Construction and Building Materials. 2013;**46**:8-12. DOI: 10.1016/J.CONBUILDMAT.2013.04.014

[32] Nochaiya T, Chaipanich A. Behavior of multi-walled carbon nanotubes on the porosity and microstructure of cement-based materials. Applied Surface Science. 2011;**257**:1941-1945. DOI: 10.1016/J.APSUSC.2010.09.030

[33] Parveen S, Rana S, Fangueiro R, Paiva MC. Microstructure and mechanical properties of carbon nanotube reinforced cementitious composites developed using a novel dispersion technique. Cement and Concrete Research. 2015;**73**:215-227. DOI: 10.1016/J. CEMCONRES.2015.03.006

[34] Torabian Isfahani F, Li W, Redaelli E. Dispersion of multi-walled carbon nanotubes and its effects on the properties of cement composites. Cement and Concrete Composites. 2016;**74**:154-163. DOI: 10.1016/J.CEMCONCOMP.2016.09.007

[35] Geim AK, Novoselov KS. The rise of graphene. Nature Materials. 2007;**6**:183-191. DOI: 10.1038/nmat1849

[36] Lee C, Wei X, Kysar JW, Hone J. Measurement of the elastic properties and intrinsic strength of monolayer graphene. Science. 2008;**321**:385-388. DOI: 10.1126/science.1157996

[37] Novoselov KS, Morozov V, Jiang D, Zhang Y, Dubonos SV, Grigorieva IV, Firsov AA, Geim AK. Electric field effect in atomically thin carbon films. Science. 2004;**306**:666-670

[38] Kim J, Cote LJ, Huang J. Two dimensional soft material: New faces of graphene oxide. Accounts of Chemical Research. 2012;**45**:1356-1364. DOI: 10.1021/ar300047s

[39] Shang Y, Zhang D, Yang C, Liu Y, Liu Y. Effect of graphene oxide on the rheological properties of cement pastes. Construction and Building Materials. 2015;**96**:20-28. DOI: 10.1016/J.CONBUILDMAT.2015.07.181

[40] Li X, Korayem AH, Li C, Liu Y, He H, Sanjayan JG, et al. Incorporation of graphene oxide and silica fume into cement paste: A study of dispersion and compressive strength. Construction and Building Materials. 2016;**123**:327-335. DOI: 10.1016/J.CONBUILDMAT. 2016.07.022

[41] Yang H, Monasterio M, Cui H, Han N. Experimental study of the effects of graphene oxide on microstructure and properties of cement paste composite. Composites. Part A, Applied Science and Manufacturing. 2017;**102**:263-272. DOI: 10.1016/J.COMPOSITESA. 2017.07.022

[42] Zhu XH, Kang XJ, Yang K, Yang CH. Effect of graphene oxide on the mechanical properties and the formation of layered double hydroxides (LDHs) in alkali-activated slag cement. Construction and Building Materials. 2017;**132**:290-295. DOI: 10.1016/j. conbuildmat.2016.11.059

[43] Zhao L, Guo X, Ge C, Li Q, Guo L, Shu X, et al. Mechanical behavior and toughening mechanism of polycarboxylate superplasticizer modified graphene oxide reinforced cement composites. Composites. Part B, Engineering. 2017;**113**:308-316. DOI: 10.1016/J. COMPOSITESB.2017.01.056

[44] Li W, Li X, Chen SJ, Liu YM, Duan WH, Shah SP. Effects of graphene oxide on early-age hydration and electrical resistivity of Portland cement paste. Construction and Building Materials. 2017;**136**:506-514. DOI: 10.1016/j.conbuildmat.2017.01.066

[45] Lv S, Ma Y, Qiu C, Sun T, Liu J, Zhou Q. Effect of graphene oxide nanosheets of microstructure and mechanical properties of cement composites. Construction and Building Materials. 2013;**49**:121-127. DOI: 10.1016/j.conbuildmat.2013.08.022

[46] Wang M, Wang R, Yao H, Farhan S, Zheng S, Du C. Study on the three dimensional mechanism of graphene oxide nanosheets modified cement. Construction and Building Materials. 2016;**126**:730-739. DOI: 10.1016/j.conbuildmat.2016.09.092

[47] Lu Z, Li X, Hanif A, Chen B, Parthasarathy P, Yu J, et al. Early-age interaction mechanism between the graphene oxide and cement hydrates. Construction and Building Materials. 2017;**152**:232-239. DOI: 10.1016/J.CONBUILDMAT.2017.06.176

[48] Li X, Liu YM, Li WG, Li CY, Sanjayan JG, Duan WH, et al. Effects of graphene oxide agglomerates on workability, hydration, microstructure and compressive strength of cement paste. Construction and Building Materials. 2017;**145**:402-410. DOI: 10.1016/J.CONBUILDMAT.2017.04.058

[49] Sharma S, Kothiyal NC. Comparative effects of pristine and ball-milled graphene oxide on physico-chemical characteristics of cement mortar nanocomposites. Construction and Building Materials. 2016;**115**:256-268. DOI: 10.1016/j.conbuildmat.2016.04.019

[50] Li X, Lu Z, Chuah S, Li W, Liu Y, Duan WH, et al. Effects of graphene oxide aggregates on hydration degree, sorptivity, and tensile splitting strength of cement paste. Composites: Part A, Applied Science and Manufacturing. 2017;**100**:1-8. DOI: 10.1016/J.COMPOSITESA.2017.05.002

[51] Mohammed A, Sanjayan JG, Duan WH, Nazari A. Incorporating graphene oxide in cement composites: A study of transport properties. Construction and Building Materials. 2015;**84**:341-347. DOI: 10.1016/J.CONBUILDMAT.2015.01.083

[52] Du H, Gao HJ, Pang SD. Improvement in concrete resistance against water and chloride ingress by adding graphene nanoplatelet. Cement and Concrete Research. 2016;**83**:114-123. DOI: 10.1016/J.CEMCONRES.2016.02.005

[53] Xu J, Zhang D. Pressure-sensitive properties of emulsion modified graphene nanoplatelets/cement composites. Cement and Concrete Composites. 2017;**84**:74-82. DOI: 10.1016/j.cemconcomp.2017.07.025

[54] Shi Z-Q, Chung DD. Carbon fiber-reinforced concrete for traffic monitoring and weighing in motion. Cement and Concrete Research. 1999;**29**:435-439. DOI: 10.1016/S0008-8846(98)00204-X

[55] Han B, Yu X, Ou J, Han B, Yu X, Ou J. Challenges of self-sensing concrete. In: Self-Sensing Concrete in Smart Structures. Oxford, UK: Butterworth Heinemann; 2014. pp. 361-376. DOI: 10.1016/B978-0-12-800517-0.00011-3

[56] Norris A, Saafi M, Romine P. Temperature and moisture monitoring in concrete struc-
tures using embedded nanotechnology/microelectromechanical systems (MEMS) sensors.
Construction and Building Materials. 2008;**22**:111-120. DOI: 10.1016/J.CONBUILDMAT.
2006.05.047

[57] Saafi M. Wireless and embedded carbon nanotube networks for damage detection in con-
crete structures. Nanotechnology. 2009;**20**:395502. DOI: 10.1088/0957-4484/20/39/395502

[58] Lebental B, Chainais P, Chenevier P, Chevalier N, Delevoye E, Fabbri J, et al. Aligned
carbon nanotube based ultrasonic microtransducers for durability monitoring in civil
engineering. Nanotechnology. 2011;**22**:395501. DOI: 10.1088/0957-4484/22/39/395501

[59] Kang I, Schulz MJ, Kim JH, Shanov V, Shi D. A carbon nanotube strain sensor for
structural health monitoring. Smart Materials and Structures. 2006;**15**:737-748. DOI:
10.1088/0964-1726/15/3/009

[60] Nanni F, Ruscito G, Nad L, Gusmano G. Self-sensing nanocomposite CnP—GFRP rods
as reinforcement and sensors of concrete beams. Journal of Intelligent Material Systems
and Structures. 2009;**20**:1615-1623. DOI: 10.1177/1045389X09337171

[61] Meoni A, D'Alessandro A, Downey A, García-Macías E, Rallini M, Materazzi A, et al.
An experimental study on static and dynamic strain sensitivity of embeddable smart
concrete sensors doped with carbon nanotubes for SHM of large structures. Sensors.
2018;**18**:831. DOI: 10.3390/s18030831

[62] Liu Q, Xu Q, Yu Q, Gao R, Tong T. Experimental investigation on mechanical and piezo-
resistive properties of cementitious materials containing graphene and graphene oxide
nanoplatelets. Construction and Building Materials. 2016;**127**:565-576. DOI: 10.1016/J.
CONBUILDMAT.2016.10.024

[63] Le J-L, Du H, Pang SD. Use of 2D graphene nanoplatelets (GNP) in cement composites
for structural health evaluation. Composites. Part B, Engineering. 2014;**67**:555-563. DOI:
10.1016/J.COMPOSITESB.2014.08.005

[64] Ubertini F, D'Alessandro A, Downey A, García-Macías E, Laflamme S, Castro-Triguero
R. Recent advances on SHM of reinforced concrete and masonry structures enabled by
self-sensing structural materials. Proceedings. 2017;**2**:119. DOI: 10.3390/ecsa-4-04889

[65] Li Q, Mahendra S, Lyon DY, Brunet L, Liga MV, Li D, et al. Antimicrobial nanomateri-
als for water disinfection and microbial control: Potential applications and implications.
Water Research. 2008;**42**:4591-4602. DOI: 10.1016/J.WATRES.2008.08.015

[66] Hashimoto K, Irie H, Fujishima A. TiO_2 photocatalysis: A historical overview and
future prospects. Japanese Journal of Applied Physics. 2005;**44**:8269-8285. DOI: 10.1143/
JJAP.44.8269

[67] Hochmannova L, Vytrasova J. Photocatalytic and antimicrobial effects of interior paints.
Progress in Organic Coatings. 2010;**67**:1-5. DOI: 10.1016/J.PORGCOAT.2009.09.016

[68] Huang L, Li D-Q, Lin Y-J, Wei M, Evans DG, Duan X. Controllable preparation of nano-MgO and investigation of its bactericidal properties. Journal of Inorganic Biochemistry. 2005;**99**:986-993. DOI: 10.1016/J.JINORGBIO.2004.12.022

[69] Tuan LA et al. Novel silver nanoparticles: Synthesis, properties and applications. International Journal of Nanotechnology. 2011;**8**:278-290

[70] Kang S, Herzberg M, Rodrigues DF, Elimelech M. Antibacterial effects of carbon nanotubes: Size does matter! Langmuir. 2008;**24**:6409-6413. DOI: 10.1021/la800951v

[71] Grover N, Borkar IV, Dinu CZ, Kane RS, Dordick JS. Laccase- and chloroperoxidase-nanotube paint composites with bactericidal and sporicidal activity. Enzyme and Microbial Technology. 2012;**50**:271-279. DOI: 10.1016/J.ENZMICTEC.2012.01.006

[72] Bravo J, Zhai L, Wu Z, Cohen RE, Rubner MF. Transparent superhydrophobic films based on silica nanoparticles. Langmuir. 2007;**23**:7293-7298. DOI: 10.1021/la070159q

[73] Li X, Du X, He J. Self-cleaning antireflective coatings assembled from peculiar mesoporous silica nanoparticles. Langmuir. 2010;**26**:13528-13534. DOI: 10.1021/la1016824

[74] Ling XY, Phang IY, Vancso GJ, Huskens J, Reinhoudt DN. Stable and transparent superhydrophobic nanoparticle films. Langmuir. 2009;**25**:3260-3263. DOI: 10.1021/la8040715

[75] Meng L-Y, Park S-J. Effect of fluorination of carbon nanotubes on superhydrophobic properties of fluoro-based films. Journal of Colloid and Interface Science. 2010;**342**:559-563. DOI: 10.1016/J.JCIS.2009.10.022

[76] Bu IYY, Oei SP. Hydrophobic vertically aligned carbon nanotubes on Corning glass for self cleaning applications. Applied Surface Science. 2010;**256**:6699-6704. DOI: 10.1016/J.APSUSC.2010.04.073

[77] Tan LK, Kumar MK, An WW, Gao H. Transparent, well-aligned TiO_2 nanotube arrays with controllable dimensions on glass substrates for photocatalytic applications. ACS Applied Materials & Interfaces. 2010;**2**:498-503. DOI: 10.1021/am900726k

[78] Pan C, Sun C, Wei H-M, Han G-Z, Zhang J-Z, Fujishima A, et al. Bio-inspired titanium dioxide film with extremely stable super-amphilicity. Materials Research Bulletin. 2007;**42**:1395-1401. DOI: 10.1016/J.MATERRESBULL.2006.11.008

[79] Diamanti MV, Ormellese M, Pedeferri M. Characterization of photocatalytic and superhydrophilic properties of mortars containing titanium dioxide. Cement and Concrete Research. 2008;**38**:1349-1353. DOI: 10.1016/J.CEMCONRES.2008.07.003

[80] Diamanti MV, Del Curto B, Ormellese M, Pedeferri MP. Photocatalytic and self-cleaning activity of colored mortars containing TiO_2. Construction and Building Materials. 2013;**46**:167-174. DOI: 10.1016/J.CONBUILDMAT.2013.04.038

[81] Chen X, Xu S, Yao N, Shi Y. 1.6 V nanogenerator for mechanical energy harvesting using PZT nanofibers. Nano Letters. 2010;**10**:2133-2137. DOI: 10.1021/nl100812k

[82] Wang ZL, Wu W. Nanotechnology-enabled energy harvesting for self-powered micro/nanosystems. Angewandte Chemie, International Edition. 2012;**51**:11700-11721. DOI: 10.1002/anie.201201656

[83] Martin D, Minchin RF, Belkina M, Milev A, Kannangara GSK. Toxicity and Regulatory Perspectives of Carbon Nanotubes. In: Polymer-Carbon Nanotube Composites. Cambridge, UK: Woodhead Publishing Limited; 2011. DOI: 10.1533/9780857091390.2.621

[84] Ghiazza M, Vietti G, Fenoglio I. Carbon nanotubes: Properties, applications, and toxicity. In: Health and Environmental Safety of Nanomaterials. Elsevier; 2014. pp. 147-174. DOI: 10.1533/9780857096678.3.147

[85] Zhang Q, Wu Z, Li N, Pu Y, Wang B, Zhang T, et al. Advanced review of graphene-based nanomaterials in drug delivery systems: Synthesis, modification, toxicity and application. Materials Science and Engineering: C. 2017;**77**:1363-1375. DOI: 10.1016/j.msec.2017.03.196

[86] Lalwani G, D'Agati M, Khan AM, Sitharaman B. Toxicology of graphene-based nanomaterials. Advanced Drug Delivery Reviews. 2016;**105**:109-144. DOI: 10.1016/j.addr.2016.04.028

[87] Ema M, Gamo M, Honda K. A review of toxicity studies on graphene-based nanomaterials in laboratory animals. Regulatory Toxicology and Pharmacology. 2017;**85**:7-24. DOI: 10.1016/j.yrtph.2017.01.011

Nanostructured Oxide Semiconductor Compounds with Possible Applications for Gas Sensors

Corneliu Doroftei and Liviu Leontie

Additional information is available at the end of the chapter

Abstract

Nanostructured oxide semiconductor compounds have gained a big importance, in basic and mostly in applicative researches, due to their unique properties, and their increased potential of utilization as sensors in various electronic and optoelectronic devices. The development of devices based on semiconductor materials as gas sensors has been visible during the recent years, due to their low manufacturing cost. Because the basic materials and the manufacturing processes are critical for gas sensors high performance, they need to be studied and capitalized in practice. Among the new technologies, the production of nanocrystalline materials and hybrid structures offer huge opportunities to improve sensitivity, selectivity and response time, as a consequence of the intensification of gas-sensor interaction. In this study, a series of nanostructured oxide semiconductor compounds with a spinel-type structure and perovskite, respectively, based on transition metals and synthesized by the sol-gel self-combustion method, with possible applications for resistive gas sensors, are presented.

Keywords: nanostructured materials, oxide semiconductors, sol-gel self-combustion, structural properties, gas-sensing properties

1. Introduction

In order to improve the environmental conditions, in certain spaces, monitoring and control systems are needed. These must be able to quickly and safely detect the gas-polluting sources and to compare their emissions with the accepted standards. Until now, the air pollution measurements were performed with analytical instruments using optical spectroscopy or mass chromatograph spectrometry for gases.

The optical systems measure the absorption spectrum after the target gas was excited by light. Such a sensor needs a complex system: a monochromatic excitation source and an optical sensor to analyze the absorption spectrum [1].

The spectroscopic systems are based on the direct analysis of the molecular mass or of the vibration spectrum of the target gas. Such a sensor can measure quantitatively, with a very good precision, the composition of various gases. The mass spectrometer and the gas chromatograph are the most important systems of spectroscopic gas sensors; yet, at the same time, they are very expensive, hard to implement in reduced spaces, and can rarely be used in real time [1].

Instead, a compact, robust, highly performing and low-cost gas sensor can be a very attractive alternative to the classical devices used for environment monitoring. A series of recent researches [2–7] have been focused for the development of solid gas sensors having as sensitive element oxide semiconductor materials, among which are the spinels and perovskites, and their performances began to be improved.

The main characteristics of the sensors are field of application, sensitivity, selectivity, resolution (the smallest measurable increment of the stimulus), promptitude (rate of reaction to stimuli variation), accuracy (measuring error in percentages reported to the entire scale), sensor size and mass, operating temperature and environmental conditions, life time (in hours or in operating cycles), long-term stability, and cost.

Sensitivity is the device characteristic perceived as the variation of physical and chemical properties of the material exposed to gas.

Selectivity represents the characteristic through which a sensor element can detect a certain target gas from a gas mix.

Stability represents the characteristic through a sensor that is able to give the same results, under the same experimental conditions, after the longest operating time possible.

Nowadays, there is a clear tendency to search for new types of spinel or perovskite nanostrutures and to use new synthesis techniques for the preparation of novel sensor materials in massive form (bulk), thick layers or thin layers. The use of a large number of dopants is meant to increase the sensitivity and selectivity of spinel or perovskite gas sensors. Efforts are made to extend the range of operating temperatures and to lower the optimal operating temperature, and to reduce the power consumption of the sensing element. The resistive sensors made of thin layers present the advantage that has small power consumption; yet, they are sensitive to physical and chemical contamination and are rarely regenerable [1].

The systematic studies on a large number of oxide compounds have proved that the variation of the electric conductivity in the presence of some gases in the air constitutes a common phenomenon for the oxide compounds, including spinels and perovskites [8]. The sign of the response, that is, the increase or decrease of the electric resistivity, is determined by the semiconductor type, p or n, as well as by the oxidizing or reducing character of the gas. The sensitivity of an oxide semiconductor sensor can be generally improved by doping, thus modifying the charge carrier concentration and mobility, or by microstructural modifications, for example, by reducing the particle dimensions to the nanosized range.

The modification of the electric conductivity of the sensing material exposed to the specific gas is mainly the result of the reactions that occur at the sensor surface through the modification of the adsorbed oxygen concentration [9–11]. The oxygen-adsorbed ions at the material surface extract the electrons from the material and create a potential barrier, which restricts the electron movement and conductivity. When the reacting gases combine with this oxygen, the height of the potential barrier is diminished and the gas conductivity increases accordingly. This conductivity change is directly related with the amount of the specific gas present in the environment, whence the possibility to determine the gas presence and concentration [12–14]. These gas sensor reactions appear at diverse temperatures, generally between 100 and 600°C, and the sensor needs to be positioned at the temperature of the maximum response.

One of the main challenges for the developers of spinel-type or perovskite gas sensors is to increase their selectivity. Currently, there are two general approaches for enhancing the selective properties of sensors. The first aims at preparing a material, which is specifically sensitive to a certain gas and has a reduced or zero cross-sensitivity to other compounds that may be present in the working atmosphere. With this purpose, the optimal temperature, the nature of doping elements, and their concentrations are investigated. Nonetheless, it is usually very difficult to achieve an absolutely selective oxide gas sensor in practice. Practically, most of the materials possess cross-sensitivity at least to humidity and other vapors or gases. Another approach is based on the preparation of materials able to discriminate between several gases in a mixture. It is impossible to do this by using a single signal from the sensor. This discrimination can be usually reached either by modulating the sensor temperature [15–20] or by using a sensor array [21–23]. In the former case, such discrimination is possible because of the different optimum operating temperatures for different gases. In the latter case, N signals are obtained simultaneously from N sensors, which usually differ from each other through the doping element, doping ratio, grain size, and/or temperature.

The sensor selectivity is influenced by several factors, such as the surface energy band diagram, energy of gas molecule, and the amount of gas adsorbed on the sensing material at different operating temperatures [24]. Therefore, further investigations will be necessary in order to clarify the mechanism of selectivity.

2. Reports from the specialized literature on a series of oxide semiconductor compounds used for resistive gas sensors

The specialized literature of the recent years reports a series of spinels and perovskites used to obtain gas sensors [25–39].

The spinel-type oxide semiconductors with a general formula of AB_2O_4 have demonstrated to be good materials for the detection of both oxidizing and reducing gases [25–33]. Kapse [35] conducted a study on the sensitivity of spinelic oxide compounds ($NiFe_2O_4$, $ZnFe_2O_4$, $MgFe_2O_4$, $ZnAl_2O_4$, $CoAl_2O_4$ and $MgAl_2O_4$) synthesized by citrated sol–gel technique for various gases (H_2S, NH_3, C_2H_5OH, LPG). The author obtains the best values of the magnesium spinel sensitivity ($MgFe_2O_4$) for H_2S (4.8), C_2H_5OH (12.4), LPG (6.3) at an operating temperature of 325°C

and within the $CoAl_2O_4$ spinel for NH_3 (1.3) at an operating temperature of 150°C and a concentration of 50 ppm. Sutkaa et al. [36] investigated the nickel ferrite with zinc substitutes ($Ni_{1-x}Zn_xFe_2O_4$), p-type semiconductors with increased porosity, predominantly open pores. The samples were synthesized by the sol–gel self-combustion method. For the $NiFe_2O_4$ sample, for a concentration of 500 ppm acetone vapors in the air, they obtain a sensitivity S of 3.7 at an optimal operating temperature of 275°C.

Regarding a series of perovskites of type ABO_3, Wang et al. [37] reported the utilization of the nanocrystalline $BaMnO_3$ perovskite having an *n*-type semiconductor behavior as a sensor selective to O_2, with low operating temperatures. Hara et al. [38] have reported a study on perovskites from the $SrTiO_3$ family as O_2 selective sensors, working at the room temperature. The undoped material exhibits high sensitivity, but its resistivity is extremely high, which makes it unusable in practice. It has been found that by Nb^{5+} doping, the sensor resistivity decreases, but its sensitivity also decreases. The same happens for Fe^{3+} doping. By doping with Cr^{3+}, a high decrease of resistivity was obtained, while the sensitivity remains the same. Gaudhari et al. [39] carried out a study on the Ba-doped nanostructured perovskite $SmCoO_3$ as selective sensor for CO_2, working at a temperature of 425°C. For an Sm substitution with Ba ($Sm_{0.9}Ba_{0.1}CoO_3$), a decrease in the optimum operating temperature from 425 to 370°C and a diminution of the response time are obtained.

3. Obtaining nanomaterials by the sol-gel self-combustion method

The classical method for oxide semiconductor preparation implies oxides milling, homogenization, and sintering. Since the size of the milled particles is quite big, and their homogenization is not perfect, a longer sintering operation is necessary to obtain a material with a unitary composition. During sintering, the crystallites increase up to dimensions of the order of micrometer. In order to avoid the crystallite increase phenomenon, the reaction duration must be reduced, and the compounds entering the reaction need to be homogenized at a molecular scale.

The method presented here, named sol-gel self-combustion [40–45], accomplishes the homogenization at the molecular level by introducing compounds in the form of nitrates solutions in a colloidal medium (**Figure 1**). With a view to limit the dimensions of hydroxide particles to a nanometer level and to avoid the flocculation phenomenon, the co-precipitation reaction does not occur in a simple aqueous solution, but in a colloidal solution. The colloid molecules surround the hydroxide microcrystals just after their formation and hinder their rapid growth, thus avoiding their agglomeration. The hydroxide particles remain in the place of their generation, thus providing the homogenization of hydroxide mixture. In order to be certain of the final material composition, one uses reagents, such that after the reaction of hydroxides co-precipitation, the operations of settlement, washing or filtering are no longer necessary, because the secondary reaction products are volatile or eliminable as gases or vapors through subsequent reactions.

Through an exothermic reaction in the form of a quick combustion, one obtains the semiconductor material in the form of an ultra-fine homogeneous powder. In order to obtain very small-size (nanometric) particles of oxide semiconductor material, the reactions of hydroxides calcinations and the formation of oxide compounds occur at a very short time interval (of the

order of microseconds) under the form of an autonomous combustion. The substances necessary for combustion result from the reaction of hydroxides formation itself, if adequate reagents are used in the precipitation reaction.

Because the reaction lasts a few seconds, the crystals do not have enough time to grow. The final dimension of the particle of oxide semiconductor material, as well as its structure and properties, is obtained after a heat treatment, during which the process of material crystallization and crystallites growth up to the necessary size occurs. The treatment temperature and duration are, in all the cases, smaller than those necessary for sintering according to classical methods, due to the high homogeneity of the mix.

This method provides a good product homogenization. At the same time, due to the absence of settling, filtering, or washing operations, one has the certitude of material composition.

The sol-gel self-combustion method permits to obtain an ultra-fine, homogeneous powder, with particles of nanometric size, within a narrow dimension range, and a pronounced porosity (as
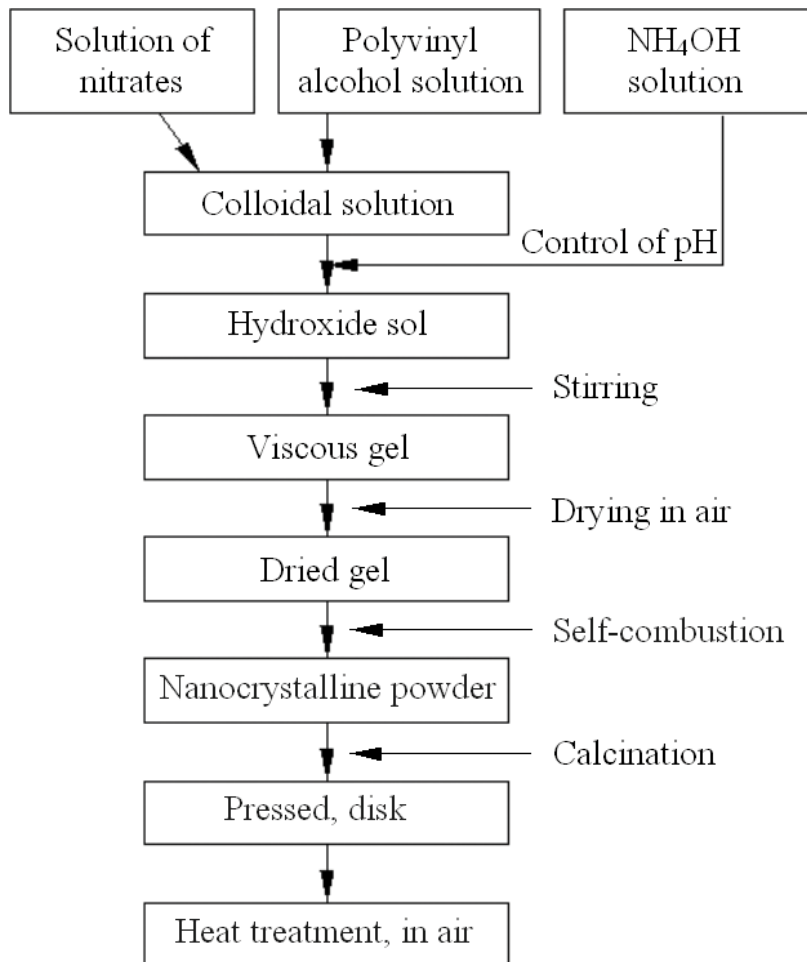

Figure 1. Stages of obtaining materials by sol-gel self-combustion method.

the open pores prevail), which favors gas access inside the samples. This open-pores system appeared during the self-combustion reaction, through which a large amount of gases was eliminated. This porous structure appears at all the oxidic compounds prepared through this method [45–49].
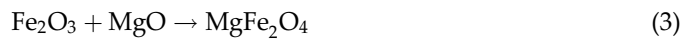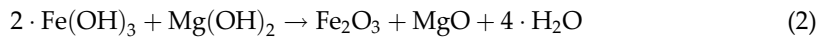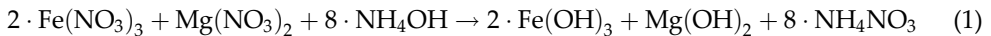
4. Nanostructured spinels and perovskites used for resistive gas sensors

In this subsection, a series of the spinels ($Mg_{1-x}Sn_xFe_2O_4$ where x = 0, 0.1) and perovskites ($La_{0.8}Pb_{0.2}Fe_{1-x}Zn_xO_3$ where x = 0, 0.05, 0.1, 0.2) obtained by the sol-gel self-combustion method used to achieve resistive gas sensors are presented and characterized.
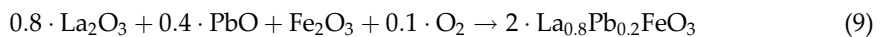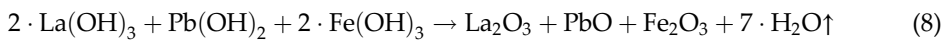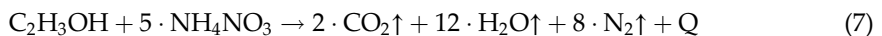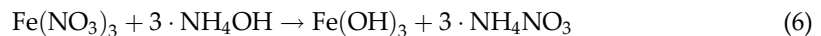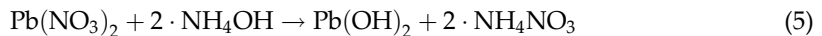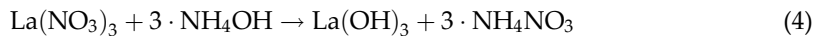
4.1. Gas sensors: obtaining and characterization

Nanograined spinelic and perovskite powders of nominal compositions: $MgFe_2O_4$ (MFO-0), $Mg_{0.9}Sn_{0.1}Fe_2O_4$ (MFO-1) and $La_{0.8}Pb_{0.2}FeO_3$ (LPFO-0), $La_{0.8}Pb_{0.2}Fe_{0.95}Zn_{0.05}O_3$ (LPFO-1), $La_{0.8}Pb_{0.2}Fe_{0.9}Zn_{0.1}O_3$ (LPFO-2), $La_{0.8}Pb_{0.2}Fe_{0.8}Zn_{0.2}O_3$ (LPFO-3), respectively, were prepared by the sol-gel self-combustion method using polyvinyl alcohol (PVA) as fuel and as colloidal medium [50, 51]. The method included the following procedures: dissolution of metal nitrates (stoichiometric amounts of analytical grade) 10% metal in deionized water, the addition of polyvinyl alcohol solution (10% in deionized water, metal/PVA ratio is 1/1), the addition of ammonia to increase pH to about 8, stirring at 80°C, drying the gel at 100–120°C, and finally self-combustion. The combusted powders were calcined at 500°C for 30 min to eliminate any residual carbon and organic compounds [50, 51].

The reactions for the basic compositions (x = 0) can be schematized as follows [30, 51]:

$$2 \cdot Fe(NO_3)_3 + Mg(NO_3)_2 + 8 \cdot NH_4OH \rightarrow 2 \cdot Fe(OH)_3 + Mg(OH)_2 + 8 \cdot NH_4NO_3 \quad (1)$$

$$2 \cdot Fe(OH)_3 + Mg(OH)_2 \rightarrow Fe_2O_3 + MgO + 4 \cdot H_2O \quad (2)$$

$$Fe_2O_3 + MgO \rightarrow MgFe_2O_4 \quad (3)$$

and

$$La(NO_3)_3 + 3 \cdot NH_4OH \rightarrow La(OH)_3 + 3 \cdot NH_4NO_3 \quad (4)$$

$$Pb(NO_3)_2 + 2 \cdot NH_4OH \rightarrow Pb(OH)_2 + 2 \cdot NH_4NO_3 \quad (5)$$

$$Fe(NO_3)_3 + 3 \cdot NH_4OH \rightarrow Fe(OH)_3 + 3 \cdot NH_4NO_3 \quad (6)$$

$$C_2H_3OH + 5 \cdot NH_4NO_3 \rightarrow 2 \cdot CO_2\uparrow + 12 \cdot H_2O\uparrow + 8 \cdot N_2\uparrow + Q \quad (7)$$

$$2 \cdot La(OH)_3 + Pb(OH)_2 + 2 \cdot Fe(OH)_3 \rightarrow La_2O_3 + PbO + Fe_2O_3 + 7 \cdot H_2O\uparrow \quad (8)$$

$$0.8 \cdot La_2O_3 + 0.4 \cdot PbO + Fe_2O_3 + 0.1 \cdot O_2 \rightarrow 2 \cdot La_{0.8}Pb_{0.2}FeO_3 \quad (9)$$

The resulting powders were subjected to cold pressing in disk-shaped samples (17-mm diameter, 1.2-mm thick), followed by heat treatment in air for 1100°C/240 min (spinels) and 900°C/40 min (perovskites) [33, 47, 50, 51].

The structure and surface properties of the heat-treated samples were investigated by X-ray diffraction (XRD), scanning electron microscopy (SEM), and energy-dispersive X-ray analysis (EDX).

For electrical measurements, a heat-treated disk was silvered on both flat surfaces. The sensor element was executed by deposing two comb-type silver electrodes on one face of the heat-treated disk using the "screen-printing" method. For the gas-sensing measurements, the sensor element was mounted on a heater capable of controlling the operating temperature and placed in a glass chamber provided with a gas homogenizer and connected to a gas-volumetric dosing device. The gas-sensing properties were investigated at various operating temperatures, included in the range of 100–420°C. The test gases used were ethanol (C_2H_5OH) and acetone (C_3H_6O) at various concentrations. The sensitivity (sensing response), S, for sensor elements made with spinel-type materials, was defined as the ratio [31, 33, 36, 50]

$$S = \frac{\Delta R}{R_a} = \frac{|R_a - R_g|}{R_a} \tag{10}$$

and for sensor elements made with perovskite-type materials, it was defined as the ratio [51–53]

$$S = \frac{R_g}{R_a} \tag{11}$$

where R_a and R_g are the sensor resistance in air and in the presence of the test gas, respectively.

4.2. Results and discussion

4.2.1. Structural properties

From the X-ray diffractometry performed for the samples presented, it was found that the MFO samples present a cubic structure of spinel type, while the LPFO samples present an orthorhombic structure perovskite type, as a result, the heat treatments in air, specific for each sample (**Table 1**). The samples have a good crystallinity in the specified thermal treatment conditions. The structural characteristics of the samples obtained from X-ray diffractometry (XRD) and from analyses by a scanning electron microscope (SEM) [33, 50] are shown in **Table 1**.

Generally, the samples are characterized by a very fine structure being composed of aggregates of nanograins with irregular shapes and sizes, with a pronounced porosity and channels that are favoring the adsorption or desorption of the gas. **Figure 2(a–d)** shows the SEM micrographs for the MFO-0, MFO-1, LPFO-0, and LPFO-2 samples where it is possible to highlight the extremely fine structure of the granule samples having a mean size of about 100 nm for the MFO-1 sample and of about 200 nm for the LPFO-2 sample. The studied samples are characterized by a high porosity (45–65%) and a specific surface area in the domain of 5–24 m^2/g. The gas sensitivity depends largely on the microstructure.

Sample symbol	Lattice constants (Å)	Average particle size D_m (nm)	Bulk density d (g/cm^3)	Porosity p (%)	Specific surface area A_{sp} (m^2/g)
MFO-0	a = 0.8354	500	2.40	45.8	5.0
MFO-1	a = 0.8352	100	2.52	51.6	23.8
LPFO-0	a = 5.5675 b = 7.8648 c = 5.5563	250	3.60	48.56	6.66
LPFO-1	a = 5.5679 b = 7.8665 c = 5.5571	230	3.40	51.49	7.67
LPFO-2	a = 5.5685 b = 7.8673 c = 5.5577	200	3.06	56.41	9.80
LPFO-3	a = 5.5688 b = 7.8685 c = 5.5584	150	2.50	64.50	16

Table 1. Structure characteristics of investigated samples.

The chemical elemental composition of the studied samples was confirmed by the energy-dispersive X-ray spectra (EDX). The obtained chemical elemental composition is typical for these compounds (any foreign element is absent). **Figure 2(e)** presents the EDX spectrum for the LPFO-2 sample.

4.2.2. Gas-sensing properties

The samples show n-type (MFO) and p-type (LPFO) semiconductor characteristics within the studied temperature range. Electrical resistivity measurements in air (ρ_a) at room temperature indicated very high values, over 10^6 Ω·cm. Thermal activation energy is about 0.4 eV for the MFO-0 sample and about 0.6 eV for the other studied samples.

In regard to gas-sensing properties, the sensitivity of the electric resistance to ethanol and acetone vapors in air was investigated. **Figures 3** and **4** show the sensitivity characteristics for the MFO (spinel-type) samples according to the operating temperatures, while these samples were exposed to saturated ethanol or acetone vapors, and **Figures 5** and **6** show the sensitivity characteristics for the LPFO (perovskite-type) samples according to the operating temperatures, while exposed to a concentration of 400 ppm ethanol or acetone vapors.

The gas sensitivity is strongly related to the working temperature, material composition, mean particle size, and porosity [50]. In the studied operating temperature range, the sensitivities increase with the increase of the temperature reaching maximum values (at temperatures called optimal operating temperatures) and then the sensitivities decrease slightly [54–56].

For MFO samples (**Figures 3** and **4**), the gas sensitivity increased with the increasing operating temperature and reached a maximum value at an optimum operating temperature (T_{op}) of
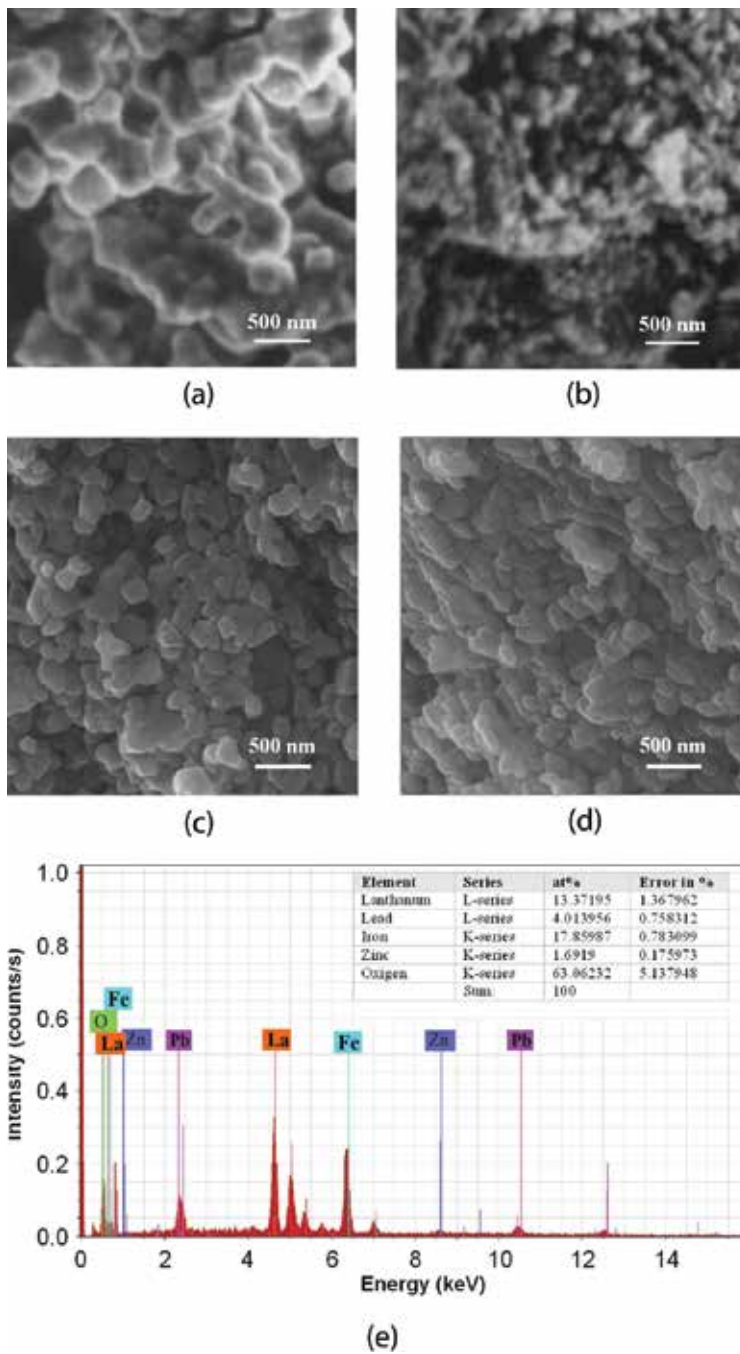
Figure 2. SEM micrographs for the MFO-0 (a), MFO-1 (b), LPFO-0 (c), and LPFO-2 (d) samples and EDX spectra (e) for the LPFO-2 sample [47, 50, 51].

about 380°C. The sensitivity to acetone vapors (**Figure 4**) is higher than that to ethanol vapors (**Figure 3**) for both samples (MFO-0 and MFO-1). The best sensitivity, 0.82, was obtained for the sample that has tin substitutions (MFO-1) to acetone vapors at an optimum operating
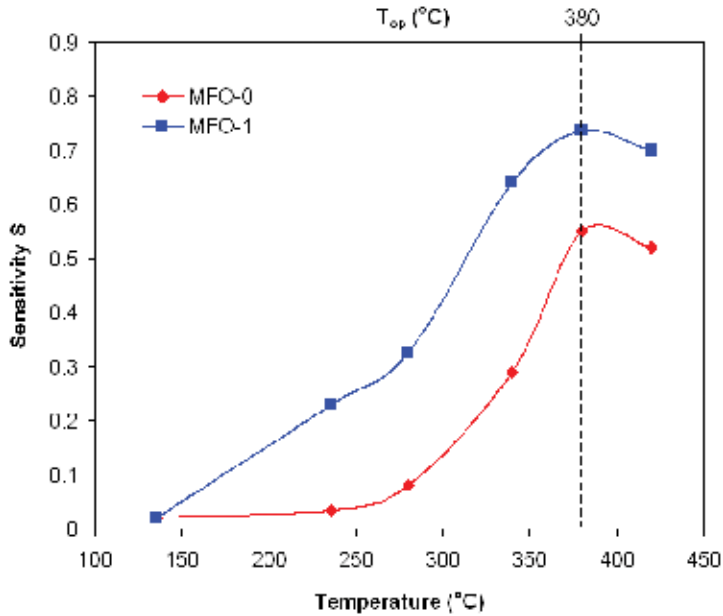

Figure 3. Sensitivity versus operating temperature characteristics for studied spinels at ethanol vapors [50].
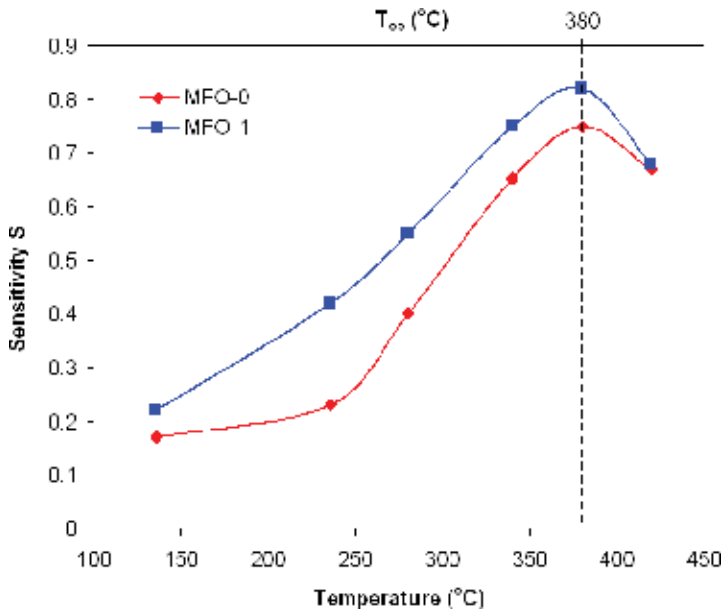

Figure 4. Sensitivity versus operating temperature characteristics for studied spinels at acetone vapors [50].

temperature of 380°C. The obtained results correlate well with the grain size changes from 500 to 100 nm (**Table 1**). The sensitivity has been improved by reducing the grain size. Martins et al. [50, 57] analyzed the effect of particle size on the sensitivity of ZnO film and reported a
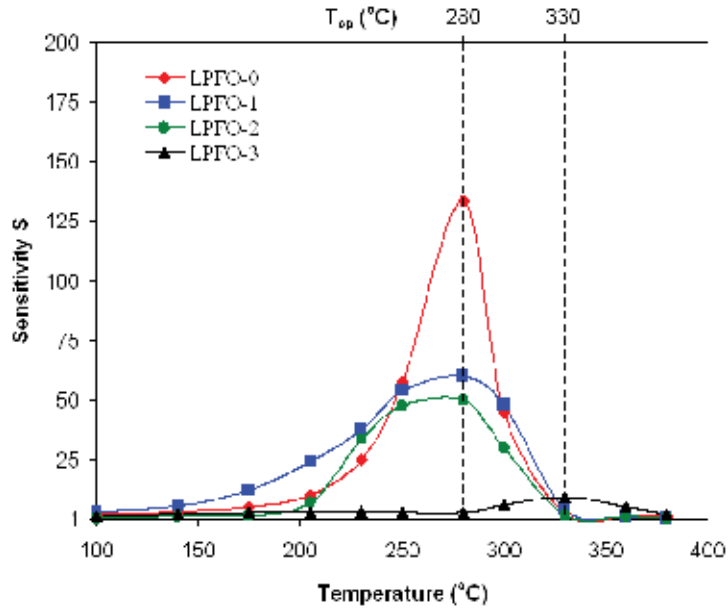

Figure 5. Sensitivity versus operating temperature characteristics for studied perovskites at ethanol vapors [51, 53].
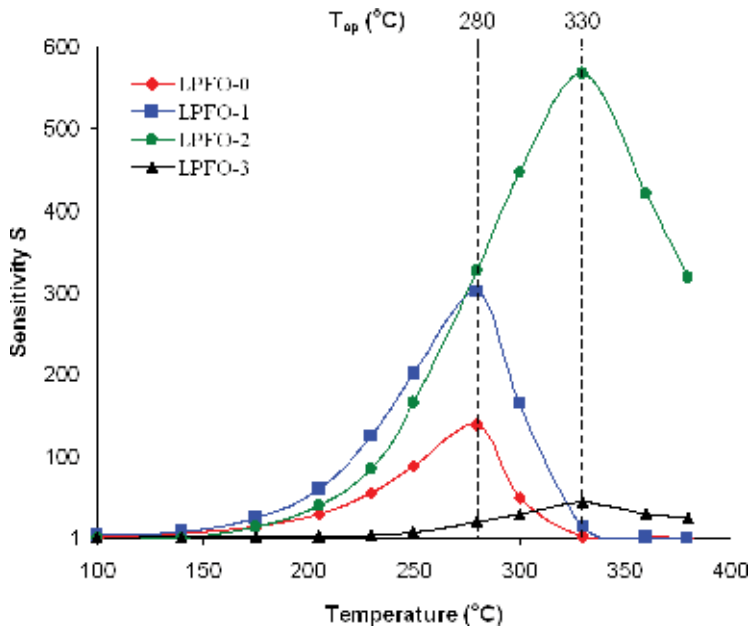

Figure 6. Sensitivity versus operating temperature characteristics for studied perovskites at acetone vapors [51, 53].
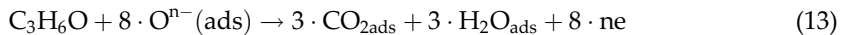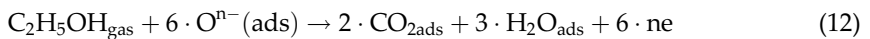
significant increase of the sensitivity as the grain size decreases from 120 to 4 nm. Also, the porous structure promotes the increase of the sensitivity. If the sensor material is porous, the gas will easily penetrate into the internal part of the sintered material, resulting in a large change in the resistance (i.e., a large sensitivity). This may be referred to as a structure effect. These results suggest that the role of tin in $MgFe_2O_4$ sample is to facilitate the oxidation of reducing gases [50].

Due to the oxidizing reaction, in the oxide semiconductors, the oxygen vacancies (point defects) appear, which change the electrical conductivity (the free electron concentration increases for the samples with n-type semiconductor behavior, analog the gaps concentration increases for the samples with p-type semiconductor behavior).

For LPFO samples, the sensitivity of ethanol (**Figure 5**) decreases with increasing Zn^{2+} ion concentration from 133 for LPFO-0 sample to 10 for LPFO-3 sample. The sensitivity of LPFO-1 and LPFO-2 samples is somewhere between and close to 50 for both samples. The optimum operating temperature remains around 280°C at the samples with x = 0, 0.05 and 0.1, and increases to 330°C for x = 0.2. The effect of Fe^{3+} ions substitution by Zn^{2+} ions consists in the diminution of the sensitivity to ethanol [51].

The sensitivity to acetone (**Figure 6**) increases very much with the increase of the Zn^{2+} ions concentration from 140 at the sample with x = 0–560 at the sample with x = 0.1. For the concentration x = 0.2, the sensitivity suddenly decreases to 45, as in the case of ethanol. The optimum operating temperature is of 280°C for the samples with x = 0 and 0.05 and increases at 330°C for x = 0.1 and 0.2. The effect of the concentration x of Zn^{2+} ions is a spectacular increase of the sensitivity up to x = 0.1, after which the sensitivity strongly decreases for higher concentrations [51].

When the C_2H_5OH (ethanol) or C_3H_6O (acetone) gas is introduced, a chemical reaction occurs between C_2H_5OH and C_3H_6O, respectively, and the adsorbed oxygen [51, 53]:

$$C_2H_5OH_{gas} + 6 \cdot O^{n-}(ads) \rightarrow 2 \cdot CO_{2ads} + 3 \cdot H_2O_{ads} + 6 \cdot ne \tag{12}$$

$$C_3H_6O + 8 \cdot O^{n-}(ads) \rightarrow 3 \cdot CO_{2ads} + 3 \cdot H_2O_{ads} + 8 \cdot ne \tag{13}$$

Electrons released from the reaction would annihilate the holes. Hence, the material resistivity increased. As each acetone molecule produces 8n electrons, that is, the highest number among the two gases, and the molar concentration was the same for the studied gases, the increase of the sensing element resistivity in the presence of acetone is the highest [51]. This suggests that $La_{0.8}Pb_{0.2}Fe_{1-x}Zn_xO_3$ sensors are applicable to detect these gases, especially acetone vapors. The substitution of Fe^{3+} ions by Zn^{2+} ions in $La_{0.8}Pb_{0.2}FeO_3$ intervenes directly, but in a different manner in the sensing mechanism of these gases. For ethanol, the sensitivity decreases with an increasing concentration of Zn^{2+} (x) ions, while for acetone, the sensitivity increases with the increase of x value, but decreases for x > 0.1. Therefore, in order to clarify the mechanism of sensitivity, especially to acetone, further investigations will be necessary [51].

5. Conclusions

Nanostructured oxide semiconductor compounds have gained a big importance, in basic and mostly in applicative researches, due to their unique properties, their increased potential of utilization as sensors in various electronic and optoelectronic devices. The development of devices based on semiconductor materials as gas sensors has been visible during the recent years, due to their low manufacturing cost.

The mass spectrometer and the gas chromatograph are the most important systems of spectroscopic gas sensors; yet, at the same time, they are very expensive, hard to implement in reduced spaces and can rarely be used in real time.

Instead, a compact, robust, highly performing, and low-cost gas sensor can be a very attractive alternative to the classical devices used for environment monitoring. A series of recent researches have focused on the development of solid gas sensors having as sensitive element oxide semiconductor materials, among which are the spinels and perovskites, and their performances began to be improved.

In this chapter, the structural, morphological, and sensory characteristics of some porous oxide semiconductor compounds with a spinel-type structure ($Mg_{1-x}Sn_xFe_2O_4$; x = 0, 0.1) or with a perovskite-type structure ($La_{0.8}Pb_{0.2}Fe_{1-x}Zn_xO_3$; x = 0, 0.05, 0.1, 0.2) were presented.

These compounds were prepared by the sol-gel self-combustion method. After the thermal treatments in air, the samples attain corresponding crystalline structure (spinel-type or perovskite-type, respectively).

The spinel-type samples are characterized by a very fine structure (100–500 nm) with an accentuated porosity (46–65%) and channels that favor the adsorption or desorption of the gas around particle agglomerates. Samples show a semiconductor behavior with a thermal activation energy between 0.4 and 0.6 eV. The gas sensitivity is strongly related to the working temperature, material composition, mean particle size, and porosity.

In the case of these samples, the gas sensitivity increased with the increasing operating temperature and reached a maximum value at an optimum operating temperature (T_{op}) of about 380°C. The sensitivity to acetone vapors is higher than that to ethanol vapors for both samples (x = 0 and x = 0.1). The best sensitivity, 0.82, was obtained for the sample that has tin substitutions (x = 0.1) to acetone vapors at an optimum operating temperature of 380°C. The obtained results correlate well with the grain size changes from 500 to 100 nm.

The perovskite-type compounds exhibit orthorhombic symmetry (space group Pnma) and crystallizes in the perovskite-like cell of $LaFeO_3$, having a porous granular and a uniform structure. The average grain size decreases from 250 to 150 nm with the increase of Zn concentration. The porosity of the samples increases with increasing Zn concentration from 31.11 to 46.78%. The sensor elements show p-type-semiconducting properties for all studied gases within the temperature range of 100–380°C. Through the substitution of the Fe^{3+} ions by Zn^{2+} ions (x = 0.1), the sensor element has the best response to acetone. At a concentration of 400 ppm gas at the operating temperature of 330°C, the response to acetone is spectacular (560).

Conflict of interest

The authors declare that there are no conflicts of interest.

Author details

Corneliu Doroftei[1]* and Liviu Leontie[1,2]

*Address all correspondence to: docorneliug@gmail.com

1 Integrated Center for Studies in Environmental Science for North-East Region, Alexandru Ioan Cuza University of Iasi, Iasi, Romania

2 Faculty of Physics, Alexandru Ioan Cuza University of Iasi, Iasi, Romania

References

[1] Doroftei C, Iacomi FD. Resistive sensor for acetone vapour. Patent RO 129798 B1. 2017

[2] Fergus JW. Perovskite oxides for semiconductor-based gas sensors. Sensors and Actuators B. 2007;**123**:1169-1179. DOI: 10.1016/j.snb.2006.10.051

[3] Naderer M, Kainz T, Schütz D, Reichmann K. The influence of Ti-nonstoichiometry in $Bi_{0.5}Na_{0.5}TiO_3$. Journal of the European Ceramic Society. 2014;**34**:663-667. DOI: 10.1016/j.jeurceramsoc.2013.10.010

[4] Bukhari SM, Giorgi J. Ni doped $Sm_{0.95}Ce_{0.05}FeO_{3-1}$ perovskite based sensors for hydrogen detection. Sensors and Actuators B. 2013;**181**:153-158. DOI: 10.1016/j.snb.2013.01.073

[5] Bertocci F, Fort A, Vignoli V, Mugnaini M, Berni R. Optimization of perovskite gas sensor performance: Characterization, measurement and experimental design. Sensors. 2017;**17**:1352-1373. DOI: 10.3390/s17061352

[6] Doroftei C, Popa PD, Iacomi F. Study of the influence of nickel ions substitutes in barium stannates used as humidity resistive sensors. Sensors and Actuators A. 2012;**173**:24-29. DOI: 10.1016/j.sna.2011.10.007

[7] Doroftei C. Formaldehyde sensitive Zn-doped LPFO thin films obtained by rf sputtering. Sensors and Actuators B. 2016;**231**:793-799. DOI: 10.1016/j.snb.2016.03.104

[8] Moseley PT, Norris JOW, Williams DE. Techniques and mechanisms in gas sensing.Bristol, UK: Adam Hilger; 1991. pp. 46-60

[9] Seiyama T, Kato A, Fujisishi K, Nagatoni M. A new detector for gaseous components using semiconductive thin films. Analytical Chemistry. 1962;**34**:1052-1053. DOI: 10.1021/ac60191a001

[10] Carotta MC, Benetti M, Ferrari E, Giberti A, Malagu C, Nagliati M, Vendemiati B, Martinelli G. Basic interpretation of thick film gas sensors for atmospheric application. Sensors and Actuators B. 2007;**126**:672-677. DOI: 10.1016/j.snb.2007.04.016

[11] Frenzer G, Frantzen A, Sanders D, Simion U, Maier WF. Wet chemical synthesis and screening of thick porous films for resistive gas sensing applications. Sensors. 2006;**6**: 1568-1586. DOI: 10.3390/s6111568

[12] Arai H, Ezaki S, Shimizu Y, Shippo O, Seiyama T. Semiconductive humidity sensor of perovskite type oxides. In: Proceedings International Meeting on Chemical Sensors; 19-22 September 1983; Fukuoka. pp. 393-398

[13] Seiyama T, Yamazoe N, Arai H. Ceramic humidity sensors. Sensors and Actuators B. 1983; **4**:85-96. DOI: 10.1016/0250-6874(83)85012-4

[14] Ding J, TJMc A, Cavicchi RE, Semancik S. Surface state trapping model for SnO_2-based microhotplate sensors. Sensors and Actuators B. 2001;**77**:597-601. DOI: 10.1016/S0925-4005(01)00765-1

[15] Chakraborty S, Sen A, Maiti HS. Selective detection of methane and butane by temperature modulation in iron doped tin oxide sensors. Sensors and Actuators B. 2006;**115**:610-613. DOI: 10.1016/j.snb.2005.10.046

[16] Parret F, Menini P, Marlinez A, Soulantica K, Maisonnat A, Chaudret B. Improvement of micromachined SnO_2 gas sensors selectivity by optimised dynamic temperature operating mode. Sensors and Actuators B. 2006;**118**:276-282. DOI: 10.1016/j.snb.2006.04.055

[17] Nakata S, Okunishi H, Nakashima Y. Distinction of gases with a semiconductor sensor under a cyclic temperature modulation with second-harmonic heating. Sensors and Actuators B. 2006;**119**:556-561. DOI: 10.1016/j.snb.2006.01.009

[18] Nakata S, Okunishi H, Nakashima Y. Distinction of gases with a semiconductor sensor depending on the scanning profile of a cyclic temperature. The Analyst. 2006;**131**:148-154. DOI: 10.1039/B509996J

[19] Huang JR, Li GY, Huang ZY, Huang XJ, Liu JH. Temperature modulation and artificial neural network evaluation for improving the CO selectivity of SnO_2 gas sensor. Sensors and Actuators B. 2006;**114**:1059-1063. DOI: 10.1016/j.snb.2005.07.070

[20] Huang JR, Gu CP, Meng FL, Li MQ, Liu JH. Detection of volatile organic compounds (VOCs) by using a single temperature modulated SnO_2 gas sensor and artificial neural network. Smart Materials and Structures. 2007;**16**:701-705

[21] Baschirotto A, Capone S, D'Amico A, Di Natale G, Ferragina V, Ferri G, Francioso L, Grassi M, Guerrini N, Malcovati P, Martinelli E, Siciliano P. A portable integrated widerange gas sensing system with smart A/D front-end. Sensors and Actuators B. 2008; **130**:164-174. DOI: 10.1016/j.snb.2007.07.144

[22] Sysoev VV, Goschnick J, Schneider T, Strelcov E, Kolmakov A. A gradient microarray electronic nose based on percolating SnO_2 nanowire sensing elements. Nano Letters. 2007;**7**:3182-3188. DOI: 10.1021/nl071815+

[23] Rock F, Barsan N, Weimar U. Electronic nose: Current status and future trends. Chemical Reviews. 2008;**108**:705-725. DOI: 10.1021/cr068121q

[24] Wen Z, Tian-mo L. Gas-sensing properties of SnO_2-TiO_2-based sensor for volatile organic compound gas and its sensing mechanism. Physica B: Condensed Matter. 2010;**405**:1345-1348. DOI: 10.1016/j.physb.2009.11.086

[25] Bangale SV, Patil DR, Bamane SR. Nanostructured spinel $ZnFe_2O_4$ for the detection of chlorine gas. Sensors and Transducers Journal. 2011;**134**:107-119

[26] Iftimie N, Rezlescu E, Popa PD, Rezlescu N. Gas sensitivity of nanocrystalline nickel ferrite. Journal of Optoelectronics and Advanced Materials. 2006;**8**:1016-1018

[27] Comini E, Ferroni M, Guidi V, Fagila G, Martinelli G, Sberveglieri G. Nanostructured mixed oxides compounds for gas sensing applications. Sensors and Actuators B. 2002;**84**:26-32. DOI: 10.1016/S0925-4005(02)00006-0

[28] Reddy CVG, Manorama SV, Rao VJ. Semiconducting gas sensor for chlorine based on inverse spinel nickel ferrite. Sensors and Actuators B. 1999;**55**:90-95. DOI: 10.1016/S0925-4005(99)00112-4

[29] Chen NS, Yang XJ, Liu ES, Huang JL. Reducing gas-sensing properties of ferrite compounds MFe_2O_4 (M = Cu, Zn, Cd and Mg). Sensors and Actuators B. 2000;**66**:178-180. DOI: 10.1016/S0925-4005(00)00368-3

[30] Rezlescu N, Doroftei C, Rezlescu E, Popa PD. Structure and humidity sensitive electrical properties of the Sn^{4+} and/or Mo^{6+} substituted Mg ferrite. Sensors and Actuators B. 2006;**115**:589-595. DOI: 10.1016/j.snb.2005.10.028

[31] Satyanarayana L, Reddy KM, Manorama SV. Synthesis of nanocrystalline $Ni_{1-x}Co_xMn_x$ $Fe_{2-x}O_4$: A material for liquefied petroleum gas sensing. Sensors and Actuators B. 2003;**89**:62-67. DOI: 10.1016/S0925-4005(02)00429-X

[32] Niu X, Du W, Du W. Preparation and gas sensing properties of ZnM_2O_4 (M = Fe, Co, Cr). Sensors and Actuators B. 2004;**99**:405-409. DOI: 10.1016/j.snb.2003.12.007

[33] Rezlescu N, Doroftei C, Rezlescu E, Popa PD. Lithium ferrite for gas sensing applications. Sensors and Actuators B. 2008;**133**:420-425. DOI: 10.1016/j.snb.2008.02.047

[34] Liu X, Cheng B, Qin H, Song P, Huang S, Zhang R, Hu J, Jiang M. Preparation, electrical and gas sensing properties of perovskite-type $La_{1-x}Mg_xFeO_3$ semiconductor materials. Journal of Physics and Chemistry of Solids. 2007;**68**:511-515. DOI: 10.1016/j.jpcs.2007.01.009

[35] Kapse VD. Preparation of nanocrystalline spinel-type oxide materials for gas sensing applications. Research Journal of Chemical Sciences. 2015;**5**:7-12

[36] Sutkaa A, Mezinskis G, Lusis A, Stingaciuc M. Gas sensing properties of Zn-doped p-type nickel ferrite. Sensors and Actuators B. 2012;**171–172**:354-360. DOI: 10.1016/j.snb.2012.04.059

[37] Wang N, Hu CG, Xia CH, Feng B, Zhang WZ, Xi Y, Xiong YF. Ultrasensitive gas sensitivity property of $BaMnO_3$ nanorods. Applied Physics Letters. 2007;**90**:163111.1-163111.3. DOI: 10.1063/1.2722692

[38] Hara T, Ishiguro T, Wakiya N, Shinozaki K. Oxigen sensing properties of $SrTiO_3$ thin films. Japanese Journal of Applied Physics. 2008;**47**:7486-7489. DOI: 10.1143/JJAP.47.7486

[39] Chaudhari GN, Padole PR, Jagatap SV, Pawar MJ. CO_2 sensing characteristics of $Sm_{1-x}Ba_xCoO_3$ (x = 0; 0.1; 0.15; 0.2) nanostructured thick film. International Journal on Smart Sensing and Intelligent Systems. 2008;**1**:613-622

[40] Rezlescu N, Rezlescu E, Popa PD, Doroftei C, Ignat M. Comparative study between catalyst properties of simple spinel ferrite powders prepared by self-combustion route. Romanian Reports in Physics. 2013;**65**:1348-1356

[41] Doroftei C, Leontie L, Popa A. The study on nanogranular system manganites La-Pb-Ca-Mn-O which exhibits a large magnetoresistance near room temperature. Journal of Materials Science-Materials in Electronics. 2017;**28**:12891-12899. DOI: 10.1007/s10854-017-7119-8

[42] Doroftei C, Popa PD, Rezlescu E, Rezlescu N. Structural and catalytic characterization of nanostructured iron manganite. Composites: Part B. 2014;**67**:179-182. DOI: 10.1016/j.compositesb.2014.07.005

[43] Rezlescu N, Rezlescu E, Popa PD, Doroftei C, Ignat M. Some nanograined ferrites and perovskites for catalytic combustion of acetone at low temperature. Ceramics International. 2015;**41**:4430-4437. DOI: 10.1016/j.ceramint.2014.11.134

[44] Rezlescu N, Rezlescu E, Popa PD, Doroftei C, Ignat M. Scandium substituted nickel-cobalt ferrites nanoparticles for catalyst applications. Applied Catalysis B. 2014;**158**:70-75. DOI: 10.1016/j.apcatb.2014.03.052

[45] Rezlescu N, Rezlescu E, Popa PD, Doroftei C, Ignat M. Nanostructured $GdAlO_3$ perovskite, a new possible catalyst for combustion of volatile organic compounds. Journal of Materials Science. 2013;**48**:4297-4304. DOI: 10.1007/s10853-013-7243-7

[46] Doroftei C, Popa PD, Rezlescu E, Rezlescu N. Nanocrystalline $SrMnO_3$ powder as catalyst for hydrocarbon combustion. Journal of Alloys and Compounds. 2014;**584**:195-198. DOI: 10.1016/j.jallcom.2013.09.054

[47] Doroftei C, Popa PD, Iacomi F. Synthesis of nanocrystalline La-Pb-Fe-O perovskite and methanol sensing. Sensors and Actuators B. 2012;**161**:977-981. DOI: 10.1016/j.snb.2011.11.078

[48] Leontie L, Doroftei C. Nanostructured spinel ferrites for catalytic combustion of gasoline vapors. Catalysis Letters. 2017;**147**:2542-2548. DOI: 10.1007/s10562-017-2164-8

[49] Doroftei C, Leontie L. Synthesis and characterization of some nanostructured composite oxides for low temperature catalytic combustion of dilute propane. RCS Advances. 2017;**7**:27863-27871. DOI: 10.1039/c7ra03916f

[50] Rezlescu N, Doroftei C, Rezlescu E, Popa PD. The influence of Sn^{4+} and/or Mo^{6+} ions on the structure, electrical and gas sensing properties of Mg-ferrite. Physica Status Solidi A. 2006;**203**:306-316. DOI: 10.1002/pssa.200521043

[51] Doroftei C, Popa PD, Iacomi F, Leontie L. The influence of Zn^{2+} ions on the microstructure, electrical and gas sensing properties of $La_{0.8}Pb_{0.2}FeO_3$ perovskite. Sensors and Actuators B. 2014;**191**:239-245. DOI: 10.1016/j.snb.2013.09.113

[52] D'Amico A, Di Natale C. A contribution on some basic definitions of sensors properties. IEEE Sensors Journal. 2001;**1**:183-190. DOI: 10.1109/JSEN.2001.954831

[53] Doroftei C, Popa PD, Iacomi F. Selectivity between methanol and ethanol gas of La-Pb-Fe-O perovskite synthesized by novel method. Sensors and Actuators A. 2013;**190**:176-180. DOI: 10.1016/j.sna.2012.11.018

[54] Zhang L, Qin HW, Song P, Hu JF, Jiang MH. Electric properties and acetone-sensing characteristics of $La_{1-x}Pb_xFeO_3$ perovskite system. Materials Chemistry and Physics. 2006;**98**:358-362. DOI: 10.1016/j.matchemphys.2005.09.041

[55] Song P, Qin HV, Zhang L, An K, Lin ZI, Hu JF, Jiang MH. The structure, electrical and ethanol-sensing properties of $La_{1-x}Pb_xFeO_3$ perovskite ceramicswith x ≤ 0.3. Sensors and Actuators B. 2005;**104**:312-316. DOI: 10.1016/j.snb.2004.05.023

[56] Singh MP, Singh H, Singh O, Kohli N, Singh RC. Preparation and characterization of nanocrystalline WO_3 powder based highly sensitive acetone sensor. Indian Journal of Physics. 2012;**86**:357-361. DOI: 10.1007/s12648-012-0062-x

[57] Martins R, Fortunato E, Nunes P, Fereira I, Marques A. Zinc oxide as an ozone sensor. Journal of Applied Physics. 2004;**96**:1398-1408. DOI: 10.1063/1.1765864

Edited by Marcelo Rubén Pagnola,
Jairo Useche Vivero and Andres Guillermo Marrugo

A fundamental part of modern technology is composed of devices that use special materials as main components. Since the last few decades of the last century and even more recently, a remarkable development has been achieved in new micro- and nanostructured materials with compositional structures and production methods that open unprecedented technological, economic, and ecological perspectives due to high yields, economies of scale, the possibility of reducing weight and size, and the low environmental impact of the equipment that contains them. This book offers a collection of excellent studies that use state-of-the-art methodologies developed by professional researchers from different countries in diverse areas of materials. In this way, this book is particularly useful to academics, scientists, practicing researchers, and postgraduate students whose work relates to the latest nanomaterial technologies.

IntechOpen